Effect of Varying Internal Geometry on the Static Performance of Rectangular Thrust-Reverser Ports

Richard J. Re and Mary L. Mason

NASA

NASA Technical Memorandum 89061

Effect of Varying Internal Geometry on the Static Performance of Rectangular Thrust-Reverser Ports

Richard J. Re and Mary L. Mason
Langley Research Center
Hampton, Virginia

NASA

Summary

An investigation has been conducted to evaluate the effects of several geometric parameters on the internal performance of rectangular thrust-reverser ports for nonaxisymmetric nozzles. Internal geometry was varied with a test apparatus which simulated a forward-flight nozzle with a single, fully deployed reverser port. The test apparatus was designed to simulate thrust reversal (conceptually) either in the convergent section of the nozzle or in the constant-area duct just upstream of the nozzle. The main geometric parameters investigated were port angle, port corner radius, port location, and internal-flow blocker angle. For all reverser-port geometries tested, the port opening had an aspect ratio (throat width to throat height) of 6.1 and had a constant passage area from the geometric port throat to the exit.

The tests were conducted in the static test facility of the Langley 16-Foot Transonic Tunnel. The reverser ports were tested at nozzle pressure ratios from 1.5 to 8.0 with high-pressure air for propulsion simulation. Port angles (measured from a horizontal reference line) investigated were 75°, 90°, 120°, and 135°. Sharp and rounded port corners were tested for each port angle. Static pressures were measured in each reverser passage. Reverser-port performance data are presented as discharge coefficients, internal thrust ratios, resultant thrust ratios, and thrust-vector angles.

Introduction

Recent interest in the utilization of the propulsion system as a significant contributor to aircraft maneuver and control capability (ref. 1) has led to many studies and research programs on multifunction nozzles (refs. 2 to 6). A notable illustration of the capabilities that the propulsion system can bring to an aircraft through management of the nozzle thrust vector is the Harrier, which is controllable in vertical and short take-off and landing modes and can utilize vectoring in forward flight for maneuverability (refs. 7 and 8).

Current research on multifunction nozzles emphasizes nonaxisymmetric nozzles because their rectangular geometry is more amenable to the incorporation of thrust-vectoring and thrust-reversing capabilities than the round geometry of axisymmetric nozzles. Many studies of nonaxisymmetric nozzles have provided a data base and some design and analysis techniques for nozzle internal performance in the conventional and thrust-vectoring modes. In general, the three nonaxisymmetric nozzle types considered (two-dimensional convergent-divergent (refs. 9 to 12), single-expansion-ramp (refs. 12 to 14), and

wedge nozzles (refs. 12, 15, and 16)) have demonstrated internal performance capabilities competitive with axisymmetric nozzles. In addition, they have shown high levels of internal performance in the thrust-vectoring mode (when the jet flow is turned subsonically). Wind tunnel investigations of aircraft configurations having nonaxisymmetric nozzles have indicated that in some cases, especially twin-engine (side-by-side) installations (refs. 17 to 19), the aerodynamic characteristics are better than the same configuration with axisymmetric nozzles.

Thrust-reverser nozzles have been investigated less systematically (refs. 10, 11, 13, and 20 to 25), but the data available have shown that internal performance is very dependent on reverser-port geometry. The performance of nozzles in the reverse-thrust mode can be significantly lower than the performance of forward-thrust nozzles. This result is not unexpected and is caused by typical reverser installation requirements. A large amount of flow turning is required to direct the internal flow into the reverser port; in addition, because of geometry restrictions, there is little length available for uniform flow convergence to the throat (minimum-flow area) in the port passages. Although a high level of flow efficiency in the reverser ports is not essential, the port area must be properly sized to prevent adverse back-pressure effects on engine operation. For example, changes in engine back pressure caused by oversized or undersized reverser ports could result in engine stall or overspeed.

An investigation has been conducted in the static test facility of the Langley 16-Foot Transonic Tunnel to evaluate the effects of varying several geometric parameters on the internal performance of rectangular thrust-reverser ports for nonaxisymmetric nozzles. Internal geometry was varied with a test apparatus which simulated a forward-flight nozzle with a single, fully deployed reverser port. A single reverser port was tested so that the angle of the port efflux could be computed directly from normal- and axial-force measurements. The test apparatus was designed to simulate thrust reversal either in the convergent section of the nozzle or in the constant-area duct located just upstream of the nozzle. The primary geometric parameters investigated were port angle, port corner radius, port location, and internal-flow blocker angle. For all reverser-port geometries tested, the port opening had an aspect ratio (throat width to throat height) of 6.1. The reverser-port throat (minimum-flow area) was always in the port passage. The port passage had a constant area from the port throat to the exit. Port angles (measured from the horizontal reference line) tested were 75° and 90°

(for thrust spoiling) and 120° and 135° (for thrust reversing). Sharp and rounded port corners were tested for each port angle. Static pressures were measured in each reverser passage. Reverser-port performance data are presented as discharge coefficients, internal thrust ratios, resultant thrust ratios, and thrust-vector angles (thrust-reverse angles).

Symbols

All forces (with the exception of resultant gross thrust) and angles are referred to the model centerline (body axis).

C_d port discharge coefficient (ratio of measured weight-flow rate to ideal weight-flow rate based on measured port area)

F measured thrust along body axis, lbf

F_i ideal isentropic gross thrust,

$$w_p \sqrt{\frac{R_j T_{t,j}}{g^2} \left(\frac{2\gamma}{\gamma-1}\right) \left[1 - \left(\frac{p_a}{p_{t,j}}\right)^{\frac{\gamma-1}{\gamma}}\right]}, \text{ lbf}$$

F_r resultant gross thrust, $\sqrt{F^2 + N^2}$, lbf

g gravitational constant, 32.174 ft/sec^2

M measured pitching moment, in-lbf

N measured normal force, lbf

NPR   nozzle pressure ratio, $p_{t,j}/p_a$

p local static pressure, psi

p_a ambient pressure, psi

$p_{t,j}$ jet total pressure, psi

R port corner radius, in.

R_j gas constant (for $\gamma = 1.3997$), 1716 ft^2/sec^2-°R

s distance along flow surface from geometric minimum to pressure orifice, in.

$T_{t,j}$ jet total temperature, °R

w_p measured weight-flow rate, lbf/sec

γ ratio of specific heats, 1.3997 for air

δ resultant thrust-vector angle, $|\tan^{-1}\frac{N}{F}|$, deg

Apparatus and Methods

Static Test Facility

This investigation was conducted in the static test facility of the Langley 16-Foot Transonic Tunnel.

The static test facility has been used extensively in the development of nonaxisymmetric nozzles and the evaluation of their internal performance (ref. 26). All tests were conducted with the jet exhausting to the atmosphere. This facility utilizes the same clean, dry air supply as that used in the 16-Foot Transonic Tunnel and a similar air-control system, including valving, filters, and a heat exchanger (to operate the jet flow at constant stagnation temperatures).

Single-Engine Propulsion-Simulation System

A sketch of the single-engine air-powered nacelle model on which various thrust-reverser ports were mounted is presented in figure 1(a) with a typical port configuration attached. An external high-pressure air system provided a continuous flow of clean, dry air at a controlled temperature of about 530°R. This high-pressure air was varied up to approximately 9 atm and was brought through a dolly-mounted support strut by six tubes which connected to a high-pressure plenum chamber. As shown in figure 1(b), the air was then discharged perpendicularly into the model low-pressure plenum through eight multiholed nozzles equally spaced around the high-pressure plenum. This method was designed to minimize the forces imposed by the transfer of axial momentum as the air was passed from the nonmetric high-pressure plenum to the metric (i.e., mounted to the force balance) low-pressure plenum. Two flexible metal bellows were used as seals and served to compensate for axial forces caused by pressurization of the low-pressure plenum. The air was then passed through the low-pressure plenum (which was circular in cross section), through a transition section, through a porous plate, and through an instrumentation section, all of which were common to all ports investigated (see fig. 1(a)). The transition section provided a smooth flow path for the airflow from the circular low-pressure plenum to the rectangular porous plate and the instrumentation section. The instrumentation section had a flow path width-height ratio of 1.437 and was identical in geometry to the model airflow entrance. All model configurations were attached to the instrumentation section at model station 41.13.

Model and Reverser-Port Description

The basic internal geometry of a typical reverser-port configuration is presented in figure 2. In general, each of the port configurations represented the top half of a thrust reverser installed in a nonaxisymmetric nozzle. By design, the nozzle internal geometry or duct geometry was rectangular in cross section. The flow path width was a constant 4.00 in. from the start of the instrumentation section to the

port exit (see inset, fig. 1(a)). The duct internal-flow area just upstream of the port corner (at model station 45.93) was sized to produce an internal-flow Mach number between 0.2 and 0.3. (See typical port internal geometry in fig. 2.) Internal-flow area was sized to represent half the flow area of a full reverser configuration by positioning a flow splitter (i.e., a flat plate) inside the model. This plate represents what would have been the horizontal plane of internal-flow symmetry (centerline) if the models had been complete thrust-reverser configurations with both top and bottom ports. Use of a single reverser port permits direct computation of the efflux angle from normal- and axial-force balance measurements. If the model simulated a complete reverser configuration, the normal-force components of opposing ports would cancel each other so that efflux angle could only be inferred or estimated.

Port geometry was varied to simulate different reverser-port designs and different reverser deployment settings. A sketch illustrating some of the model components and port variables is presented in figure 3. The four basic geometric parameters varied during this test were port angle, port location, port corner radius, and internal-flow blocker angle. Sketches of the basic reverser configurations tested with each of the port angles are presented in figures 4 to 7. Port angles of 75°, 90°, 120°, and 135° were selected to represent thrust-reversing settings, thrust-spoiling settings, or transient nozzle-reverser geometries which might occur during deployment. Port location was selected as a variable to simulate nozzle designs with the reverser located either in the constant-area section of the duct ahead of the nozzle or in the convergent section of the nozzle itself (see fig. 3(b)). To simulate a port in the convergent section of the nozzle, the surface approaching the port corner was angled 20° downward (e.g., see fig. 4(a)). To represent a port in the constant-area duct ahead of the nozzle, the same surface was held parallel to the surface of the splitter plate (e.g., see fig. 4(d)). Port corner radii were 0, 0.047, and 0.109 in. for the convergent section ports and 0 and 0.109 in. for the constant-area duct reverser ports. For each of the configurations with a rounded port corner (port corner radius > 0 in.), the internal geometry was designed such that the corner radius was tangent to the approaching-flow surface and also was tangent to the forward passage wall of the port. The internal-flow blocker angle, that is, the angle formed by the surface of the internal-flow blocker (see fig. 3(a)), was equal to the port angle for the basic reverser-port configurations tested. However, for selected configurations, different filler blocks were inserted into the model to vary the blocker angles so that different combinations of port angle and blocker angle were also tested. Sketches of the different combinations of port angle and blocker angle are shown in figures 8 to 13.

All reverser ports tested had an aspect ratio (ratio of port throat width to port throat height) of 6.1. (See fig. 3(a).) Each configuration had the same port-passage area of 2.62 in². (Port-passage area is the product of the port throat height of 0.655 in. and the port throat width of 4.00 in.) The port-passage area was constant and equal to the geometric throat area (minimum-flow area) from the port entrance to the port exit. For all basic port configurations, the passage sidewalls extended completely to the port exit to fully contain the reverser flow in the lateral plane.

In addition to the basic parametric variations of the port geometries, the effects of varying the passage wall geometry were investigated on selected reverser-port configurations with a port angle of 120°. Sketches of the configurations with modified passage walls are presented in figures 14 and 15. The effects of varying the port-passage length were investigated by assembling a 120° port configuration with three combinations of forward and aft passage walls, which resulted in ports with three different passage lengths (see fig. 14). Another 120° port was assembled with a shortened forward passage wall, which resulted in a port configuration with unequal passage wall lengths (see fig. 15).

Instrumentation

A three-component strain-gage balance was used to measure the forces and moments on the model. (See fig. 1.) Jet total pressure was measured at a fixed station in the instrumentation section (see fig. 1(a)) by means of a four-probe rake through the upper surface, a three-probe rake through the side, and a three-probe rake through the corner. A thermocouple, also located in the instrumentation section, was used to measure jet total temperature. Weight flow of the high-pressure air supplied to the port was determined by calibration of pressure and temperature measurements in the high-pressure plenum against the known performance of standard axisymmetric choke nozzles. Internal static-pressure orifices were installed in the ports along the centerlines of the forward and aft passage walls and along the surface of the port corners. A sketch of a reverser port showing the coordinate system which was used to define the pressure orifice locations is shown in figure 16. The pressure orifice locations for each port are given in the pressure data tables 1 to 33. The coordinate selected for presentation of the pressure data was s, defined as the distance along the forward

or aft flow surface of the port passage. The origin ($s = 0$) on each surface (forward or aft) was located in the plane of the port minimum geometric area at the start of the passage. Values of s were positive in the direction of the port exhaust flow and negative in the direction opposite to the flow.

Data Reduction

Approximately 50 frames of data, taken at a rate of 10 frames per second, were used for each data point to obtain average values for computations. With the exception of resultant gross thrust F_r, all force data in this report are referenced to the model centerline.

The basic performance parameters used for the presentation of results are F/F_i, F_r/F_i, δ, and C_d. The internal thrust ratio F/F_i is the ratio of actual thrust (along the body axis) to ideal thrust, where ideal thrust is based on measured weight-flow rate and on total temperature and pressure conditions in the port throat, as defined in the *Symbols* section. The balance axial-force measurement, from which actual port thrust is subsequently obtained, is initially corrected for model weight tares and balance interactions. Although the bellows arrangement was designed to eliminate pressure and momentum interactions with the balance, small bellows tares on all balance components still exist. These tares result from a small pressure difference between the ends of the bellows when internal velocities are high and from small differences in the forward and aft bellows spring constants when the bellows are pressurized. As discussed in reference 11, these bellows tares were determined by running calibration nozzles with known performance over a range of expected normal forces and pitching moments. The balance data were then corrected in a manner similar to that discussed in reference 11 to obtain actual thrust, normal force, and pitching moment. The resultant gross thrust F_r, used in the resultant thrust ratio F_r/F_i, and the resultant thrust-vector angle δ are then determined from these corrected balance data. Resultant thrust ratio F_r/F_i is equal to internal thrust ratio F/F_i as long as the jet-exhaust flow remains unvectored ($\delta = 0°$). Significant differences between F_r and F_i occur when jet-exhaust flow is turned from the axial direction, and the magnitude of these differences is a function of resultant thrust-vector angle δ. Port discharge coefficient C_d is the ratio of measured weight-flow rate to ideal weight-flow rate, where ideal weight-flow rate is based on jet total pressure $p_{t,j}$, jet total temperature $T_{t,j}$, and measured port throat area. Port discharge coefficient is thus a measure of the ability of a port to pass weight flow and is reduced by boundary-layer thickness and nonuniform flow in the throat.

Presentation of Results

Internal performance data, selected comparisons of performance parameters, and selected local static-pressure distributions are presented in figures 17 to 49. The figures are organized as follows:

For configurations with port angles of 75°, 90°, or 120°, reverser-port internal performance is presented in terms of internal thrust ratio F/F_i, resultant thrust ratio F_r/F_i, discharge coefficient C_d, and resultant thrust-vector angle δ as functions of nozzle pressure ratio (NPR). The performance parameters derived from force-balance measurements (thrust ratios and thrust-vector angle) are not presented for the reverser-port configurations with a port angle of 135°. The exit flow from the 135° port impinged on the supporting test stand and recirculated around the metric portion of the model. Because of the subsequent flow impingement effects, balance measurements were not considered accurate for the 135° port configurations. However, the performance data derived from internal measurements (discharge coefficients and static-pressure ratios) were not adversely affected by flow recirculation and are presented.

The pressure data presented in the figures represent local static pressures which were measured on the flow surfaces in the vertical plane of symmetry of the ports. Static-pressure ratios $p/p_{t,j}$ are presented graphically for selected configurations and NPR's. Complete listings of the static-pressure data for each port configuration are presented in tables 1 to 33.

Results and Discussion

A primary control parameter for stable and efficient operation of turbojet and turbofan engine systems is exhaust nozzle throat area. The size of the throat (i.e., the minimum internal-flow area) must be changed when the engine power setting is significantly altered so that engine operating parameters remain within acceptable ranges. For example, a change from a dry power setting to an afterburning power setting requires an increase in throat area. (In fighter aircraft applications, throat area nearly doubles in going from dry to full afterburning power mode.) It is essential that throat area be sized properly to keep the engine operating within its design envelope of pressures, temperatures, and rotor speeds. If throat area is too small, the back pressure on the engine will be high, possibly resulting in engine stall or in excessive internal temperature. If throat area is too large, the back pressure on the engine will be low, causing a thrust loss and the possibility of engine surge.

When the exhaust-system design includes thrust reversing upstream of the forward-flight nozzle throat, the sizing of throat area becomes more complicated. In a system with thrust-reversing capability, the throat of the internal-flow region must shift from the forward-flight nozzle location to the reverser port as the flow direction changes. The reverser-port throat area must be carefully coordinated with the changing forward-thrust nozzle throat area to avoid engine back pressurization during reverser deployment. The complex internal geometry of a deployed thrust reverser often results in an effective flow area which is significantly smaller than the geometric internal-flow area. If this effective reverser flow area is significantly smaller or larger than the corresponding forward-thrust nozzle throat area, engine operating problems could occur.

The discharge coefficient C_d reflects effective internal-flow area changes. Discharge coefficient is a measure of the normalized flow rate provided by an exhaust nozzle or reverser at a given NPR. When based on a constant geometric throat area, a change in C_d (i.e., in flow rate) indicates a change in back pressure on the engine. By matching C_d levels for a reverser configuration with those for a forward-thrust nozzle, the designer can properly size the reverser throat area to avoid adverse back-pressure effects on the engine. The C_d will reflect changes in effective internal-flow area which result from variation of port angle, port corner radius, and port location on blocker geometry, and thus can be used to evaluate the effects of reverser internal geometry on engine operation. For this investigation, C_d, based on

a measured port throat area, is used as a primary reverser performance parameter. Internal thrust ratio F/F_i and thrust-vector angle δ are used to evaluate flow-turning (reversing) capability. Resultant thrust ratio F_r/F_i provides a measure of the total thrust generated by each reverser-port configuration.

Effects of Port Corner Radius

The effects of varying port corner radius on the internal performance of configurations with each of the four port angles are shown in figures 17 to 22. Values of C_d are lowest at low NPR's (NPR $\leq$ 3.0) but increase with increasing NPR to reach a nearly constant level. The large variation in C_d with NPR at low values of NPR is typical of thrust-reversing systems that choke the flow in the ports (refs. 10 and 20) and suggests that the flow pattern in the port has not yet stabilized. At a fixed NPR, increasing the port corner radius increases the value of C_d (see figs. 21 and 22), a change which indicates that the effective port flow area is directly affected by the port corner geometry. In addition, for a given port angle and port location, the ports with the largest corner radius reach a nearly constant C_d level at lower values of NPR than the ports with a smaller corner radius. Rounding the port corner apparently establishes a stabilized port flow pattern (reflected by C_d constant with NPR) at lower NPR's. The rounded port corner geometry improves the area convergence for the flow approaching the port passage so that the change in flow area around the port corner is less abrupt. As a result, the flow starts to accelerate farther upstream of the geometric minimum (which occurs at the start of the port passage, as shown in fig. 16), and stable flow patterns in the port are formed at lower values of NPR.

The effects of port corner radius on stabilizing the port flow pattern at low NPR's are illustrated by the static-pressure distributions of figures 23 and 24. In figure 24, compare the pressure distributions for the sharp port corner configuration ($R = 0$ in.) with the pressure distributions for the rounded port corner configuration ($R = 0.109$ in.) along the duct and port corner surfaces upstream of the geometric minimum ($s < 0$ in.). After sonic speed has been reached on the port corner surface, that is, when $p/p_{t,j} < 0.5283$ (at NPR > 1.75 in fig. 24), the downstream pressures on the forward wall of the port are lower for the rounded-corner port than the corresponding pressures for the sharp-corner port at NPR's up to about 5.0. The effect of the lower pressures for the rounded-corner port is evident in the performance data. In particular, consider the pressure data of figure 24 and the C_d data of figure 19(b). The C_d data show a

more rapid increase in the range $1.75 <$ NPR < 2.0 for the rounded-corner port than for the sharp-corner port. In this same NPR range, the pressures for the rounded-corner port drop sharply below the sonic speed level. Neither the drop in pressure nor the rapid increase in C_d is evident for the sharp-corner port in the same NPR range.

In general, the static pressures of figures 23 and 24 indicate that the sonic line (where $p/p_{t,j} = 0.5283$) in the port passage is not at the geometric minimum (port-passage entrance) but is highly inclined across the passage. This inclination of the sonic line was discussed in reference 21, which presented pressure distributions measured on the sidewalls and in the port passage of a similar reverser configuration (120° port angle and sharp corner radius) with constant-area passage geometry. The forward (upstream) end of the sonic line is at, or upstream of, the port corner while the downstream end of the sonic line is on the aft wall near the passage exit. As the corner radius is increased, the flow on the forward surface accelerates earlier and, as a result, the forward end of the sonic line moves farther upstream. Computation of pressure contours for a 120° port with a corner radius of 0.109 in. was reported in reference 22. The numerical procedure used in this reference was developed to compute the internal-flow field of two-dimensional thrust reversers. The geometry of the port used for computations was the same as that of the rounded-corner port of figure 6(e) except that the passage length of the port for computation was shorter. The computed surface static pressures compare well with the data of figure 24 and indicate the end points of an inclined sonic line in the passage.

Internal thrust ratio F/F_i is obtained from the measured axial force and the computed ideal thrust and is positive in the forward-thrust direction. For reverser performance, large negative values represent desirable F/F_i results. Thus, the lower (or more negative) the value of F/F_i, the better the reverser performance. In general, the reverse-thrust-ratio goal of a thrust-reverser design is equal to the cosine of the port-passage angle if there are no flow-turning devices located in the port exit. If the ports of the present investigation are considered to be angle settings for a thrust reverser capable of varying port angle from 75° to 120°, then the design thrust ratio range is 0.259 to −0.500. (Recall that no force data are presented for the 135° port-angle configurations.)

The trends in the variation of the internal thrust ratio F/F_i with NPR are similar to the trends in the variation of C_d with NPR previously discussed (see figs. 17 to 19). At low NPR's, where C_d increases with increasing NPR until leveling off, F/F_i

decreases (i.e., reverser performance improves) significantly with increasing NPR. This decrease indicates that port reverse-thrust efficiency increases with increasing NPR until a nearly constant value of F/F_i is attained. Both C_d and F/F_i tend to level off at the same value of NPR (typically between 3.0 and 5.0), probably because the flow pattern in the port passage stabilizes in that NPR range. The port with a sharp corner produces less reverse thrust at lower NPR's than the ports with rounded corners. As NPR increases, F/F_i for the sharp-corner ports continues to decrease after F/F_i for the rounded-corner ports has leveled off, a condition indicating that the rounded-corner ports produce less reverse thrust at higher NPR's. Thus, the rounded-corner ports have better reverse-thrust F/F_i performance at low values of NPR and the sharp-corner ports have better reverse-thrust F/F_i performance at high values of NPR.

The variation of resultant thrust ratio F_r/F_i with NPR for the reverser-port configurations is similar to the variation of F_r/F_i with NPR which has been observed for two-dimensional convergent-divergent nozzles (refs. 10 and 12). For the 75° to 120° port angles and for all port corners (figs. 17 to 19), the F_r/F_i curves peak at values between 0.96 and 0.98 then decline with increasing NPR. These peaks generally occur at values of NPR between 3.0 and 3.5; this indicates that the reverser ports had an effective expansion ratio (ratio of exit area to throat area) of about 1.09. However, the port passages had no physical geometric divergence between the geometric minimum (entrance) of the passage and the exit, so that the geometric expansion ratio equals 1.0. Therefore, the effective expansion ratio results from flow phenomena in the reverser port, not from the passage geometry. The effective expansion ratio greater than 1.0, the variation of C_d at low NPR's, and the inclined sonic line deduced from the pressure distributions reflect changing, nonuniform flow conditions in the port passage at low NPR's.

There are no consistent effects of the port corner radius on F_r/F_i at low NPR's. In most cases, once the F_r/F_i curve peaks (at NPR between 3.0 and 3.5), rounded port corners ($R > 0$ in.) result in larger values of F_r/F_i than the sharp port corner (as shown in fig. 19). Thus, in general, the ports with rounded corners are more efficient in generating gross (resultant) thrust than the ports with sharp corners, especially at high NPR's.

Thrust-vector angle, by definition, combines the axial-thrust component and the normal-force thrust component (which make up resultant thrust) to describe the direction of the reverser-port flow. Data for thrust-vector angle δ show the same trends with NPR as the C_d data and the F/F_i data discussed previously. For all port corners, δ increases with increasing NPR to reach a nearly constant level. Regardless of port corner radius, all three port-angle geometries turn the flow through an angle greater than the geometric design angle at NPR's above 2.5. The value of NPR at which δ levels off and becomes nearly constant decreases with increasing port corner radius. At NPR > 3.0, the sharp port corner results in larger values of δ (i.e., better flow turning) than the rounded port corner. The better flow-turning capability of the sharp port corner at high NPR's explains the improved reverse-thrust performance of these configurations noted previously. At lower NPR's, the flow-turning capability increases with increasing port corner radius for all port corner geometries tested.

Effects of Port Angle

The effects of port angle on nozzle internal performance for each of the port corner radii are summarized in figures 25 to 28. Values of C_d, which are presented in figures 25 and 26 for three values of NPR, decrease with increasing port angle regardless of port corner radius or NPR. As port angle increases from 75° to 135°, C_d decreases by 10 to 20 percent, depending on port corner radius. This trend in C_d indicates that, independent of corner radius or NPR, the effective port flow area decreases as port angle increases, even though the geometric flow area in the passage is constant and does not change with port angle.

In figures 27 and 28, F/F_i is shown as a function of port angle for three NPR's. As expected, F/F_i decreases with increasing port angle, showing that reverse thrust increases as port angle increases. For flow conditions slightly above choked (NPR > 1.89), all the ports produce reverse thrust equal to or greater than the design thrust of the reverser-port configuration (i.e., cosine of the port angle). As mentioned earlier, the ports with rounded corners produce more reverse thrust at lower NPR's, while the ports with a sharp corner produce more reverse thrust at higher NPR's.

The effects of port angle on the internal static-pressure distributions at NPR's of 1.75, 3.0, and 5.0 are shown in figures 29 to 33. For the rounded-corner ports, the location of sonic flow conditions along the forward wall of the port passage (the values of s at which $p/p_{t,j} = 0.5283$) moves upstream with increasing port angle. This apparent effect of port angle on the internal-flow field of the ports with rounded corners is actually a consequence of two factors, namely, port-angle variation and port design geometric constraints. Unfortunately, the individual

7

effect of each factor cannot be isolated from the test data.

Port-angle variation alone can result in moving the sonic flow location upstream. As port angle increases, the flow must turn through a larger angle (for a rounded port corner). Thus, the flow probably starts to accelerate sooner and the onset of supersonic flow conditions moves upstream. The changes in the location of sonic flow conditions can also be explained by the model design geometry shown in figures 4 to 7. For all configurations with ports in the convergent section, the start of the constant passage geometry (minimum-flow area, $s = 0$ in.) is fixed at that point on the forward passage wall 1.24 in. above the splitter plate. Because this starting point is fixed, increasing the port corner radius forces a change in the internal geometric convergence of the flow path. For the configurations with ports in the convergent section and rounded-corner radii, an increase in port angle increases the length of the curved section of the port corner upstream of $s = 0$ in. to actually increase the length of the convergent section. (Compare the convergent sections of figs. 4(c), 5(c), 6(c), and 7(c) to see how the geometry changes with port angle.) For the configurations with the port in the constant-area duct, rounding the port corner actually introduces a small convergent section upstream of $s = 0$ in. (shown in figs. 4(e), 5(e), 6(e), and 7(e)). Increasing the length of the upstream convergent section or adding an upstream convergent section to the internal-flow path probably causes flow acceleration upstream of the geometric minimum so that the onset of supersonic flow conditions moves upstream.

For the sharp-corner ports (figs. 29 and 32), port angle has little effect on the location of sonic flow along the forward passage wall. Both the convergent-section sharp-corner ports and the constant-area duct sharp-corner ports have pressure distributions along the forward passage wall which are uniform at port angles up to 135°. At the 135° port angle, the sharp-corner port in the convergent section has an abrupt drop in pressure along the forward wall downstream of the port corner (in the port passage). This decrease in static pressure occurs about one-third of the way up the passage at $s \approx 0.15$ in. The pressures then increase to the ambient values near the passage exit. This pressure distribution could be the result of flow separation along the forward wall in the vicinity of the 135° port corner, with flow reattachment near the port-passage exit.

Effects of Port Location

The effects of port location on internal performance for each of the four port angles can be seen by comparing parts (a) and (b) of figures 17 to 20

and by comparing figures 25 with 26 and 27 with 28. In general, port location has only a small effect on thrust-related parameters F/F_i, F_r/F_i, and δ but has a large effect on C_d. Comparison of the C_d values of figure 25 with those of figure 26 indicates that the ports in the convergent section have C_d values between 1 and 5 percent lower than C_d values of ports in the constant-area duct. Since the port-passage geometries are the same regardless of port location, the differences in C_d must result from differences in the flow convergence to the passage. Differences in the upstream flow fields for the two port locations are related to the 20° flow angle on the internal surface approaching the port corner of the configurations with the port in the convergent section. For these configurations, the internal flow on the forward flow surface has been turned 20° away from the port (by the convergent section) before it enters the port passage. Subsequently, the turning efficiency of the port is reduced (i.e., flow must be turned through a larger angle) and lower values of C_d result.

If the primary factor causing differences in C_d with port location is assumed to be the increased internal-flow turning for ports in the convergent section, then a correlation based on flow-turning angle, rather than on port angle, should be possible. The configurations with ports in the constant-area duct have an effective flow-turning angle equal to the port angle, since all flow streamlines approaching the port corner are parallel to the horizontal reference plane (i.e., the splitter plate). The configurations with ports in the convergent section have flow streamlines approaching the port corner at angles near 20° downward along the upper wall and near 0° on the lower flow boundary (the splitter plate). For a first-order correlation, an average internal-flow angle of 10° downward relative to the horizontal reference plane can be assumed for ports in the convergent section of the nozzle. Thus, the effective flow-turning angle for convergent-section ports is the sum of the port angle and 10°. A correlation of C_d data for different flow-turning angle calculations is presented in figure 34 for ports with sharp ($R = 0$ in.) and rounded ($R = 0.109$ in.) corners at three NPR's. Results show good agreement in C_d for both port-location geometries even at NPR = 1.75, for which the port flow patterns are probably still unsettled.

Effects of Blocker Angle

For the data presented in figures 17 to 34, the internal-flow blocker angle was the same as the port angle, and the blocker formed a continuous flat surface with the port-passage aft wall. To determine the effects of blocker geometry on port performance, selected configurations were tested with the blocker

8

angle unequal to the port angle. Blocker geometry (figs. 8 to 13) was varied by inserting flat-surfaced, wedge-shaped pieces in the duct against the baseline 135° aft surface. Except for the configurations with 90° port and 120° blocker angles, blocker-angle changes altered only the internal geometry upstream of the geometric throat (entrance) of the reverser port, so that the convergence to the passage was changed by inserting the blocker but the port-passage geometry remained the same. For the configurations with 90° port and 120° blocker angles, however, increasing the blocker angle from 90° to 120° changed the location of the geometric throat.

The effect of blocker geometry on port internal performance is presented in figures 35 to 39 for three different port angles (90°, 120°, and 135°). In general, blocker-angle variations result in a 2- to 3-percent change in C_d. For the 90° port angle, a blocker angle smaller than the port angle decreases C_d and a blocker angle greater than the port angle increases C_d. For the 135° port, a blocker angle smaller than the port angle results in increased values of C_d. The effect of blocker angle on the thrust data depends on the changes blocker variation causes in the reverser internal geometry. When blocker variation changes only the convergence to the passage, a blocker angle smaller than the port angle produces increases in reverse thrust (F/F_i decreases) and in reverse-thrust-vector angle δ. Opposite effects can be noted for blocker angles greater than the port angle. When blocker variation changes the location of the port-passage entrance (90° port and 120° blocker angles), the effects on thrust parameters are somewhat different. For the 90° port with a sharp corner, increasing the blocker angle from 90° to 120° results in a crossover in F/F_i and δ at an NPR of about 4.3. The same change in blocker angle for the 90° port with a rounded corner ($R = 0.047$ in.) does not result in a crossover in F/F_i and δ; in this case, increasing the blocker angle from 90° to 120° decreases reverse-thrust and δ levels.

The effects of blocker angle on internal static-pressure distributions at three NPR's are shown in figures 40 to 45. Again, the effect of blocker angle depends on how the blocker changes the reverser internal geometry. Pressure distributions for the two configurations with 90° port and 120° blocker angles for which blocker angle changes the port-passage entrance location are presented in figures 40 and 41. Pressure data for the configurations for which blocker angle changes only the upstream convergence geometry (port-passage geometry remains constant) are shown in figures 42 to 45.

Varying the blocker angle has little effect on pressure data for most of the configurations with constant port-passage geometry. (See figs. 43 to 45.) However, the pressure data for the 90° port configuration with a corner radius of 0.109 in. show a marked effect of blocker angle, as is apparent in figure 42. At NPR's of 3.0 and 5.0, the pressures on the aft wall indicate that a local supersonic region ($p/p_{t,j} < 0.5283$) exists in the vicinity of the port-passage entrance for the 120° and the 135°/90° blocker. This supersonic region results from the flow accelerating around the sharp obtuse corner formed by the intersection of the 90° aft passage wall with the 120° or the 135° blocker. A local supersonic flow region occurs only when the blocker angle is greater than the port angle. Blocker angles equal to or less than the angle of the aft passage wall do not form a corner which would accelerate the flow and, except for a region near the port exit, the flow remains subsonic on the aft passage wall. This same 90° port configuration also shows an effect of blocker angle on the forward passage wall. The 120° and 135°/90° blockers cause pressure recovery in the passage to start closer to the geometric throat than the ports with the 75° or 90° blockers.

A crossover effect occurs for some of the thrust data when increasing blocker angle causes the port-passage entrance location to change. The pressure data for both configurations with 90° port and 120° blocker angles (figs. 40 and 41) also show a crossover. This crossover in the forward-wall pressures occurs between NPR = 3.0 and NPR = 5.0 when blocker angle changes from 90° to 120°. In addition, pressures for the 120° blocker along the aft wall are very low, indicating supersonic flow in this region.

Effects of Port-Passage Length

Port-passage length is defined as the length of the passage from the port-passage entrance (start of the constant-area passage) to the exit plane of the port. For all the basic configurations passage length was 0.49 in. (See figs. 4 to 7.) This length was selected as reasonable based on practical constraints that would be involved in the installation of a thrust-reverser passage through the duct wall and fuselage of an aircraft afterbody. However, for some applications, this passage length may be too long. Therefore, a 120° port configuration (with $R = 0.109$ in.) in the constant-area duct was selected to be tested with two shorter passage lengths. (See fig. 14.)

The effects on port internal performance of decreasing the passage length are shown in figure 46. Decreasing the passage length decreases C_d by as much as 3 percent for NPR's from 1.75 to 4.0 but has no effect on C_d for NPR's above 4.0. The values of F_r/F_i are not significantly affected by varying

passage length, but F/F_i shows a systematic variation. Reverse thrust and thrust-vector angle decrease significantly with decreasing passage length, especially when the passage length decreases from 0.31 to 0.15 in. These decreases result from incomplete flow turning in the shorter port passages.

Internal static-pressure distributions for the three passage lengths are presented in figure 47 at three NPR's. At NPR $\leq$ 3.0, the pressures along the forward wall decrease as the passage length increases. At NPR $=$ 5.0, this trend has changed so that the forward-wall pressures are lowest when the passage length is 0.31 in. At NPR's greater than 5.0, both configurations with shorter passage lengths have lower pressures along the forward wall than the port with the baseline passage length. (See tables 17 to 19.)

Effects of Forward Passage Wall Geometry

To further investigate the effects of passage wall geometry on reverser flow, a 120° port with a sharp corner was tested with a shortened forward passage wall. (See fig. 15.) The forward wall was shortened by 0.16 in., so it was 33 percent shorter than the aft passage wall. The effects of the forward passage wall on port internal performance are presented in figure 48 and the effects on internal static-pressure distributions are presented in figure 49. The performance data show no effects of forward-wall length on any performance parameters over the full NPR range. Pressures along the aft passage wall are unaffected by the change in forward-wall length, but the forward-wall pressures show a small effect which varies with NPR.

Conclusions

A static test has been conducted to determine the effects of several geometric parameters on the internal performance of rectangular thrust-reverser ports.

The parameters varied were port corner radius, port angle, port location, and internal-flow blocker angle. Port performance was evaluated in terms of discharge coefficient, resultant thrust ratio, internal thrust ratio, thrust-vector angle, and port surface static pressure. The following conclusions were determined from these data:

1. Port discharge coefficient (normalized flow rate) increased with increasing port corner radius.

2. For a given port angle, the port with the largest corner radius reached a nearly constant level of discharge coefficient at a lower nozzle pressure ratio than ports with smaller corner radii.

3. Port internal surface static pressures indicated that the sonic line was highly inclined in the passage, with the forward end of the sonic line in the vicinity of the port corner and the other end of the sonic line on the aft wall near the passage exit.

4. Discharge coefficient decreased with increasing port angle (for a given port corner radius), indicating a decrease in effective port area.

5. All the ports investigated produced reverse-thrust levels equal to or greater than the design thrust which the geometry of the port would indicate (i.e., cosine of port angle) for nozzle pressure ratios slightly above choked.

6. Simulation of a port of a given angle installed in a constant-area duct or in the convergent section of a nozzle (flow approach to port corner deflected 20° down) indicated that discharge coefficient was related more directly to the actual flow-turning angle than to port angle.

7. The effect of the blocker angle depended not only on the size of blocker angle relative to port angle but also on whether the blocker changed the convergence geometry or the location of the port throat.

References

1. Beitler, R. S.: Engine Control Considerations for Multifunction Nozzles. AIAA-84-2454, Oct.–Nov. 1984.

2. Stevens, H. L.; Thayer, E. B.; and Fullerton, J. F.: Development of the Multi-Function 2-D/C-D Nozzle. AIAA-81-1491, July 1981.

3. Lorincz, Dale J.; Chiarelli, Charles; and Hunt, Brian L.: Effect of In-Flight Thrust Reverser Deployment on Tactical Aircraft Stability and Control. AIAA-81-1446, July 1981.

4. Wasson, H. R.; Hall, G. R.; and Palcza, J. L.: Results of a Feasibility Study To Add Canards and ADEN Nozzle to the YF-17. AIAA Paper 77-1227, Aug. 1977.

5. Stevens, H. L.: *F-15/Nonaxisymmetric Nozzle System Integration Study Support Program.* NASA CR-135252, 1978.

6. Nelson, B. D.; and Nicolai, L. M.: Application of Multi-Function Nozzles to Advanced Fighters. AIAA-81-2618, Dec. 1981.

7. Myles, Bruce: *Jump Jet—The Revolutionary V/STOL Fighter,* Second ed. Brassey's Defence Publ., c.1986.

8. Fozard, John W., compiler: *The Jet V/STOL Harrier— An Evolutionary Revolution in Tactical Air Power.* Aircraft Group, British Aerospace, c.July 1978.

9. Mason, Mary L.; Putnam, Lawrence E.; and Re, Richard J.: *The Effect of Throat Contouring on Two-Dimensional Converging-Diverging Nozzles at Static Conditions.* NASA TP-1704, 1980.

10. Re, Richard J.; and Leavitt, Laurence D.: *Static Internal Performance Including Thrust Vectoring and Reversing of Two-Dimensional Convergent-Divergent Nozzles.* NASA TP-2253, 1984.

11. Capone, Francis J.: *Static Performance of Five Twin-Engine Nonaxisymmetric Nozzles With Vectoring and Reversing Capability.* NASA TP-1224, 1978.

12. Berrier, Bobby L.; and Re, Richard J.: *Effect of Several Geometric Parameters on the Static Internal Performance of Three Nonaxisymmetric Nozzle Concepts.* NASA TP-1468, 1979.

13. Re, Richard J.; and Berrier, Bobby L.: *Static Internal Performance of Single Expansion-Ramp Nozzles With Thrust Vectoring and Reversing.* NASA TP-1962, 1982.

14. Re, Richard J.; and Leavitt, Laurence D.: *Static Internal Performance of Single-Expansion-Ramp Nozzles With Various Combinations of Internal Geometric Parameters.* NASA TM-86270, 1984.

15. Maiden, Donald L.; and Petit, John E.: Investigation of Two-Dimensional Wedge Exhaust Nozzles for Advanced Aircraft. *J. Aircr.,* vol. 13, no. 10, Oct. 1976, pp. 809–816.

16. Capone, Francis J.; and Maiden, Donald L.: *Performance of Twin Two-Dimensional Wedge Nozzles Including Thrust Vectoring and Reversing Effects at Speeds up to Mach 2.20.* NASA TN D-8449, 1977.

17. Capone, Francis J.; and Berrier, Bobby L.: *Investigation of Axisymmetric and Nonaxisymmetric Nozzles Installed on a 0.10-Scale F-18 Prototype Airplane Model.* NASA TP-1638, 1980.

18. Capone, Francis J.: *Aeropropulsive Characteristics at Mach Numbers up to 2.2 of Axisymmetric and Nonaxisymmetric Nozzles Installed on an F-18 Model.* NASA TP-2044, 1982.

19. Capone, Francis J.; and Reubush, David E.: *Effects of Varying Podded Nacelle-Nozzle Installations on Transonic Aeropropulsive Characteristics of a Supersonic Fighter Aircraft.* NASA TP-2120, 1983.

20. Carson, George T., Jr.; Capone, Francis J.; and Mason, Mary L.: *Aeropropulsive Characteristics of Nonaxisymmetric-Nozzle Thrust Reversers at Mach Numbers From 0 to 1.20.* NASA TP-2306, 1984.

21. Putnam, Lawrence E.; and Strong, Edward G.: *Internal Pressure Distributions for a Two-Dimensional Thrust-Reversing Nozzle Operating at a Free-Stream Mach Number of Zero.* NASA TM-85655, 1983.

22. Imlay, S. T.; Kao, T. J.; McMaster, D. L.; and MacCormack, R. W.: Solution of the Navier-Stokes Equations for Flow Within a 2-D Thrust Reversing Nozzle. AIAA-84-0344, Jan. 1984.

23. Hakim, A.; Arena, A. V.; and Obye, R. C.: Axisymmetric Approach and Landing Thrust Reverser Concepts: Static Performance Test Results. AIAA-83-1227, June 1983.

24. Obye, R. C.; and Hakim, A. D.: Axisymmetric Approach and Landing Thrust Reverser Concepts: Hot Flow Test Results. AIAA-84-1176, June 1984.

25. Berrier, Bobby L.; and Capone, Francis J.: *Effect of Port Corner Geometry on the Internal Performance of a Rotating-Vane-Type Thrust Reverser.* NASA TP-2624, 1986.

26. Leavitt, Laurence D.: Summary of Nonaxisymmetric Nozzle Internal Performance From the NASA Langley Static Test Facility. AIAA-85-1347, July 1985.

Table 1. Ratio of Internal Static Pressure to Jet Total Pressure for Port
With Geometric Reverser Angle of 75°, Port Corner Radius
of 0 in., Constant-Area Duct Geometry, and Blocker Angle of 75°

Forward-wall static-pressure ratio, $p/p_{t,j}$

NPR	s, in.						
	-.050	.050	.100	.150	.200	.310	.410
1.503	.863	.660	.658	.660	.659	.659	.654
1.753	.835	.563	.562	.563	.562	.561	.557
1.990	.822	.492	.491	.492	.491	.489	.487
2.254	.810	.428	.427	.427	.426	.423	.424
2.506	.803	.377	.375	.375	.374	.370	.373
3.006	.797	.289	.287	.287	.285	.281	.289
3.499	.794	.194	.193	.192	.189	.190	.226
3.998	.793	.161	.160	.160	.158	.163	.221
5.000	.793	.156	.155	.155	.153	.158	.217
6.011	.793	.155	.154	.154	.153	.156	.215
7.008	.794	.154	.154	.153	.152	.155	.214
8.011	.793	.153	.153	.152	.152	.154	.212

Aft-wall static-pressure ratio, $p/p_{t,j}$

NPR	s, in.		
	.225	.325	.425
1.503	.776	.739	.705
1.753	.718	.668	.623
1.990	.681	.624	.572
2.254	.654	.589	.534
2.506	.635	.565	.506
3.006	.610	.534	.468
3.499	.590	.511	.442
3.998	.584	.505	.437
5.000	.583	.504	.436
6.011	.583	.505	.436
7.008	.583	.506	.437
8.011	.583	.507	.437

Table 2. Ratio of Internal Static Pressure to Jet Total Pressure for Port
With Geometric Reverser Angle of 75°, Port Corner Radius of
0.109 in., Constant-Area Duct Geometry, and Blocker Angle of 75°

Forward-wall static-pressure ratio, $p/p_{t,j}$

NPR	s, in.							
	-.143	-.095	-.048	.050	.100	.226	.326	.426
1.498	.786	.600	.627	.639	.638	.633	.635	.637
1.748	.747	.441	.500	.513	.509	.499	.507	.532
2.004	.732	.368	.363	.359	.359	.377	.414	.461
2.249	.728	.360	.320	.317	.317	.331	.366	.412
2.504	.723	.354	.248	.230	.227	.268	.333	.391
3.008	.724	.356	.211	.213	.211	.256	.329	.383
3.505	.724	.358	.198	.208	.207	.255	.330	.383
4.012	.723	.361	.184	.201	.203	.258	.335	.387
4.998	.723	.368	.177	.196	.201	.261	.338	.389
5.997	.724	.374	.164	.191	.200	.264	.343	.391
6.992	.724	.380	.163	.188	.199	.264	.344	.390
8.014	.723	.382	.156	.185	.200	.264	.344	.389

Aft-wall static-pressure ratio, $p/p_{t,j}$

NPR	s, in.			
	.142	.242	.342	.442
1.498	.760	.734	.683	.689
1.748	.684	.646	.567	.589
2.004	.629	.578	.459	.477
2.249	.615	.560	.444	.448
2.504	.596	.536	.425	.417
3.008	.591	.531	.422	.415
3.505	.590	.530	.420	.414
4.012	.589	.529	.419	.414
4.998	.588	.529	.418	.414
5.997	.587	.529	.417	.414
6.992	.586	.529	.417	.414
8.014	.585	.529	.417	.414

Table 3. Ratio of Internal Static Pressure to Jet Total Pressure for Port
With Geometric Reverser Angle of 75°, Port Corner Radius of
0 in., Convergent-Section Geometry, and Blocker Angle of 75°

Forward-wall static-pressure ratio, $p/p_{t,j}$

NPR	s, in.						
	−.050	.050	.100	.150	.200	.310	.410
1.503	.891	.668	.660	.660	.660	.657	.656
1.747	.871	.575	.566	.566	.565	.563	.560
1.995	.857	.503	.493	.493	.492	.490	.486
2.241	.849	.448	.436	.436	.436	.433	.428
2.506	.844	.401	.387	.387	.386	.383	.380
2.996	.838	.314	.313	.313	.312	.308	.308
3.500	.834	.251	.250	.250	.249	.244	.246
4.002	.831	.193	.192	.192	.190	.185	.195
5.004	.830	.133	.133	.133	.132	.129	.167
5.991	.830	.129	.129	.129	.129	.126	.164
6.990	.831	.128	.128	.128	.127	.125	.161
8.001	.831	.127	.127	.127	.126	.124	.160

Aft-wall static-pressure ratio, $p/p_{t,j}$

NPR	s, in.
	.376
1.503	.719
1.747	.643
1.995	.590
2.241	.555
2.506	.530
2.996	.496
3.500	.475
4.002	.460
5.004	.451
5.991	.450
6.990	.449
8.001	.449

Table 4. Ratio of Internal Static Pressure to Jet Total Pressure for Port
With Geometric Reverser Angle of 75°, Port Corner Radius of
0.047 in., Convergent-Section Geometry, and Blocker Angle of 75°

Forward-wall static-pressure ratio, $p/p_{t,j}$

NPR	s, in.						
	-.074	-.037	0.000	.050	.200	.310	.410
1.497	.784	.658	.657	.660	.658	.658	.654
1.750	.738	.557	.557	.559	.557	.554	.554
2.017	.711	.467	.467	.469	.466	.461	.469
2.249	.699	.411	.412	.413	.409	.404	.413
2.505	.691	.356	.357	.358	.353	.349	.361
2.997	.681	.257	.261	.261	.257	.254	.280
3.474	.677	.168	.178	.178	.175	.185	.249
4.005	.678	.157	.170	.169	.165	.179	.250
5.009	.678	.151	.166	.165	.162	.175	.248
6.028	.678	.144	.165	.164	.161	.174	.246
7.068	.679	.137	.164	.163	.160	.173	.246
6.972	.679	.138	.164	.163	.161	.173	.246
7.969	.679	.132	.163	.162	.159	.173	.247
8.013	.679	.132	.163	.162	.159	.173	.247

Aft-wall static-pressure ratio, $p/p_{t,j}$

NPR	s, in.
	.360
1.497	.712
1.750	.625
2.017	.551
2.249	.515
2.505	.486
2.997	.453
3.474	.433
4.005	.433
5.009	.431
6.028	.431
7.068	.431
6.972	.431
7.969	.431
8.013	.431

Table 5. Ratio of Internal Static Pressure to Jet Total Pressure for Port
With Geometric Reverser Angle of 75°, Port Corner Radius of
0.109 in., Convergent-Section Geometry, and Blocker Angle of 75°

Forward-wall static-pressure ratio, $p/p_{t,j}$

NPR	s, in.								
	-.181	-.121	-.060	0.000	.050	.100	.200	.301	.401
1.438	.810	.627	.667	.680	.681	.678	.679	.678	.682
1.495	.793	.597	.640	.653	.653	.651	.651	.649	.654
1.756	.748	.467	.530	.543	.542	.540	.539	.537	.547
1.994	.717	.401	.361	.386	.383	.378	.379	.402	.442
2.256	.710	.395	.341	.344	.341	.337	.336	.355	.391
2.499	.704	.390	.298	.300	.299	.297	.297	.314	.354
2.996	.697	.385	.236	.205	.204	.202	.211	.265	.333
3.496	.698	.387	.235	.199	.197	.195	.207	.265	.332
4.016	.697	.389	.234	.197	.194	.192	.205	.265	.332
4.997	.697	.393	.235	.195	.192	.191	.204	.263	.330
6.010	.697	.396	.234	.194	.192	.191	.203	.261	.328
6.983	.697	.398	.234	.195	.192	.192	.201	.258	.327
8.007	.697	.400	.235	.195	.193	.192	.200	.258	.329

Aft-wall static-pressure ratio, $p/p_{t,j}$

NPR	s, in.
	.371
1.438	.733
1.495	.709
1.756	.616
1.994	.501
2.256	.479
2.499	.465
2.996	.442
3.496	.440
4.016	.439
4.997	.438
6.010	.437
6.983	.437
8.007	.437

Table 6. Ratio of Internal Static Pressure to Jet Total Pressure for Port
With Geometric Reverser Angle of 90°, Port Corner Radius
of 0 in., Constant-Area Duct Geometry, and Blocker Angle of 90°

Forward-wall static-pressure ratio, $p/p_{t,j}$

NPR	s, in.						
	-.050	.050	.100	.150	.200	.310	.410
1.502	.864	.660	.659	.660	.659	.657	.655
1.745	.838	.565	.567	.565	.565	.563	.560
2.002	.820	.490	.492	.489	.489	.488	.483
2.497	.804	.386	.388	.386	.385	.383	.380
2.260	.811	.431	.431	.430	.430	.427	.424
3.008	.797	.309	.310	.307	.306	.303	.303
3.496	.792	.247	.246	.245	.244	.241	.243
4.013	.789	.185	.186	.184	.183	.179	.193
5.014	.786	.141	.141	.141	.139	.138	.175
6.007	.786	.138	.138	.137	.137	.135	.172
6.988	.785	.136	.136	.135	.135	.133	.168
8.007	.782	.125	.125	.124	.124	.122	.152

Aft-wall static-pressure ratio, $p/p_{t,j}$

NPR	s, in.				
	.050	.150	.250	.350	.450
1.502	.848	.823	.768	.730	.685
1.745	.811	.781	.709	.659	.598
2.002	.785	.752	.667	.608	.537
2.497	.758	.723	.622	.554	.480
2.260	.770	.734	.640	.576	.503
3.008	.743	.707	.596	.524	.447
3.496	.732	.698	.580	.506	.428
4.013	.724	.690	.566	.487	.408
5.014	.719	.690	.562	.484	.406
6.007	.718	.694	.562	.484	.406
6.989	.717	.696	.561	.483	.406
8.007	.759	.709	.566	.488	.410

Table 7. Ratio of Internal Static Pressure to Jet Total Pressure for Port
With Geometric Reverser Angle of 90°, Port Corner Radius of
0.109 in., Constant-Area Duct Geometry, and Blocker Angle of 90°

Forward-wall static-pressure ratio, $p/p_{t,j}$

NPR	s, in.
	−.171	−.114	−.057	0.000	.050	.100	.200	.301	.401
1.503	.797	.433	.505	.627	.632	.628	.630	.636	.649
1.748	.766	.369	.411	.505	.529	.523	.525	.534	.553
2.001	.744	.345	.285	.343	.401	.401	.408	.428	.463
2.254	.736	.338	.259	.280	.318	.331	.342	.374	.414
2.503	.732	.333	.239	.252	.254	.265	.289	.330	.374
3.013	.729	.330	.202	.204	.203	.202	.225	.289	.358
3.502	.729	.331	.192	.198	.197	.196	.221	.289	.360
4.000	.729	.330	.187	.196	.195	.194	.220	.287	.359
5.006	.731	.329	.179	.192	.191	.191	.218	.288	.361
5.979	.736	.328	.162	.184	.184	.187	.223	.292	.362
5.998	.735	.327	.162	.184	.184	.187	.223	.292	.362
7.002	.736	.325	.148	.180	.181	.184	.222	.293	.363
7.989	.737	.323	.139	.181	.181	.183	.218	.294	.365

Aft-wall static-pressure ratio, $p/p_{t,j}$

NPR	s, in.
	−.059	.041	.141	.241	.341
1.503	.851	.830	.776	.744	.714
1.748	.814	.787	.715	.672	.631
2.001	.779	.745	.656	.599	.543
2.254	.766	.731	.633	.571	.509
2.503	.755	.722	.616	.551	.486
3.013	.747	.717	.603	.536	.466
3.502	.747	.722	.602	.535	.465
4.000	.746	.725	.601	.535	.464
5.006	.746	.731	.601	.534	.464
5.979	.745	.734	.602	.534	.464
5.998	.745	.735	.601	.534	.464
7.002	.745	.738	.601	.534	.464
7.989	.745	.740	.601	.534	.464

Table 8. Ratio of Internal Static Pressure to Jet Total Pressure for Port
With Geometric Reverser Angle of 90°, Port Corner Radius of
0.109 in., Constant-Area Duct Geometry, and Blocker Angle of 75°

Forward-wall static-pressure ratio, $p/p_{t,j}$

NPR	s, in.								
	-.171	-.114	-.057	0.000	.050	.100	.200	.301	.401
1.498	.799	.440	.522	.638	.642	.640	.638	.641	.651
1.751	.767	.383	.452	.509	.535	.536	.532	.537	.552
2.010	.741	.344	.273	.383	.438	.438	.429	.431	.453
2.270	.732	.337	.264	.292	.324	.329	.335	.361	.400
2.521	.729	.335	.251	.274	.288	.296	.307	.334	.368
2.998	.724	.332	.204	.208	.206	.206	.210	.244	.307
3.502	.723	.330	.180	.186	.184	.184	.189	.233	.309
4.004	.723	.330	.176	.183	.180	.180	.185	.230	.309
4.998	.723	.328	.170	.179	.176	.176	.183	.228	.308
6.010	.727	.327	.163	.176	.173	.173	.181	.228	.309
7.004	.728	.325	.157	.174	.172	.172	.179	.225	.308
7.987	.728	.323	.146	.170	.168	.166	.173	.219	.305

Aft-wall static-pressure ratio, $p/p_{t,j}$

NPR	s, in.					
	-.059	.041	.141	.241	.341	.441
1.498	.893	.853	.791	.759	.732	.673
1.751	.868	.815	.734	.690	.654	.574
2.010	.842	.776	.679	.625	.580	.481
2.270	.829	.758	.651	.592	.538	.435
2.521	.825	.756	.643	.580	.527	.420
2.998	.816	.743	.619	.554	.493	.392
3.502	.813	.743	.614	.549	.487	.386
4.004	.812	.746	.613	.548	.485	.386
4.998	.810	.751	.613	.548	.483	.385
6.010	.809	.757	.613	.548	.484	.386
7.004	.808	.759	.612	.548	.483	.385
7.987	.804	.756	.607	.544	.479	.383

Table 9. Ratio of Internal Static Pressure to Jet Total Pressure for Port
With Geometric Reverser Angle of 90°, Port Corner Radius of
0.109 in., Constant-Area Duct Geometry, and Blocker Angle of 120°

Forward-wall static-pressure ratio, $p/p_{t,j}$

NPR	s, in.								
	-.171	-.114	-.057	0.000	.050	.100	.200	.301	.401
1.501	.784	.443	.504	.623	.627	.623	.625	.635	.651
1.752	.754	.371	.362	.496	.517	.517	.518	.530	.551
2.002	.736	.353	.287	.351	.414	.413	.424	.448	.476
2.252	.729	.344	.250	.266	.300	.322	.344	.381	.420
2.502	.725	.340	.209	.217	.215	.218	.275	.345	.396
2.995	.727	.339	.184	.198	.197	.201	.268	.345	.395
3.503	.728	.338	.181	.194	.193	.199	.266	.343	.394
3.992	.729	.338	.175	.190	.189	.199	.265	.342	.392
4.999	.732	.337	.162	.180	.183	.198	.264	.339	.391
6.002	.735	.335	.154	.176	.180	.198	.264	.340	.391
7.000	.738	.334	.151	.174	.178	.195	.261	.339	.391
7.996	.738	.332	.144	.167	.172	.186	.251	.332	.363

Aft-wall static-pressure ratio, $p/p_{t,j}$

NPR	s, in.				
	-.059	.041	.141	.241	.341
1.501	.743	.811	.746	.736	.708
1.752	.667	.760	.673	.656	.618
2.002	.605	.721	.616	.592	.539
2.252	.565	.696	.580	.554	.491
2.502	.538	.681	.558	.529	.462
2.995	.529	.683	.551	.526	.458
3.503	.531	.688	.550	.526	.457
3.992	.518	.693	.548	.525	.456
4.999	.514	.697	.548	.525	.456
6.002	.510	.700	.547	.525	.455
7.000	.503	.701	.545	.523	.453
7.996	.483	.690	.538	.516	.446

Table 10. Ratio of Internal Static Pressure to Jet Total Pressure for Port With Geometric Reverser Angle of 90°, Port Corner Radius of 0.109 in., Constant-Area Duct Geometry, and Blocker Angle of 135°/90°

Forward-wall static-pressure ratio, $p/p_{t,j}$

NPR	s, in.								
	-.171	-.114	-.057	0.000	.050	.100	.200	.301	.401
1.500	.800	.452	.515	.627	.634	.631	.627	.632	.647
1.760	.766	.377	.362	.494	.513	.516	.515	.525	.546
2.000	.751	.358	.294	.360	.424	.424	.426	.446	.474
2.249	.741	.349	.252	.265	.307	.329	.345	.380	.418
2.518	.735	.344	.189	.197	.196	.202	.276	.347	.392
3.009	.735	.342	.170	.181	.181	.190	.272	.346	.387
3.507	.735	.340	.166	.178	.177	.188	.268	.343	.384
4.007	.735	.340	.158	.174	.174	.189	.267	.342	.383
5.006	.735	.339	.152	.169	.170	.189	.265	.340	.380
6.020	.738	.339	.148	.163	.168	.188	.262	.339	.379
5.996	.738	.339	.148	.163	.168	.188	.262	.339	.379
6.992	.740	.337	.143	.157	.166	.187	.261	.339	.379
8.004	.741	.336	.141	.155	.164	.186	.259	.337	.377

Aft-wall static-pressure ratio, $p/p_{t,j}$

NPR	s, in.								
	-.532	-.391	-.250	-.059	.041	.141	.241	.341	.441
1.500	.989	.986	.971	.695	.797	.767	.738	.716	.669
1.760	.987	.983	.963	.608	.732	.698	.658	.627	.564
2.000	.985	.980	.959	.549	.689	.649	.599	.558	.476
2.249	.985	.978	.956	.507	.658	.615	.557	.507	.414
2.518	.984	.977	.954	.473	.633	.590	.529	.474	.379
3.009	.984	.977	.954	.468	.638	.587	.526	.470	.375
3.507	.985	.978	.953	.464	.641	.586	.525	.469	.374
4.007	.985	.977	.953	.462	.645	.586	.525	.468	.373
5.006	.985	.978	.954	.458	.653	.585	.524	.466	.372
6.020	.986	.978	.954	.455	.661	.582	.523	.464	.371
5.996	.986	.978	.955	.455	.657	.584	.524	.464	.372
6.992	.986	.978	.954	.452	.659	.583	.523	.463	.371
8.004	.986	.977	.953	.449	.661	.579	.521	.461	.371

Table 11. Ratio of Internal Static Pressure to Jet Total Pressure for Port
With Geometric Reverser Angle of 90°, Port Corner Radius of
0 in., Convergent-Section Geometry, and Blocker Angle of 90°

Forward-wall static-pressure ratio, $p/p_{t,j}$

NPR	s, in.					
	-.050	.100	.150	.200	.250	.381
1.505	.924	.658	.661	.658	.658	.657
1.751	.911	.565	.568	.563	.563	.561
2.006	.905	.491	.496	.490	.489	.486
2.254	.902	.436	.440	.433	.433	.429
2.517	.900	.391	.392	.386	.386	.382
2.998	.901	.321	.316	.320	.320	.317
3.508	.902	.267	.266	.266	.265	.262
3.992	.903	.224	.220	.223	.222	.217
5.004	.906	.139	.137	.137	.136	.135
6.016	.910	.111	.110	.111	.110	.114
7.016	.914	.109	.108	.108	.107	.112
8.009	.917	.108	.106	.107	.106	.110

Aft-wall static-pressure ratio, $p/p_{t,j}$

NPR	s, in.		
	.200	.300	.400
1.505	.803	.754	.706
1.751	.754	.687	.625
2.006	.720	.643	.568
2.254	.697	.613	.526
2.517	.680	.592	.497
2.998	.659	.566	.471
3.508	.644	.550	.455
3.992	.635	.539	.442
5.004	.618	.521	.424
6.016	.614	.520	.423
7.016	.613	.521	.423
8.009	.613	.521	.423

Table 12. Ratio of Internal Static Pressure to Jet Total Pressure for Port
With Geometric Reverser Angle of 90°, Port Corner Radius of
0.047 in., Convergent-Section Geometry, and Blocker Angle of 90°

Forward-wall static-pressure ratio, $p/p_{t,j}$

NPR	s, in.						
	-.090	-.045	.050	.100	.150	.250	.381
1.513	.776	.653	.654	.654	.654	.652	.649
1.761	.733	.556	.557	.558	.556	.555	.553
1.740	.737	.563	.564	.565	.564	.562	.560
2.003	.710	.478	.480	.481	.479	.476	.476
2.254	.698	.417	.418	.419	.417	.415	.414
2.505	.693	.368	.369	.370	.368	.365	.364
3.004	.686	.280	.279	.278	.278	.273	.278
3.502	.683	.201	.201	.200	.200	.196	.212
4.005	.684	.155	.156	.156	.155	.152	.199
5.015	.689	.149	.150	.149	.149	.146	.196
5.995	.693	.148	.148	.148	.147	.145	.194
6.996	.697	.148	.148	.147	.147	.144	.192
7.995	.699	.147	.147	.147	.146	.144	.191

Aft-wall static-pressure ratio, $p/p_{t,j}$

NPR	s, in.		
	.200	.300	.400
1.513	.784	.742	.692
1.761	.727	.672	.605
1.740	.732	.677	.611
2.003	.688	.624	.540
2.254	.663	.592	.499
2.505	.646	.569	.476
3.004	.618	.536	.444
3.502	.599	.514	.423
4.005	.593	.506	.413
5.015	.590	.506	.414
5.995	.589	.506	.414
6.996	.588	.506	.414
7.995	.588	.506	.414

Table 13. Ratio of Internal Static Pressure to Jet Total Pressure for Port
With Geometric Reverser Angle of 90°, Port Corner Radius of
0.109 in., Convergent-Section Geometry, and Blocker Angle of 90°

Forward-wall static-pressure ratio, $p/p_{t,j}$

NPR	s, in.							
	-.209	-.140	-.070	0.000	.050	.150	.250	.381
1.506	.881	.624	.637	.647	.630	.643	.644	.645
1.747	.860	.525	.534	.546	.544	.541	.541	.544
2.010	.849	.456	.439	.450	.452	.443	.442	.453
2.253	.845	.421	.362	.370	.370	.363	.363	.386
2.511	.844	.404	.304	.309	.309	.304	.305	.334
3.009	.844	.386	.209	.208	.208	.203	.215	.285
3.505	.849	.386	.196	.196	.196	.191	.206	.287
3.992	.853	.386	.194	.194	.194	.189	.203	.285
5.007	.860	.386	.191	.192	.192	.188	.201	.284
6.006	.864	.386	.187	.192	.191	.187	.200	.285
6.988	.868	.387	.181	.191	.191	.187	.199	.286
7.997	.870	.389	.177	.191	.190	.186	.199	.289

Aft-wall static-pressure ratio, $p/p_{t,j}$

NPR	s, in.		
	.200	.300	.400
1.506	.764	.728	.685
1.747	.698	.650	.591
2.010	.644	.583	.501
2.253	.612	.543	.461
2.511	.594	.520	.438
3.009	.567	.483	.404
3.505	.566	.482	.398
3.992	.564	.482	.397
5.007	.563	.482	.397
6.006	.562	.483	.398
6.988	.562	.483	.398
7.997	.561	.484	.399

Table 14. Ratio of Internal Static Pressure to Jet Total Pressure for Port
With Geometric Reverser Angle of 90°, Port Corner Radius
of 0 in., Convergent-Section Geometry, and Blocker Angle of 120°

Forward-wall static-pressure ratio, $p/p_{t,j}$

| NPR | s, in. |
	-.050	.100	.150	.200	.250	.381
1.504	.922	.658	.658	.657	.656	.654
1.752	.908	.563	.562	.562	.561	.558
1.999	.902	.491	.490	.490	.489	.485
2.247	.900	.434	.432	.432	.432	.428
2.496	.898	.384	.382	.382	.381	.378
3.008	.895	.276	.269	.268	.265	.265
3.510	.897	.213	.197	.196	.194	.212
4.013	.901	.199	.189	.188	.186	.207
5.011	.908	.188	.185	.185	.184	.205
6.013	.913	.182	.184	.184	.183	.205
7.012	.917	.180	.183	.183	.183	.206
7.938	.920	.180	.182	.182	.182	.208
8.008	.920	.179	.182	.182	.182	.208

Aft-wall static-pressure ratio, $p/p_{t,j}$

| NPR | s, in. |
	.200	.300	.400
1.504	.599	.718	.696
1.752	.483	.623	.612
1.999	.401	.555	.548
2.247	.349	.527	.490
2.496	.281	.524	.463
3.008	.260	.460	.426
3.510	.253	.434	.410
4.013	.253	.430	.407
5.011	.251	.427	.406
6.013	.250	.426	.406
7.012	.248	.425	.405
7.938	.247	.425	.405
8.008	.247	.425	.405

Table 15. Ratio of Internal Static Pressure to Jet Total Pressure for Port
With Geometric Reverser Angle of 90°, Port Corner Radius of
0.047 in., Convergent-Section Geometry, and Blocker Angle of 120°

Forward-wall static-pressure ratio, $p/p_{t,j}$

NPR	s, in.						
	-.090	-.045	.050	.100	.150	.250	.381
1.500	.773	.657	.656	.655	.655	.653	.652
1.777	.723	.544	.543	.543	.541	.539	.539
1.756	.728	.553	.551	.551	.550	.547	.547
2.007	.704	.447	.446	.445	.442	.438	.450
2.253	.691	.354	.352	.350	.350	.345	.375
2.498	.686	.279	.278	.276	.276	.274	.341
3.502	.688	.254	.253	.252	.251	.250	.331
4.064	.692	.251	.251	.250	.249	.247	.332
3.981	.692	.251	.252	.251	.250	.248	.332
4.999	.698	.249	.250	.249	.248	.246	.336
6.004	.701	.248	.249	.248	.246	.244	.339
6.978	.705	.246	.248	.247	.245	.243	.341
7.987	.708	.244	.246	.246	.244	.242	.342

Aft-wall static-pressure ratio, $p/p_{t,j}$

NPR	s, in.		
	.200	.300	.400
1.500	.555	.660	.697
1.777	.402	.529	.589
1.756	.414	.537	.598
2.007	.224	.508	.479
2.253	.206	.431	.430
2.498	.201	.399	.402
3.502	.211	.390	.391
4.064	.212	.389	.390
3.981	.212	.389	.390
4.999	.212	.389	.390
6.004	.211	.387	.389
6.978	.211	.387	.390
7.987	.210	.388	.390

Table 16. Ratio of Internal Static Pressure to Jet Total Pressure for Port
With Geometric Reverser Angle of 120°, Port Corner Radius
of 0 in., Constant-Area Duct Geometry, and Blocker Angle of 120°

Forward-wall static-pressure ratio, $p/p_{t,j}$

NPR	s, in.				
	-.050	.050	.100	.200	.382
1.509	.902	.658	.658	.658	.656
1.754	.883	.565	.565	.564	.562
2.011	.869	.491	.491	.490	.487
2.267	.860	.430	.430	.429	.427
2.510	.859	.386	.387	.386	.383
3.014	.852	.315	.315	.313	.309
3.519	.850	.270	.270	.269	.266
4.015	.847	.230	.231	.229	.226
5.010	.845	.163	.163	.161	.158
6.020	.844	.107	.107	.106	.106
7.005	.845	.100	.100	.099	.101
8.029	.846	.098	.097	.097	.099
9.042	.761	.096	.096	.096	.098
9.063	.759	.096	.096	.095	.098

Aft-wall static-pressure ratio, $p/p_{t,j}$

NPR	s, in.						
	-.263	-.063	.037	.137	.237	.337	.437
1.509	.953	.896	.856	.828	.778	.728	.693
1.754	.944	.873	.822	.786	.722	.656	.611
2.011	.940	.855	.798	.756	.683	.605	.559
2.267	.932	.843	.781	.735	.655	.568	.524
2.510	.931	.837	.771	.723	.639	.544	.502
3.014	.928	.826	.756	.704	.615	.509	.470
3.519	.926	.821	.748	.695	.604	.495	.453
4.015	.924	.816	.741	.686	.594	.484	.442
5.010	.921	.810	.731	.675	.583	.472	.427
6.020	.920	.807	.727	.670	.577	.463	.413
7.005	.920	.807	.726	.670	.576	.464	.413
8.029	.921	.808	.725	.670	.577	.464	.413
9.042	.920	.805	.725	.670	.578	.464	.413
9.063	.920	.808	.725	.670	.578	.464	.413

Table 17. Ratio of Internal Static Pressure to Jet Total Pressure for Port
With Geometric Reverser Angle of 120°, Port Corner Radius of
0.109 in., Constant-Area Duct Geometry, and Blocker Angle of 120°

Forward-wall static-pressure ratio, $p/p_{t,j}$

NPR	s, in.									
	-.228	-.171	-.114	-.057	0.000	.050	.100	.201	.301	.401
1.497	.813	.654	.643	.651	.655	.657	.657	.655	.654	.655
1.752	.773	.556	.548	.545	.551	.553	.552	.550	.548	.552
1.753	.773	.557	.547	.546	.551	.552	.551	.550	.547	.552
2.003	.732	.501	.470	.362	.362	.357	.351	.348	.376	.431
2.255	.725	.497	.400	.319	.319	.314	.309	.307	.330	.382
2.505	.721	.492	.353	.280	.280	.275	.270	.271	.296	.345
2.997	.716	.476	.290	.221	.223	.222	.222	.221	.237	.287
3.501	.715	.495	.235	.191	.194	.193	.192	.195	.222	.282
4.005	.715	.490	.196	.185	.188	.188	.187	.190	.220	.281
4.992	.721	.504	.153	.179	.183	.183	.182	.186	.222	.288
6.009	.721	.489	.129	.171	.181	.181	.180	.185	.224	.289
6.961	.722	.499	.114	.167	.179	.178	.178	.185	.227	.291
7.005	.722	.505	.116	.167	.178	.178	.177	.185	.227	.292
7.992	.723	.497	.106	.168	.179	.179	.178	.184	.225	.292
9.016	.723	.510	.111	.167	.178	.178	.177	.183	.225	.293

Aft-wall static-pressure ratio, $p/p_{t,j}$

NPR	s, in.								
	-.443	-.243	-.143	-.043	.057	.157	.257	.357	.457
1.497	.962	.920	.894	.859	.831	.792	.757	.719	.655
1.752	.952	.899	.866	.822	.784	.734	.686	.634	.550
1.753	.953	.899	.866	.822	.784	.733	.686	.634	.550
2.003	.940	.870	.826	.768	.718	.650	.586	.515	.421
2.255	.937	.865	.818	.759	.707	.636	.570	.496	.395
2.505	.935	.860	.813	.752	.698	.626	.558	.482	.382
2.997	.933	.854	.805	.742	.686	.613	.544	.468	.371
3.501	.932	.852	.802	.739	.682	.607	.536	.456	.361
4.005	.932	.853	.802	.738	.681	.607	.535	.454	.359
4.992	.938	.858	.806	.741	.684	.610	.539	.456	.360
6.009	.938	.858	.805	.740	.684	.610	.540	.456	.359
6.961	.939	.859	.805	.740	.684	.610	.541	.457	.361
7.005	.938	.858	.805	.740	.683	.610	.540	.457	.360
7.992	.939	.859	.805	.740	.683	.610	.541	.458	.362
9.016	.938	.860	.804	.739	.683	.610	.542	.458	.362

Table 18. Ratio of Internal Static Pressure to Jet Total Pressure for Port
With Geometric Reverser Angle of 120°, Port Corner
Radius of 0.109 in., Constant-Area Duct Geometry, Blocker
Angle of 120°, and Modified Passage Length of 0.15 in.

Forward-wall static-pressure ratio, $p/P_{t,j}$

NPR	s, in.						
	-.228	-.171	-.114	-.057	0.000	.050	.100
1.509	.810	.650	.652	.655	.659	.660	.660
1.760	.772	.569	.558	.559	.564	.565	.565
2.011	.752	.527	.488	.487	.493	.494	.494
2.248	.740	.523	.433	.434	.438	.440	.440
2.500	.733	.510	.389	.390	.392	.393	.392
2.998	.725	.510	.324	.322	.327	.328	.328
3.511	.720	.509	.275	.273	.276	.274	.273
4.021	.718	.507	.239	.236	.241	.241	.241
5.018	.716	.506	.189	.183	.191	.191	.191
6.015	.715	.502	.157	.144	.157	.157	.157
7.023	.715	.489	.135	.122	.133	.133	.133
8.025	.716	.501	.121	.103	.114	.115	.114
9.011	.716	.502	.112	.082	.099	.100	.099

Aft-wall static-pressure ratio, $p/P_{t,j}$

NPR	s, in.				
	-.443	-.243	-.143	-.043	.057
1.509	.958	.914	.882	.841	.777
1.760	.951	.894	.857	.806	.726
2.011	.945	.882	.841	.785	.698
2.248	.942	.875	.831	.772	.685
2.500	.940	.869	.825	.764	.676
2.998	.937	.863	.816	.754	.665
3.511	.935	.859	.811	.747	.658
4.021	.934	.856	.807	.742	.652
5.018	.932	.853	.804	.738	.647
6.015	.931	.852	.801	.735	.645
7.023	.930	.850	.798	.732	.643
8.025	.930	.850	.796	.730	.641
9.011	.930	.850	.795	.729	.639

Table 19. Ratio of Internal Static Pressure to Jet Total Pressure for Port With Geometric Reverser Angle of 120°, Port Corner Radius of 0.109 in., Constant-Area Duct Geometry, Blocker Angle of 120°, and Modified Passage Length of 0.31 in.

Forward-wall static-pressure ratio, $p/p_{t,j}$

NPR	s, in.							
	-.228	-.171	-.114	-.057	0.000	.050	.100	.201
1.506	.809	.647	.635	.654	.657	.659	.659	.658
1.762	.770	.563	.539	.551	.556	.558	.558	.557
2.024	.746	.520	.463	.472	.477	.477	.477	.476
2.261	.730	.511	.397	.389	.389	.388	.385	.388
2.507	.725	.523	.352	.362	.363	.364	.362	.363
3.010	.723	.511	.292	.303	.309	.310	.310	.308
3.514	.717	.507	.240	.251	.253	.254	.253	.252
4.005	.714	.497	.204	.206	.208	.207	.206	.207
5.044	.708	.499	.154	.112	.118	.117	.115	.133
6.005	.708	.488	.131	.102	.110	.108	.107	.127
7.017	.710	.501	.124	.095	.108	.106	.105	.127
8.100	.712	.504	.132	.086	.106	.105	.105	.127
9.068	.713	.501	.130	.078	.105	.105	.104	.127

Aft-wall static-pressure ratio, $p/p_{t,j}$

NPR	s, in.						
	-.443	-.243	-.143	-.043	.057	.157	.257
1.506	.964	.918	.888	.866	.821	.772	.719
1.762	.956	.898	.861	.832	.776	.715	.647
2.024	.950	.884	.842	.809	.746	.679	.608
2.261	.943	.872	.825	.789	.720	.650	.584
2.507	.941	.870	.821	.783	.713	.640	.576
3.010	.944	.867	.816	.775	.702	.626	.565
3.514	.945	.862	.809	.766	.691	.612	.554
4.005	.942	.859	.804	.759	.681	.598	.540
5.044	.936	.850	.792	.747	.668	.583	.527
6.005	.932	.847	.788	.743	.665	.578	.524
7.017	.932	.847	.787	.743	.665	.578	.523
8.100	.932	.848	.787	.743	.665	.578	.523
9.068	.934	.848	.787	.743	.665	.577	.522

Table 20. Ratio of Internal Static Pressure to Jet Total Pressure for Port
With Geometric Reverser Angle of 120°, Port Corner
Radius of 0 in., Constant-Area Duct Geometry, Blocker
Angle of 120°, and Forward Passage Wall Removed

Forward-wall static-pressure ratio, $p/p_{t,j}$

NPR	s, in.					
	-.050	.050	.100	.150	.200	.250
1.511	.905	.661	.661	.661	.670	.661
1.760	.635	.567	.567	.567	.574	.567
2.024	.872	.492	.493	.492	.499	.492
2.272	.864	.438	.438	.437	.445	.437
2.510	.859	.396	.396	.395	.403	.395
3.000	.853	.330	.330	.329	.337	.329
3.513	.849	.280	.281	.280	.287	.280
4.008	.847	.245	.245	.245	.252	.244
4.994	.845	.195	.196	.195	.202	.195
6.005	.844	.161	.161	.161	.168	.160
7.000	.844	.137	.137	.136	.144	.136
7.996	.845	.117	.117	.117	.126	.115
8.975	.845	.100	.099	.099	.101	.098
9.031	.846	.099	.099	.098	.099	.097

Aft-wall static-pressure ratio, $p/p_{t,j}$

NPR	s, in.						
	-.263	-.063	.037	.137	.237	.337	.437
1.511	.955	.897	.856	.831	.781	.729	.695
1.760	.944	.872	.821	.790	.724	.657	.613
2.024	.937	.854	.796	.760	.684	.607	.561
2.272	.933	.843	.780	.741	.658	.574	.529
2.510	.930	.835	.769	.728	.641	.550	.505
3.000	.926	.825	.754	.710	.618	.521	.473
3.513	.923	.818	.745	.698	.604	.503	.454
4.008	.922	.814	.738	.690	.596	.493	.444
4.994	.920	.809	.731	.682	.587	.482	.429
6.005	.919	.805	.725	.675	.579	.474	.423
7.000	.918	.804	.722	.671	.574	.468	.415
7.996	.917	.803	.721	.671	.573	.465	.409
8.975	.916	.803	.719	.671	.574	.466	.410
9.031	.916	.803	.719	.671	.574	.466	.410

Table 21. Ratio of Internal Static Pressure to Jet Total Pressure for Port
With Geometric Reverser Angle of 120°, Port Corner Radius
of 0 in., Constant-Area Duct Geometry, and Blocker Angle of 75°

Forward-wall static-pressure ratio, $p/p_{t,j}$

NPR	s, in.				
	-.050	.050	.100	.200	.382
1.521	.903	.653	.652	.652	.651
1.767	.884	.561	.560	.559	.558
2.003	.872	.492	.492	.491	.490
2.251	.863	.432	.433	.431	.429
2.505	.854	.390	.390	.388	.386
3.006	.847	.315	.315	.313	.308
3.509	.843	.274	.274	.273	.270
4.012	.841	.235	.235	.234	.231
5.013	.839	.176	.175	.174	.170
6.021	.837	.104	.104	.103	.101
7.020	.837	.090	.090	.089	.089
8.028	.843	.088	.088	.086	.087
9.026	.757	.086	.086	.085	.086

Aft-wall static-pressure ratio, $p/p_{t,j}$

NPR	s, in.						
	-.263	-.063	.037	.137	.237	.337	.437
1.521	.960	.903	.862	.832	.779	.725	.688
1.767	.961	.881	.829	.791	.724	.655	.605
2.003	.958	.866	.808	.764	.688	.610	.559
2.251	.954	.855	.792	.744	.662	.574	.526
2.505	.947	.847	.779	.730	.643	.548	.503
3.006	.945	.836	.764	.710	.618	.512	.471
3.509	.944	.831	.756	.701	.607	.497	.456
4.012	.944	.827	.750	.693	.598	.487	.445
5.013	.941	.820	.741	.683	.587	.476	.431
6.021	.942	.817	.734	.675	.578	.464	.414
7.020	.942	.816	.732	.674	.578	.464	.415
8.028	.945	.819	.734	.675	.580	.466	.416
9.026	.945	.820	.733	.676	.581	.466	.416

32

Table 22. Ratio of Internal Static Pressure to Jet Total Pressure for Port
With Geometric Reverser Angle of 120°, Port Corner Radius
of 0 in., Convergent-Section Geometry, and Blocker Angle of 120°

Forward-wall static-pressure ratio, $p/p_{t,j}$

NPR	s, in.					
	-.100	.150	.200	.250	.300	.400
1.493	.943	.665	.670	.665	.664	.669
1.689	.931	.587	.592	.587	.586	.591
1.946	.921	.508	.514	.507	.509	.513
2.183	.918	.451	.458	.450	.450	.457
2.425	.914	.404	.413	.403	.403	.411
2.919	.909	.333	.343	.332	.331	.341
3.393	.902	.284	.295	.284	.282	.293
3.866	.901	.246	.259	.245	.245	.257
4.842	.899	.183	.207	.182	.181	.204
5.825	.897	.096	.096	.096	.094	.168
6.792	.897	.085	.085	.085	.084	.145
7.779	.898	.084	.084	.084	.083	.126
8.749	.900	.084	.084	.084	.083	.113

Aft-wall static-pressure ratio, $p/p_{t,j}$

NPR	s, in.				
	-.090	.110	.210	.310	.410
1.493	.916	.831	.791	.743	.592
1.639	.859	.744	.744	.634	.617
1.946	.604	.763	.703	.629	.542
2.183	.875	.744	.680	.595	.497
2.425	.466	.724	.665	.571	.471
2.919	.860	.712	.643	.540	.443
3.393	.853	.700	.631	.523	.427
3.866	.849	.643	.623	.510	.417
4.842	.844	.654	.613	.492	.404
5.825	.537	.672	.602	.473	.390
6.792	.838	.673	.603	.474	.388
7.779	.838	.674	.603	.475	.389
8.749	.635	.675	.603	.476	.389

Table 23. Ratio of Internal Static Pressure to Jet Total Pressure for Port
With Geometric Reverser Angle of 120°, Port Corner Radius of
0.047 in., Convergent-Section Geometry, and Blocker Angle of 120°

Forward-wall static-pressure ratio, $p/p_{t,j}$

NPR	s, in.								
	-.115	-.077	-.038	0.000	.050	.100	.150	.250	.350
1.455	.825	.686	.679	.680	.681	.681	.681	.679	.678
1.705	.781	.586	.576	.578	.578	.578	.578	.576	.574
1.954	.754	.511	.499	.501	.500	.500	.500	.497	.495
2.203	.737	.453	.437	.438	.438	.438	.437	.435	.433
2.431	.727	.410	.392	.394	.394	.393	.393	.391	.388
2.923	.714	.340	.317	.317	.316	.315	.315	.312	.308
3.428	.705	.289	.257	.255	.254	.253	.252	.249	.245
3.899	.701	.254	.206	.202	.202	.201	.200	.197	.194
4.868	.697	.238	.136	.137	.137	.137	.137	.134	.135
5.798	.697	.216	.131	.132	.132	.132	.132	.130	.130
5.832	.697	.222	.131	.132	.132	.132	.132	.130	.130
6.815	.697	.235	.129	.130	.130	.130	.130	.128	.129
7.771	.698	.230	.128	.130	.130	.130	.129	.128	.128
8.740	.699	.253	.129	.130	.130	.129	.129	.128	.128

Aft-wall static-pressure ratio, $p/p_{t,j}$

NPR	s, in.				
	-.090	.110	.210	.310	.410
1.455	.907	.826	.792	.750	.706
1.705	.879	.774	.728	.669	.607
1.954	.860	.740	.686	.611	.530
2.203	.850	.716	.659	.572	.482
2.431	.840	.702	.643	.549	.461
2.923	.829	.680	.621	.512	.432
3.428	.822	.667	.608	.487	.413
3.899	.818	.657	.599	.470	.398
4.868	.809	.643	.587	.456	.388
5.798	.808	.643	.585	.455	.387
5.832	.807	.642	.585	.455	.386
6.815	.808	.643	.585	.455	.386
7.771	.808	.643	.585	.455	.387
8.740	.809	.644	.585	.455	.387

Table 24. Ratio of Internal Static Pressure to Jet Total Pressure for Port
With Geometric Reverser Angle of 120°, Port Corner Radius of
0.109 in., Convergent-Section Geometry, and Blocker Angle of 120°

Forward-wall static-pressure ratio, $p/p_{t,j}$

NPR	s, in.									
	-.266	-.178	-.089	0.000	.050	.100	.150	.200	.300	.382
1.457	.796	.650	.653	.673	.674	.674	.673	.673	.672	.671
1.701	.746	.542	.550	.570	.570	.570	.569	.569	.566	.567
1.945	.688	.383	.383	.369	.367	.361	.357	.356	.361	.431
2.184	.675	.347	.300	.306	.302	.293	.289	.292	.328	.395
2.444	.670	.323	.271	.280	.278	.272	.269	.268	.293	.348
2.913	.663	.308	.232	.242	.242	.241	.241	.239	.244	.281
3.392	.660	.304	.210	.221	.221	.220	.220	.218	.227	.275
3.875	.659	.303	.206	.215	.216	.215	.214	.213	.223	.273
4.850	.660	.300	.196	.212	.212	.211	.210	.209	.220	.272
5.816	.660	.297	.189	.209	.209	.208	.207	.206	.220	.276
6.780	.661	.298	.184	.208	.208	.207	.205	.205	.221	.279
7.740	.662	.298	.173	.207	.207	.206	.204	.204	.222	.280
8.742	.662	.298	.171	.207	.207	.206	.204	.204	.222	.281

Aft-wall static-pressure ratio, $p/p_{t,j}$

NPR	s, in.		
	-.090	.110	.410
1.457	.902	.824	.707
1.701	.870	.776	.607
1.945	.830	.719	.416
2.184	.816	.704	.390
2.444	.812	.699	.384
2.913	.806	.690	.376
3.392	.803	.687	.376
3.875	.802	.684	.378
4.850	.800	.681	.380
5.816	.798	.678	.382
6.780	.797	.675	.382
7.740	.797	.674	.383
8.742	.796	.673	.363

Table 25. Ratio of Internal Static Pressure to Jet Total Pressure for Port
With Geometric Reverser Angle of 135°, Port Corner Radius
of 0 in., Constant-Area Duct Geometry, and Blocker Angle of 135°

Forward-wall static-pressure ratio, $p/p_{t,j}$

NPR	s, in.						
	-.050	.050	.100	.150	.200	.300	.400
1.497	.891	.667	.666	.666	.665	.666	.665
1.756	.866	.569	.567	.567	.566	.566	.565
2.002	.853	.496	.494	.494	.493	.493	.492
2.250	.842	.438	.437	.436	.436	.435	.433
2.507	.835	.389	.387	.387	.386	.386	.383
3.005	.826	.315	.314	.313	.313	.311	.307
3.509	.821	.253	.252	.252	.251	.249	.243
3.997	.817	.184	.182	.183	.182	.179	.175
4.999	.812	.095	.093	.095	.094	.092	.092
6.023	.813	.084	.083	.084	.084	.082	.084
7.031	.813	.082	.082	.082	.082	.081	.082
8.005	.815	.079	.079	.079	.079	.078	.080
9.007	.812	.078	.077	.078	.077	.077	.078

Aft-wall static-pressure ratio, $p/p_{t,j}$

NPR	s, in.										
	-1.082	-.941	-.800	-.570	-.370	-.270	-.070	.030	.130	.230	.330
1.497	.999	1.002	1.004	.995	.979	.962	.912	.880	.827	.777	.739
1.756	.999	1.003	1.004	.993	.971	.952	.888	.845	.778	.715	.664
2.002	1.001	1.005	1.007	.995	.968	.946	.873	.823	.748	.675	.616
2.250	1.001	1.005	1.006	1.000	.965	.941	.861	.807	.726	.647	.582
2.507	1.002	1.006	1.006	.999	.962	.937	.853	.796	.711	.627	.559
3.005	1.002	1.006	1.006	.996	.959	.931	.842	.780	.691	.602	.529
3.509	1.002	1.006	1.006	.998	.957	.928	.834	.770	.678	.586	.510
3.997	1.003	1.007	1.007	.996	.955	.924	.826	.760	.666	.573	.494
4.999	1.004	1.007	1.007	.994	.953	.921	.818	.749	.652	.557	.475
6.023	1.004	1.007	1.007	.995	.953	.920	.817	.748	.652	.557	.474
7.031	1.005	1.007	1.007	.994	.954	.920	.817	.747	.652	.557	.474
8.005	1.005	1.007	1.007	.994	.954	.920	.818	.746	.651	.557	.474
9.007	1.002	1.005	1.004	.992	.953	.919	.818	.745	.650	.556	.472

Table 26. Ratio of Internal Static Pressure to Jet Total Pressure for Port With Geometric Reverser Angle of 135°, Port Corner Radius of 0.109 in., Constant-Area Duct Geometry, and Blocker Angle of 135°

Forward-wall static-pressure ratio, $p/p_{t,j}$

NPR	s, in.								
	-.257	-.193	-.128	-.064	0.000	.050	.100	.200	.300
1.502	.791	.642	.655	.659	.660	.660	.661	.659	.658
1.502	.792	.642	.655	.659	.660	.660	.661	.659	.658
1.758	.746	.544	.551	.558	.559	.560	.560	.558	.556
1.998	.720	.477	.469	.481	.483	.482	.482	.480	.478
2.490	.684	.395	.321	.325	.325	.323	.321	.317	.322
2.240	.695	.421	.370	.377	.377	.375	.372	.369	.373
2.995	.674	.372	.236	.241	.241	.239	.237	.235	.242
3.497	.668	.358	.174	.185	.186	.186	.185	.183	.192
3.994	.666	.353	.150	.172	.172	.172	.171	.169	.181
5.002	.665	.349	.125	.163	.163	.163	.162	.160	.173
5.991	.665	.349	.111	.159	.160	.159	.158	.156	.171
7.005	.665	.347	.104	.156	.156	.156	.155	.153	.167
8.023	.666	.348	.101	.153	.154	.153	.152	.150	.165
8.994	.666	.349	.098	.151	.152	.151	.150	.148	.164

Aft-wall static-pressure ratio, $p/p_{t,j}$

| NPR	s, in.														
	-1.342	-1.201	-1.060	-.830	-.630	-.530	-.330	-.230	-.130	-.030	.070	.170	.270	.370	.470
1.502	.995	.999	1.002	.998	.989	.982	.954	.924	.905	.876	.824	.795	.747	.711	.631
1.502	.994	1.000	1.001	.999	.989	.982	.954	.925	.905	.876	.823	.795	.747	.711	.631
1.758	.994	.999	1.002	.999	.986	.976	.941	.906	.878	.843	.775	.738	.675	.626	.516
1.998	.994	1.000	1.003	1.000	.983	.972	.931	.893	.860	.822	.742	.700	.626	.568	.443
2.490	.994	1.000	1.003	.998	.979	.966	.916	.866	.831	.787	.690	.641	.552	.482	.362
2.240	.994	1.000	1.003	.998	.981	.968	.922	.873	.840	.797	.705	.658	.572	.505	.390
2.995	.995	1.000	1.003	.999	.977	.962	.909	.855	.818	.773	.669	.619	.525	.453	.332
3.497	.996	1.001	1.002	.999	.977	.961	.905	.848	.809	.763	.656	.607	.513	.442	.322
3.994	.995	1.001	1.002	1.000	.976	.960	.903	.846	.807	.760	.652	.601	.507	.436	.317
5.002	.996	1.001	1.003	1.001	.977	.960	.902	.845	.805	.757	.649	.597	.503	.431	.313
5.991	.997	1.002	1.003	1.001	.978	.960	.901	.844	.804	.756	.648	.596	.501	.429	.312
7.005	.997	1.001	1.003	1.001	.978	.960	.901	.843	.803	.755	.647	.594	.498	.426	.312
8.023	.997	1.002	1.003	1.001	.979	.960	.901	.843	.802	.754	.647	.593	.497	.424	.311
8.994	.997	1.002	1.003	1.000	.979	.960	.901	.845	.801	.753	.646	.592	.496	.422	.308

Table 27. Ratio of Internal Static Pressure to Jet Total Pressure for Port
With Geometric Reverser Angle of 135°, Port Corner Radius
of 0 in., Constant-Area Duct Geometry, and Blocker Angle of 90°

Forward-wall static-pressure ratio, $p/p_{t,j}$

NPR	s, in.						
	-.050	.050	.100	.150	.200	.300	.400
1.499	.907	.673	.672	.671	.671	.671	.670
1.750	.886	.578	.577	.576	.576	.575	.575
2.020	.871	.501	.500	.499	.499	.498	.497
2.270	.862	.444	.443	.442	.441	.441	.440
2.516	.855	.396	.395	.395	.394	.394	.392
3.005	.847	.322	.322	.321	.321	.320	.316
3.510	.840	.244	.243	.243	.242	.240	.234
4.023	.837	.187	.186	.186	.185	.182	.179
5.023	.834	.095	.093	.094	.094	.092	.093
6.027	.835	.088	.087	.088	.088	.087	.088
7.001	.836	.087	.086	.087	.086	.086	.087
8.007	.841	.086	.085	.086	.085	.085	.086
8.997	.837	.085	.084	.085	.084	.084	.085

Aft-wall static-pressure ratio, $p/p_{t,j}$

NPR	s, in.							
	-.570	-.370	-.270	-.070	.030	.130	.230	.330
1.499	.997	.970	.954	.906	.872	.825	.780	.742
1.750	.994	.962	.942	.882	.838	.779	.720	.671
2.020	.992	.956	.934	.864	.814	.746	.677	.620
2.270	.991	.952	.928	.853	.798	.724	.649	.587
2.516	.991	.949	.923	.845	.787	.709	.629	.564
3.005	.990	.945	.918	.833	.771	.688	.604	.533
3.510	.990	.942	.913	.823	.758	.671	.583	.508
4.023	.987	.941	.910	.817	.751	.661	.571	.494
5.023	.988	.939	.906	.810	.741	.648	.556	.476
6.027	.986	.940	.906	.810	.740	.648	.555	.476
7.001	.986	.940	.907	.810	.739	.648	.554	.476
8.007	.989	.944	.909	.812	.740	.649	.558	.477
8.997	.986	.942	.907	.811	.739	.647	.558	.475

Table 28. Ratio of Internal Static Pressure to Jet Total Pressure for Port
With Geometric Reverser Angle of 135°, Port Corner Radius
of 0 in., Convergent-Section Geometry, and Blocker Angle of 135°

Forward-wall static-pressure ratio, $p/p_{t,j}$

| NPR | s, in. |
	-.100	.100	.150	.200	.250	.300	.400
1.506	.937	.666	.666	.658	.656	.658	.666
1.759	.922	.571	.570	.560	.560	.560	.570
2.004	.911	.501	.500	.490	.489	.489	.500
2.275	.903	.441	.440	.426	.426	.426	.441
2.510	.901	.399	.398	.379	.378	.377	.399
3.020	.891	.332	.332	.278	.276	.273	.332
3.511	.886	.285	.285	.193	.191	.188	.285
4.003	.884	.250	.250	.121	.121	.118	.250
5.005	.884	.200	.200	.094	.094	.093	.200
5.998	.885	.167	.167	.086	.086	.085	.167
7.006	.886	.143	.143	.083	.083	.082	.143
7.985	.888	.125	.125	.080	.080	.079	.125
9.009	.889	.111	.111	.079	.079	.078	.111

Aft-wall static-pressure ratio, $p/p_{t,j}$

| NPR | s, in. |
	-.866	-.725	-.584	-.354	-.154	-.054	.046	.246	.346	.446
1.506	1.002	1.002	.998	.986	.929	.894	.842	.759	.709	.687
1.759	1.002	1.003	.999	.975	.911	.867	.800	.693	.624	.596
2.004	1.000	1.001	.998	.970	.899	.848	.774	.650	.566	.534
2.275	1.000	1.001	.997	.968	.889	.834	.754	.617	.521	.483
2.510	1.003	1.004	.999	.966	.884	.826	.741	.598	.496	.453
3.020	1.001	1.001	.996	.960	.871	.808	.717	.564	.458	.405
3.511	1.001	1.002	.995	.956	.864	.798	.703	.546	.439	.382
4.003	1.001	1.002	.995	.955	.859	.791	.694	.537	.430	.373
5.005	1.003	1.002	.996	.954	.859	.789	.689	.530	.424	.368
5.998	1.003	1.003	.996	.954	.860	.789	.687	.527	.421	.364
7.006	1.003	1.003	.996	.955	.860	.790	.686	.526	.420	.363
7.985	1.003	1.003	.996	.955	.861	.790	.686	.526	.419	.362
9.009	1.004	1.003	.996	.955	.862	.791	.686	.526	.419	.362

Table 29. Ratio of Internal Static Pressure to Jet Total Pressure for Port
With Geometric Reverser Angle of 135°, Port Corner Radius of
0.047 in., Convergent-Section Geometry, and Blocker Angle of 135°

Forward-wall static-pressure ratio, $p/p_{t,j}$

NPR	s, in.									
	-.127	-.085	-.042	0.000	.050	.100	.150	.200	.300	.400
1.529	.813	.632	.612	.638	.639	.636	.637	.636	.634	.653
1.748	.780	.547	.539	.558	.554	.552	.552	.552	.549	.571
2.002	.756	.464	.471	.487	.472	.470	.470	.469	.467	.499
2.253	.739	.393	.416	.431	.403	.401	.401	.400	.397	.443
2.503	.729	.330	.361	.382	.343	.341	.340	.339	.335	.398
2.994	.716	.279	.289	.315	.239	.237	.236	.234	.230	.333
3.492	.709	.266	.207	.256	.144	.144	.142	.141	.141	.285
4.007	.706	.262	.167	.218	.115	.116	.114	.115	.115	.248
5.030	.706	.262	.123	.168	.106	.106	.105	.105	.105	.198
5.975	.707	.265	.103	.138	.104	.104	.103	.103	.103	.166
7.025	.707	.265	.092	.116	.103	.102	.102	.102	.101	.142
8.026	.708	.265	.086	.102	.102	.102	.102	.101	.101	.124
9.038	.706	.263	.098	.094	.103	.103	.102	.102	.101	.110

Aft-wall static-pressure ratio, $p/p_{t,j}$

NPR	s, in.									
	-.866	-.725	-.584	-.354	-.154	-.054	.046	.246	.346	.446
1.529	1.002	1.001	.998	.977	.914	.874	.821	.740	.692	.672
1.748	1.003	1.003	.999	.968	.897	.848	.783	.681	.617	.591
2.002	1.003	1.004	.999	.963	.881	.825	.750	.630	.548	.515
2.253	1.003	1.003	.998	.959	.868	.809	.726	.597	.503	.465
2.503	1.004	1.004	.997	.955	.859	.796	.709	.573	.477	.433
2.994	1.004	1.004	.995	.948	.847	.779	.687	.545	.446	.395
3.492	1.005	1.004	.995	.943	.838	.767	.672	.530	.431	.381
4.007	1.005	1.004	.995	.944	.835	.763	.663	.518	.422	.373
5.030	1.006	1.004	.995	.943	.836	.763	.661	.513	.416	.368
5.975	1.007	1.005	.996	.945	.837	.764	.660	.512	.414	.366
7.025	1.006	1.004	.996	.944	.838	.764	.659	.511	.413	.365
8.026	1.006	1.004	.995	.943	.838	.764	.658	.511	.413	.363
9.038	1.003	1.001	.993	.942	.838	.763	.656	.510	.413	.363

Table 30. Ratio of Internal Static Pressure to Jet Total Pressure for Port
With Geometric Reverser Angle of 135°, Port Corner Radius of
0.109 in., Convergent-Section Geometry, and Blocker Angle of 135°

Forward-wall static-pressure ratio, $p/p_{t,j}$

NPR	s, in.									
	-.295	-.221	-.147	-.074	0.000	.050	.100	.150	.250	.350
1.500	.769	.555	.601	.617	.617	.617	.616	.614	.610	.608
1.748	.723	.441	.473	.504	.505	.504	.502	.499	.494	.497
2.013	.694	.407	.378	.390	.390	.390	.388	.386	.382	.391
2.252	.678	.383	.299	.303	.303	.303	.303	.300	.297	.307
2.520	.667	.370	.234	.234	.234	.234	.234	.232	.231	.246
3.008	.659	.364	.172	.172	.172	.171	.172	.169	.174	.218
3.510	.658	.364	.164	.165	.164	.164	.164	.161	.166	.219
4.024	.658	.363	.159	.162	.162	.161	.161	.158	.163	.218
5.015	.658	.363	.154	.160	.160	.160	.159	.157	.161	.216
6.019	.659	.364	.148	.159	.159	.159	.158	.156	.160	.216
7.006	.660	.364	.146	.158	.159	.159	.157	.155	.159	.217
7.998	.662	.364	.146	.158	.159	.159	.157	.155	.160	.217
8.997	.663	.364	.146	.159	.159	.159	.158	.156	.160	.217

Aft-wall static-pressure ratio, $p/p_{t,j}$

NPR	s, in.								
	-.866	-.725	-.584	-.354	-.154	-.054	.046	.246	.346	.446
1.500	.999	.999	.993	.958	.893	.851	.796	.722	.679	.672
1.748	.999	.999	.993	.945	.866	.813	.744	.642	.576	.568
2.013	1.000	.999	.990	.935	.843	.782	.701	.586	.499	.465
2.252	1.000	.999	.988	.929	.828	.763	.677	.554	.466	.424
2.520	1.000	.999	.987	.927	.818	.749	.659	.535	.448	.402
3.008	1.001	.999	.986	.921	.811	.741	.650	.525	.436	.388
3.510	1.001	.999	.986	.921	.809	.740	.648	.523	.435	.389
4.024	1.001	.999	.986	.921	.809	.739	.646	.522	.434	.389
5.015	1.003	1.000	.987	.922	.810	.739	.644	.521	.432	.388
6.019	1.003	1.000	.987	.923	.810	.739	.643	.520	.431	.388
7.006	1.003	1.000	.987	.923	.811	.739	.641	.520	.431	.388
7.998	1.003	1.000	.987	.923	.811	.739	.641	.520	.431	.387
8.997	1.003	1.000	.987	.922	.812	.739	.640	.521	.431	.387

Table 31. Ratio of Internal Static Pressure to Jet Total Pressure for Port
With Geometric Reverser Angle of 135°, Port Corner Radius of
0 in., Convergent-Section Geometry, and Blocker Angle of 90°

Forward-wall static-pressure ratio, $p/p_{t,j}$

NPR	s, in.						
	-.100	.100	.150	.200	.250	.300	.400
1.563	.943	.640	.640	.639	.640	.639	.640
1.749	.934	.573	.572	.572	.571	.571	.572
2.002	.926	.500	.500	.498	.498	.498	.500
2.264	.920	.442	.442	.438	.438	.438	.442
2.517	.916	.398	.397	.389	.388	.388	.398
2.999	.908	.334	.333	.259	.259	.256	.334
3.492	.905	.286	.286	.183	.182	.180	.286
4.026	.903	.248	.248	.100	.099	.097	.248
5.050	.904	.198	.198	.085	.085	.083	.198
6.006	.905	.166	.166	.084	.084	.082	.166
7.012	.906	.142	.142	.077	.077	.076	.142
7.992	.907	.125	.125	.076	.076	.075	.125
9.040	.909	.110	.110	.075	.076	.075	.110

Aft-wall static-pressure ratio, $p/p_{t,j}$

NPR	s, in.						
	-.354	-.154	-.054	.046	.246	.346	.446
1.563	.980	.927	.889	.836	.750	.695	.668
1.749	.978	.914	.870	.808	.704	.638	.605
2.002	.977	.902	.852	.781	.660	.580	.546
2.264	.976	.893	.839	.762	.629	.537	.500
2.517	.974	.887	.829	.748	.608	.509	.467
2.999	.970	.874	.809	.721	.566	.462	.409
3.492	.969	.868	.800	.708	.550	.445	.391
4.026	.968	.863	.793	.696	.538	.434	.379
5.050	.969	.863	.793	.694	.535	.429	.374
6.006	.969	.864	.793	.693	.535	.428	.373
7.012	.969	.865	.794	.692	.534	.426	.371
7.992	.969	.866	.795	.692	.534	.426	.371
9.040	.968	.867	.795	.692	.535	.426	.370

Table 32. Ratio of Internal Static Pressure to Jet Total Pressure for Port
With Geometric Reverser Angle of 135°, Port Corner Radius
of 0 in., Convergent-Section Geometry, and Blocker Angle of 120°

Forward-wall static-pressure ratio, $p/p_{t,j}$

NPR		s, in.					
	-.100	.100	.150	.200	.250	.300	.400
1.507	.942	.664	.663	.663	.662	.663	.664
1.743	.932	.576	.575	.572	.572	.574	.575
2.019	.921	.496	.495	.493	.493	.495	.496
2.251	.916	.444	.444	.438	.437	.444	.444
2.503	.908	.400	.399	.351	.349	.394	.399
3.009	.906	.332	.332	.250	.248	.281	.332
3.499	.902	.236	.285	.157	.156	.225	.286
3.929	.901	.254	.254	.100	.100	.100	.254
4.992	.902	.200	.200	.087	.088	.087	.200
6.013	.903	.166	.166	.085	.085	.084	.166
7.008	.905	.142	.142	.083	.084	.083	.142
7.995	.906	.125	.125	.082	.083	.082	.125
9.027	.903	.110	.110	.082	.083	.082	.110

Aft-wall static-pressure ratio, $p/p_{t,j}$

NPR	s, in.						
	-.354	-.154	-.054	.046	.246	.346	.446
1.507	.978	.926	.892	.843	.762	.714	.687
1.743	.972	.908	.866	.805	.702	.638	.604
2.018	.966	.894	.845	.774	.654	.575	.539
2.251	.962	.886	.833	.757	.625	.536	.497
2.503	.956	.874	.816	.734	.588	.491	.442
3.009	.956	.866	.802	.714	.560	.461	.404
3.499	.954	.859	.793	.701	.543	.442	.383
3.929	.952	.855	.788	.693	.534	.435	.377
4.992	.953	.856	.787	.690	.530	.431	.372
6.013	.955	.857	.788	.689	.529	.430	.371
7.008	.954	.658	.788	.689	.529	.429	.370
7.995	.954	.859	.788	.688	.529	.429	.369
9.027	.952	.858	.787	.686	.528	.427	.368

Table 33. Ratio of Internal Static Pressure to Jet Total Pressure for Port
With Geometric Reverser Angle of 135°, Port Corner Radius of 0 in.,
Convergent-Section Geometry, and Blocker Angle of 135°/90°

Forward-wall static-pressure ratio, $p/p_{t,j}$

NPR	s, in.						
	-.100	.100	.150	.200	.250	.300	.400
1.556	.945	.644	.643	.641	.641	.641	.644
1.765	.934	.568	.567	.565	.565	.565	.568
2.004	.926	.500	.499	.497	.497	.496	.500
2.259	.919	.444	.443	.432	.429	.429	.443
2.528	.911	.396	.395	.331	.330	.327	.396
3.007	.906	.332	.332	.238	.237	.233	.332
3.511	.903	.285	.285	.150	.150	.146	.285
4.010	.902	.249	.249	.099	.099	.096	.249
4.996	.899	.200	.200	.091	.091	.089	.200
5.988	.900	.167	.167	.089	.089	.088	.166
7.007	.901	.143	.142	.088	.088	.087	.142
7.998	.907	.125	.125	.084	.084	.083	.125
9.014	.908	.111	.110	.084	.084	.083	.111

Aft-wall static-pressure ratio, $p/p_{t,j}$

NPR	s, in.								
	-.725	-.584	-.354	-.154	-.054	.046	.246	.346	.446
1.556	.999	.995	.977	.923	.886	.835	.750	.697	.670
1.765	.998	.995	.967	.907	.864	.802	.700	.633	.599
2.004	.997	.993	.962	.895	.846	.776	.659	.580	.545
2.259	.996	.991	.959	.884	.831	.754	.624	.533	.493
2.528	.996	.990	.953	.871	.813	.728	.585	.485	.435
3.007	.996	.988	.949	.863	.800	.711	.561	.458	.403
3.511	.996	.988	.946	.857	.791	.700	.547	.441	.384
4.010	.995	.987	.944	.853	.786	.691	.538	.434	.378
4.996	.993	.985	.942	.852	.784	.688	.534	.429	.374
5.988	.993	.986	.942	.852	.785	.686	.533	.428	.373
7.007	.994	.987	.944	.854	.785	.686	.533	.428	.373
7.998	.997	.989	.947	.856	.788	.687	.534	.428	.373
9.014	.997	.989	.948	.857	.788	.687	.534	.428	.373
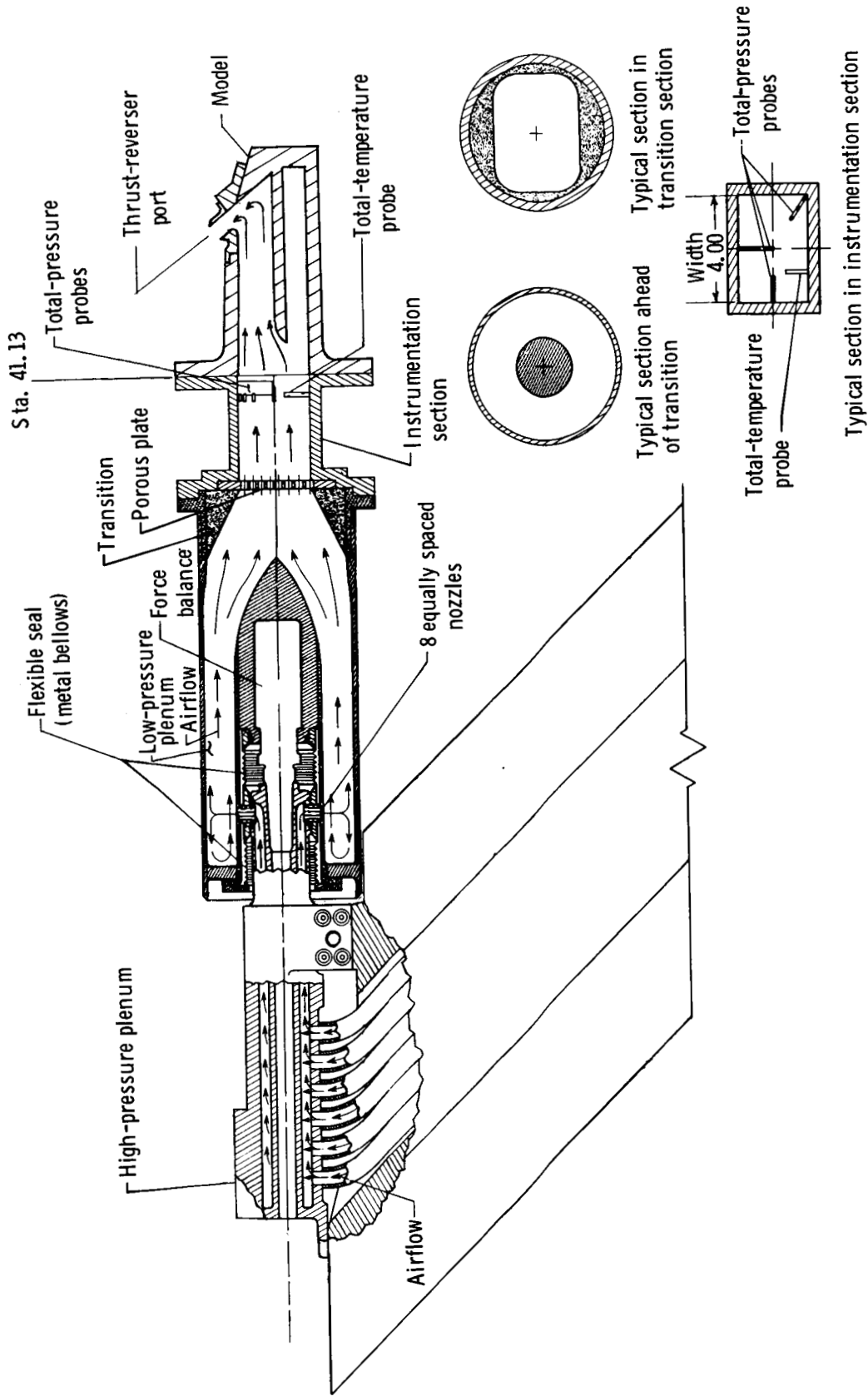
(a) Air-powered nacelle test apparatus.

Figure 1. Air-powered nacelle model with port installed and schematic of nonmetric-to-metric air transfer system. All dimensions are in inches unless otherwise indicated.

Mounted on balance (metric)

Mounted on support system (nonmetric)

Low-pressure plenum

Sta. 29.39

M

N

F

Balance

Bellows

8 multiholed nozzles

High-pressure flow

Balance cable
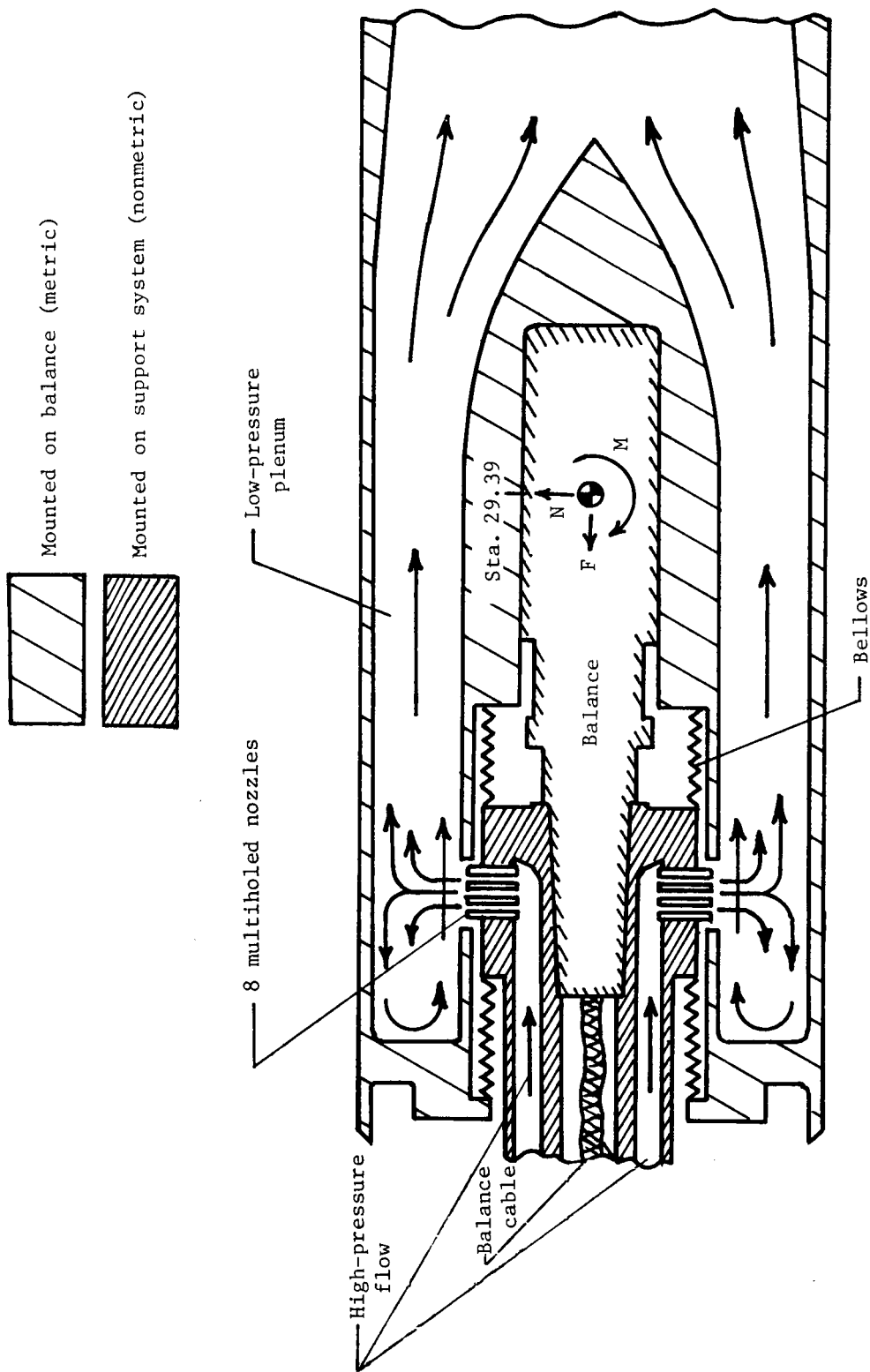
(b) Schematic cross section of flow transfer system.

Figure 1. Concluded.
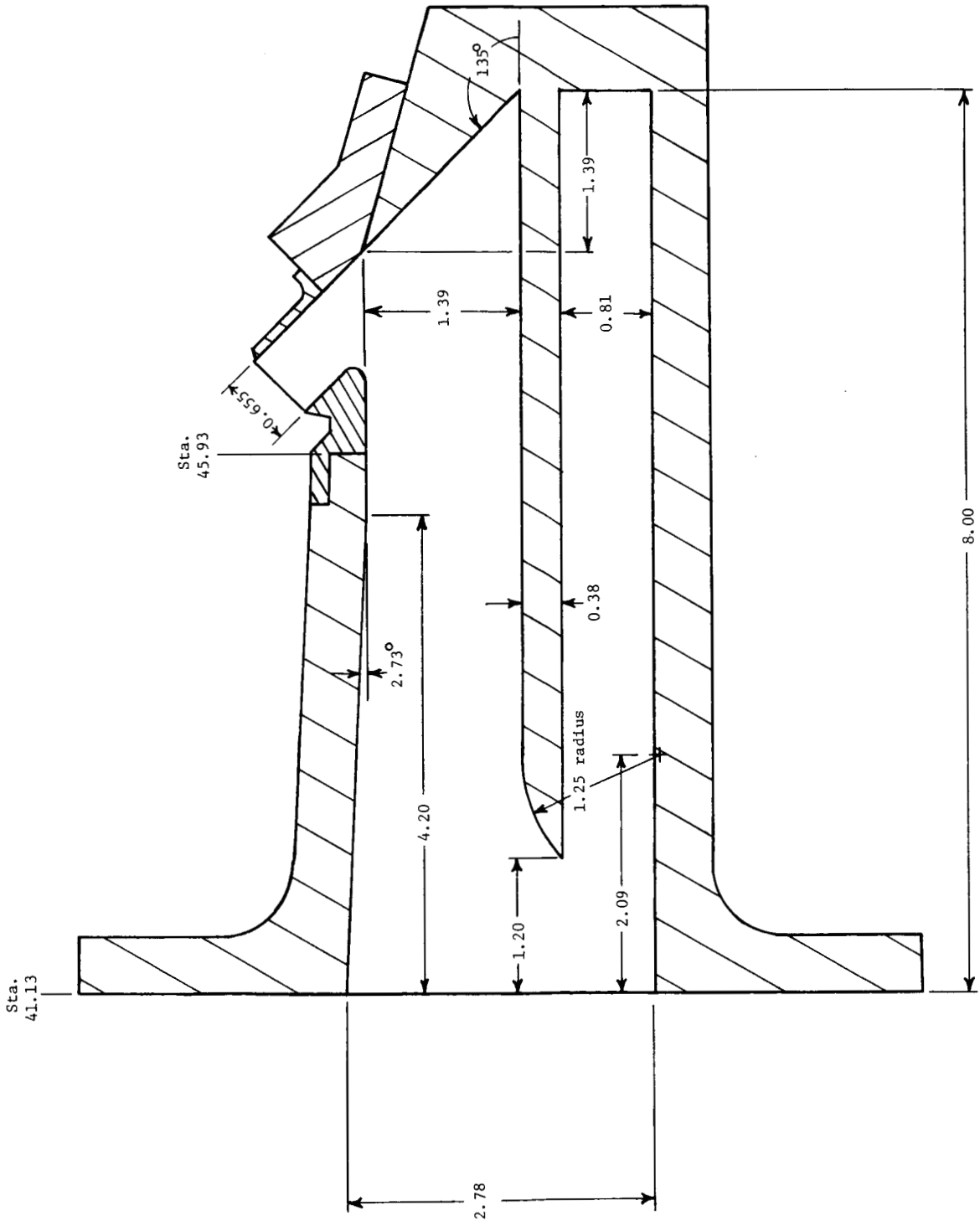
Figure 2. Model internal geometry with typical port (135°) components installed. All dimensions are in inches unless otherwise indicated.
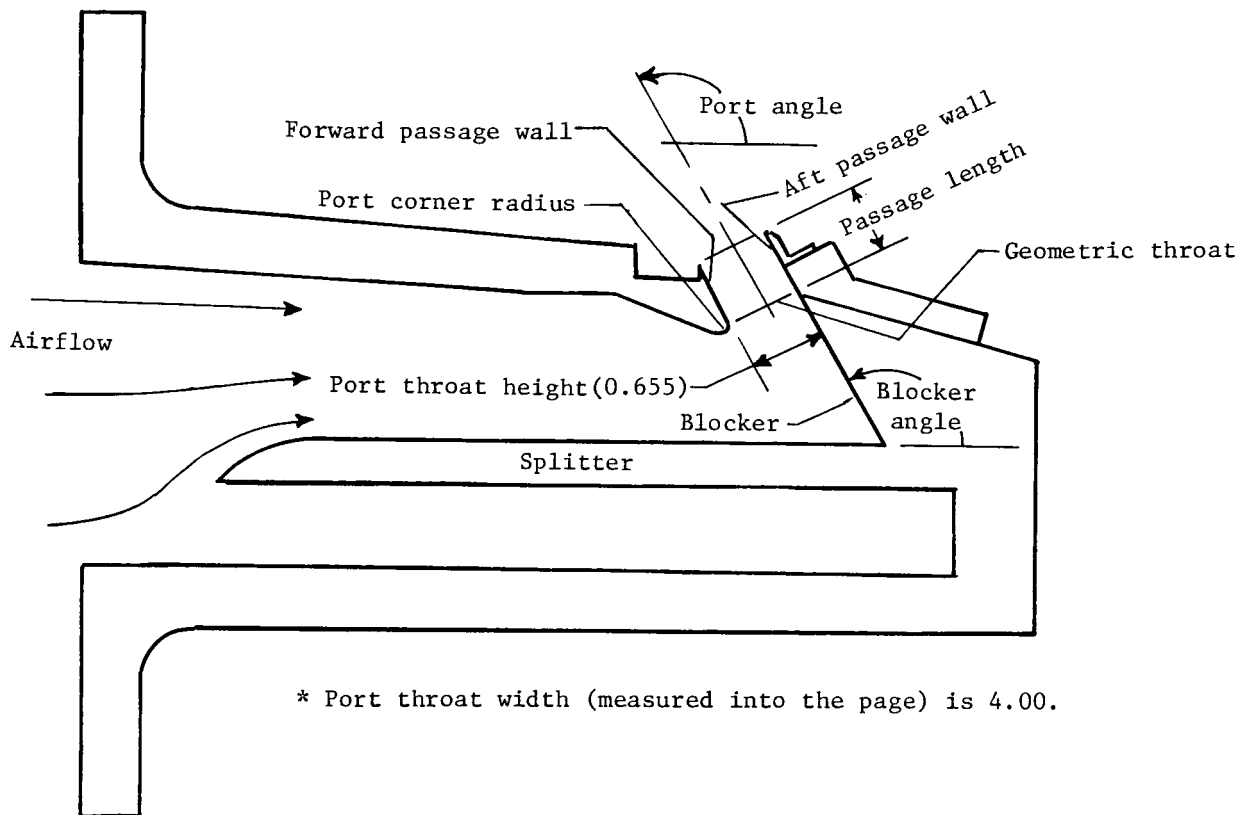
(a) Model nomenclature.

Figure 3. Model nomenclature and schematics of two reverser-port locations. All dimensions are in inches unless otherwise indicated.

Nozzle in forward-thrust configuration
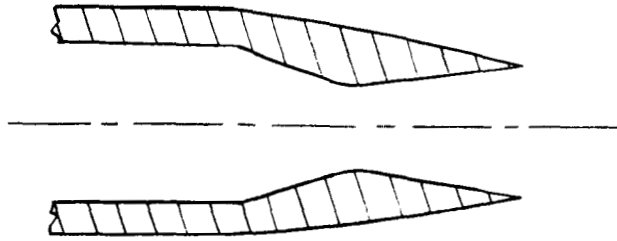
Nozzle in reverse thrust with port openings in constant-area duct
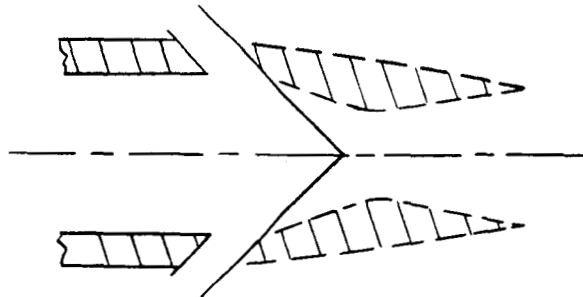
Nozzle in reverse thrust with port openings in convergent section
of the nozzle
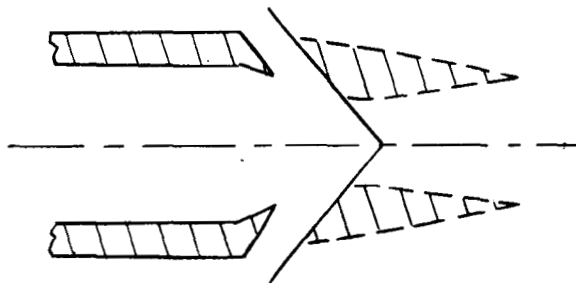
(b) Schematics of a nozzle in forward- and reverse-thrust configurations.

Figure 3. Concluded.
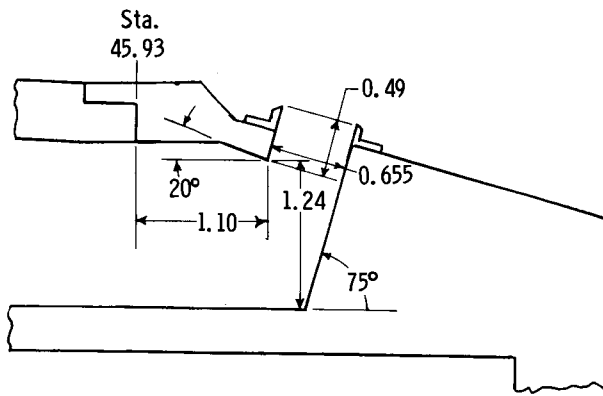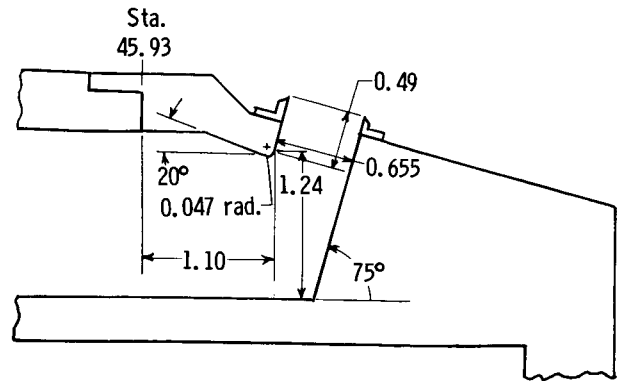
49

(a) Port in convergent section; port corner radius of 0.

(b) Port in convergent section; port corner radius of 0.047 in.
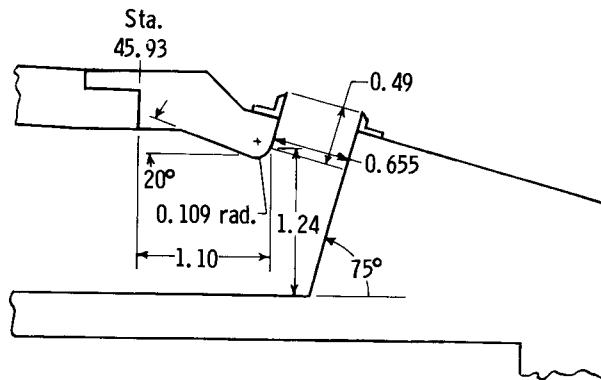
(c) Port in convergent section; port corner radius of 0.109 in.
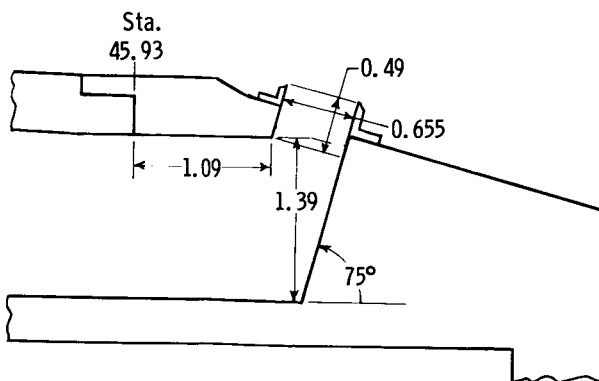
(d) Port in constant-area duct; port corner radius of 0.
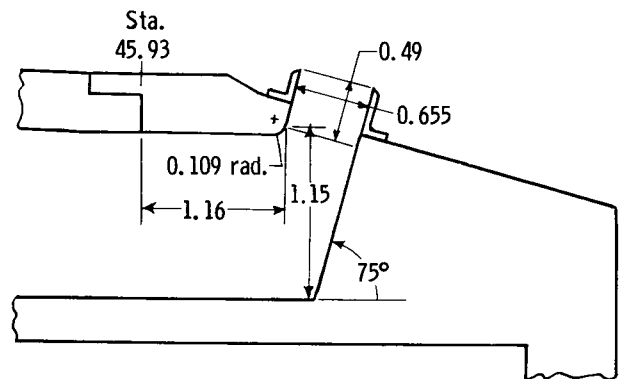
(e) Port in constant-area duct; port corner radius of 0.109 in.

Figure 4. Geometry of five basic 75° thrust-reverser ports with 75° blocker angles. All dimensions are in inches unless otherwise indicated.
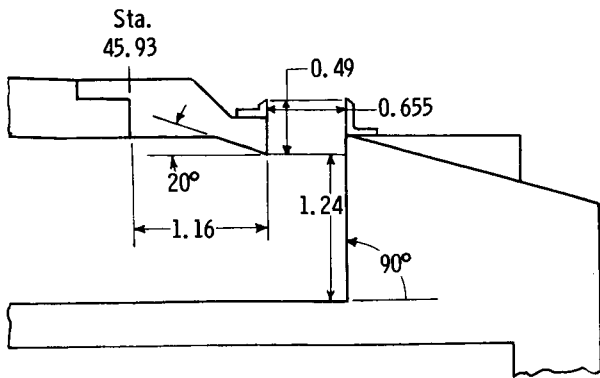
(a) Port in convergent section; port corner radius of 0.
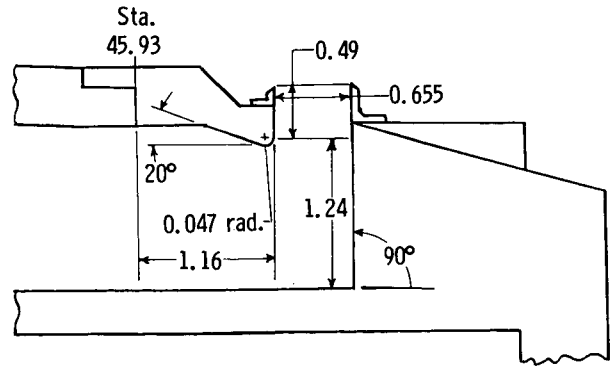
(b) Port in convergent section; port corner radius of 0.047 in.
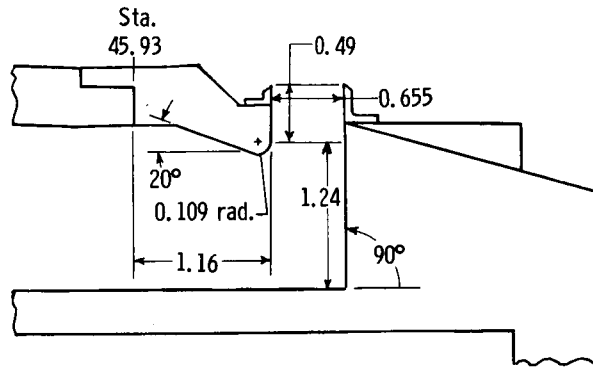
(c) Port in convergent section; port corner radius of 0.109 in.
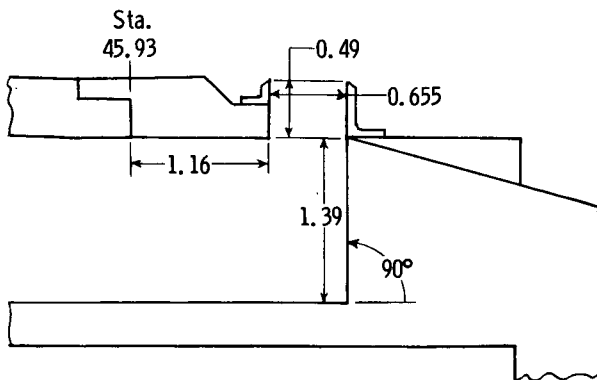
(d) Port in constant-area duct; port corner radius of 0.
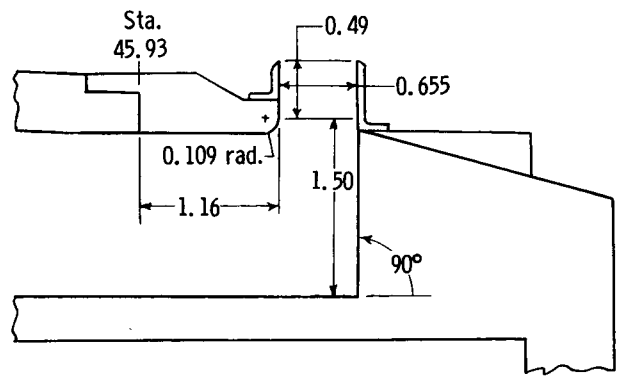
(e) Port in constant-area duct; port corner radius of 0.109 in.

Figure 5. Geometry of five basic 90° thrust-reverser ports with 90° blocker angles. All dimensions are in inches unless otherwise indicated.
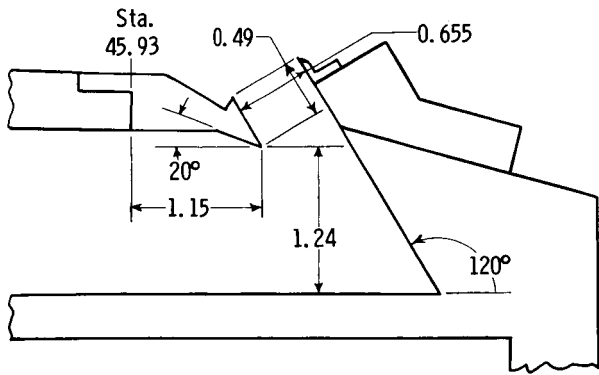
(a) Port in convergent section; port corner radius of 0.
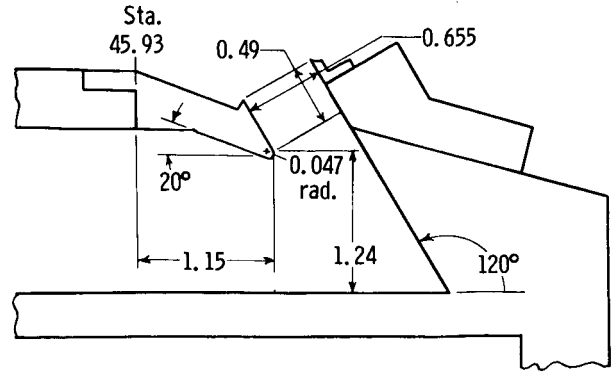
(b) Port in convergent section; port corner radius of 0.047 in.
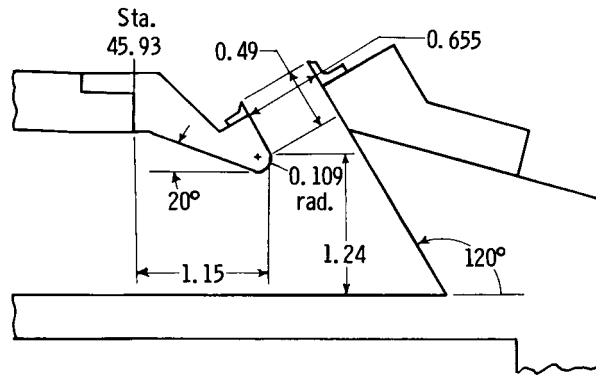
(c) Port in convergent section; port corner radius of 0.109 in.
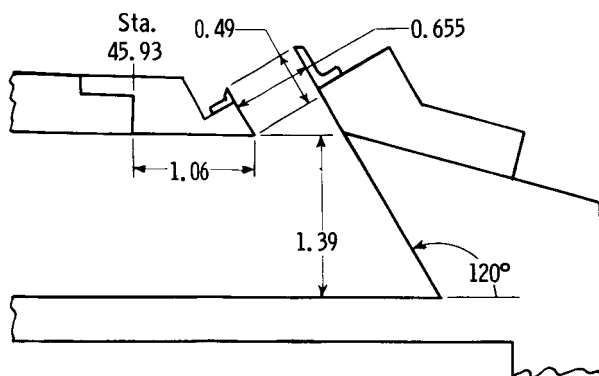
(d) Port in constant-area duct; port corner radius of 0.
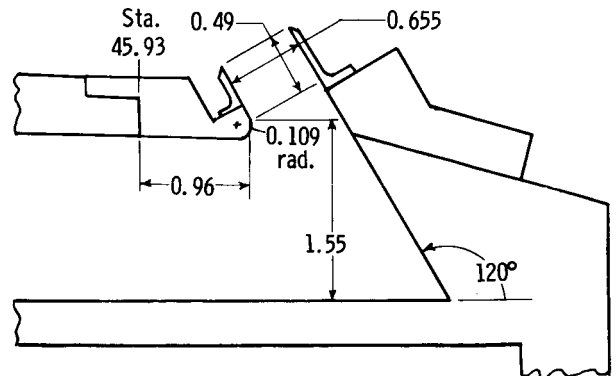
(e) Port in constant-area duct; port corner radius of 0.109 in.

Figure 6. Geometry of five basic 120° thrust-reverser ports with 120° blocker angles. All dimensions are in inches unless otherwise indicated.
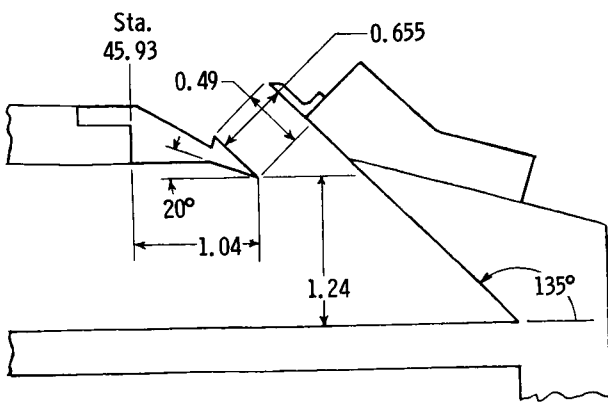
(a) Port in convergent section; port corner radius of 0.
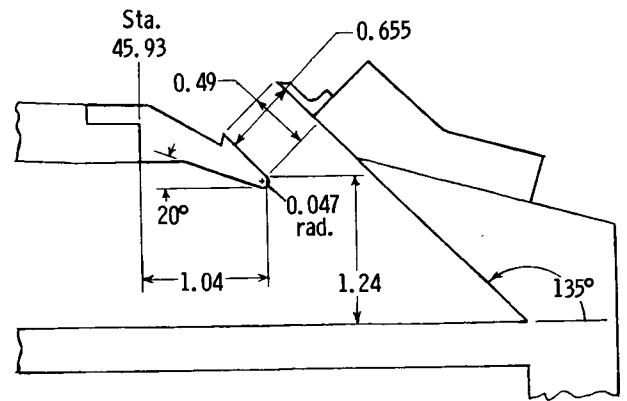
(b) Port in convergent section; port corner radius of 0.047 in.
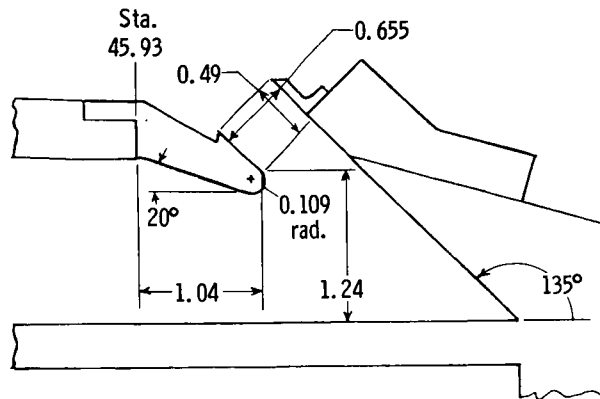
(c) Port in convergent section; port corner radius of 0.109 in.
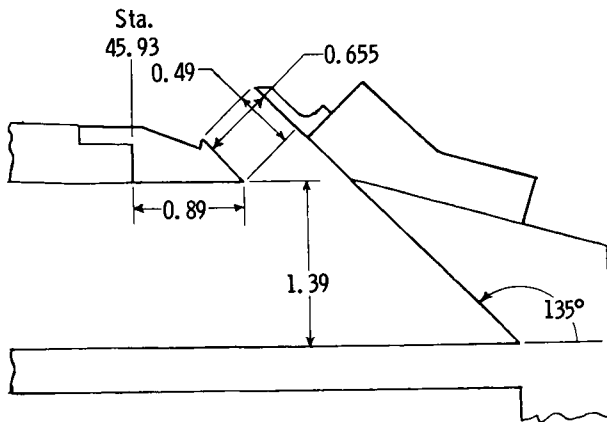
(d) Port in constant-area duct; port corner radius of 0.
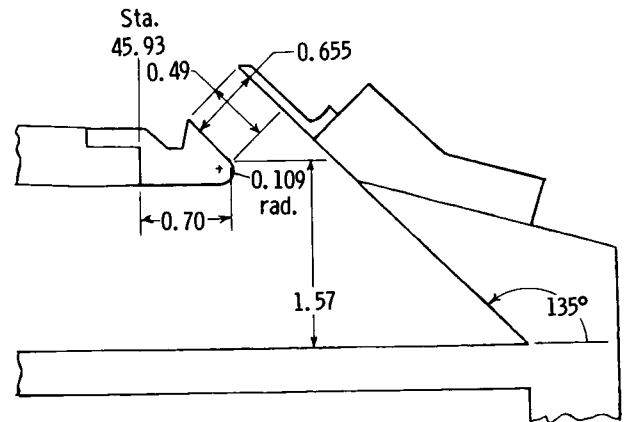
(e) Port in constant-area duct; port corner radius of 0.109 in.

Figure 7. Geometry of five basic 135° thrust-reverser ports with 135° blocker angles. All dimensions are in inches unless otherwise indicated.

Figure 8. Four blocker geometries for 90° thrust-reverser port with port corner radius of 0.109 in. in constant-area duct. All dimensions are in inches unless otherwise indicated.
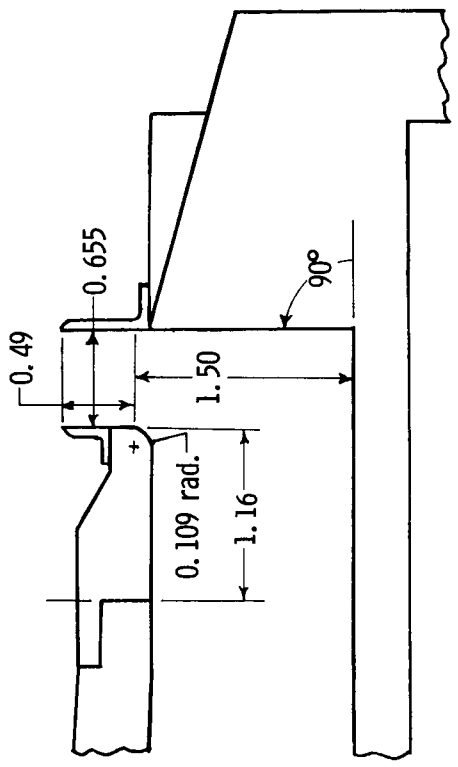
90° Blocker angle
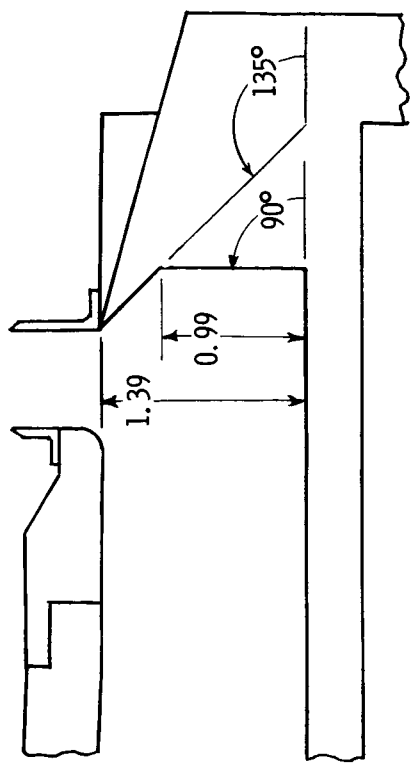
135°/90° Blocker angles
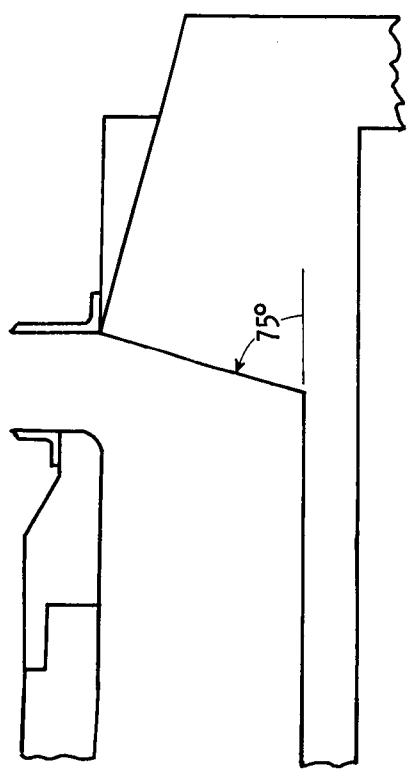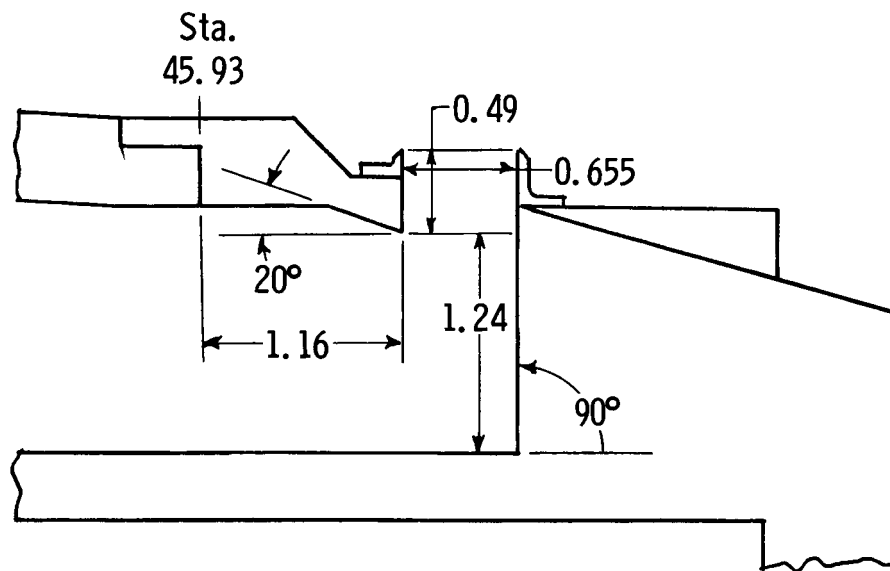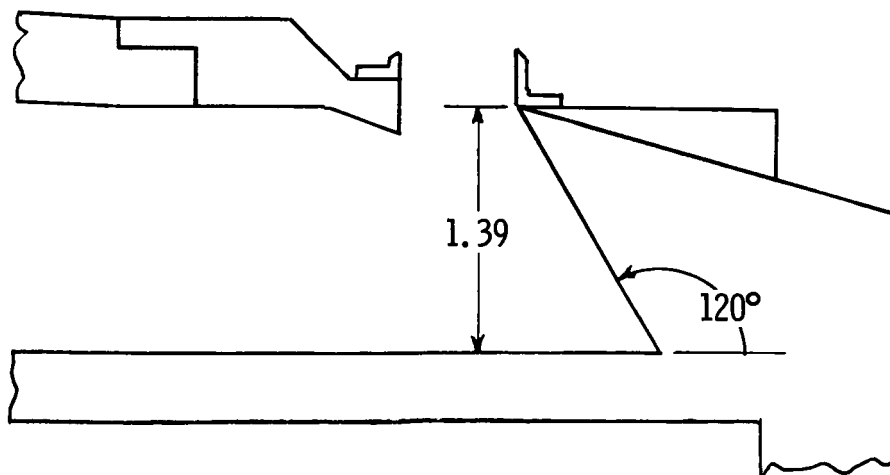
75° Blocker angle

120° Blocker angle

Figure 9. Two blocker geometries for 90° thrust-reverser port with port corner radius of 0 in. in converging section. All dimensions are in inches unless otherwise indicated.
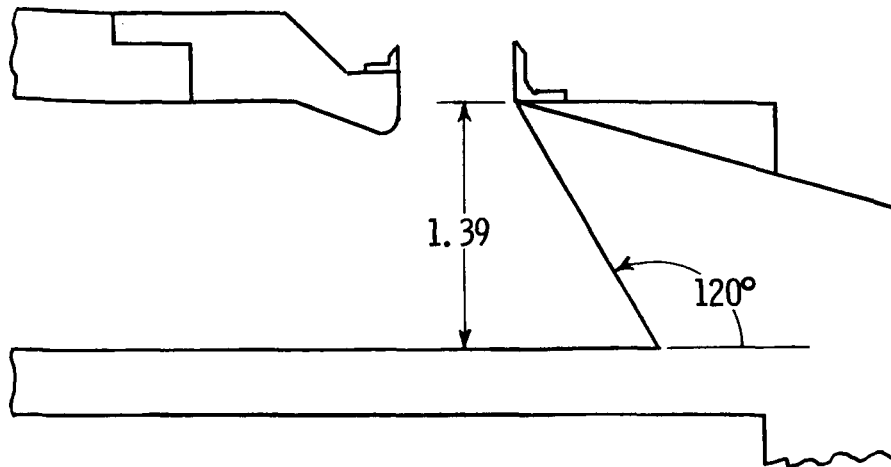
Figure 10. Two blocker geometries for 90° thrust-reverser port with port corner radius of 0.047 in. in converging section. All dimensions are in inches unless otherwise indicated.
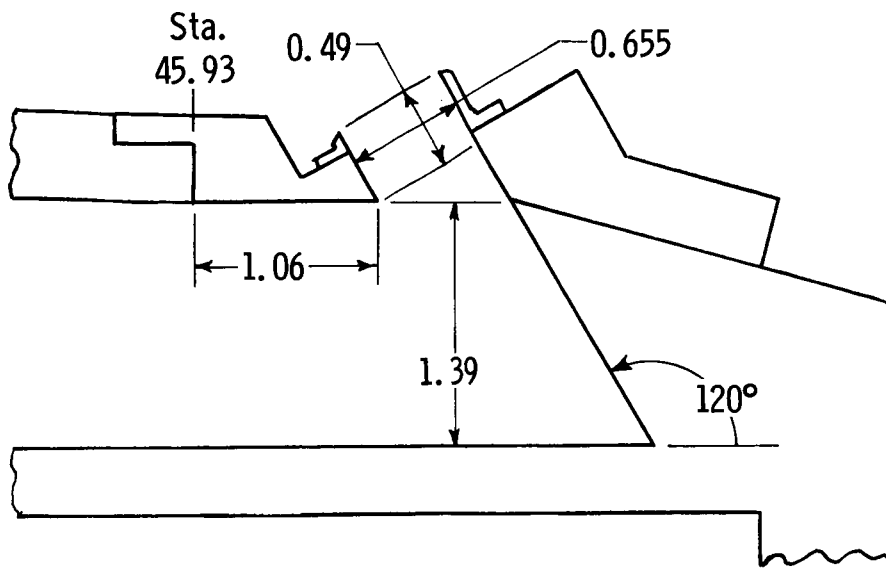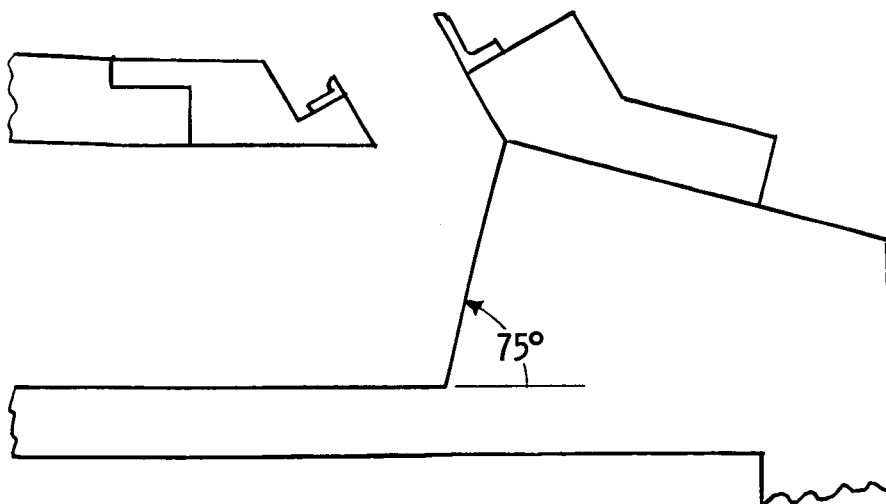
120° Blocker angle

75° Blocker angle

Figure 11. Two blocker geometries for 120° thrust-reverser port with port corner radius of 0 in. in constant-area duct. All dimensions are in inches unless otherwise indicated.

120° Blocker angle

90° Blocker angle

135°/90° Blocker angles
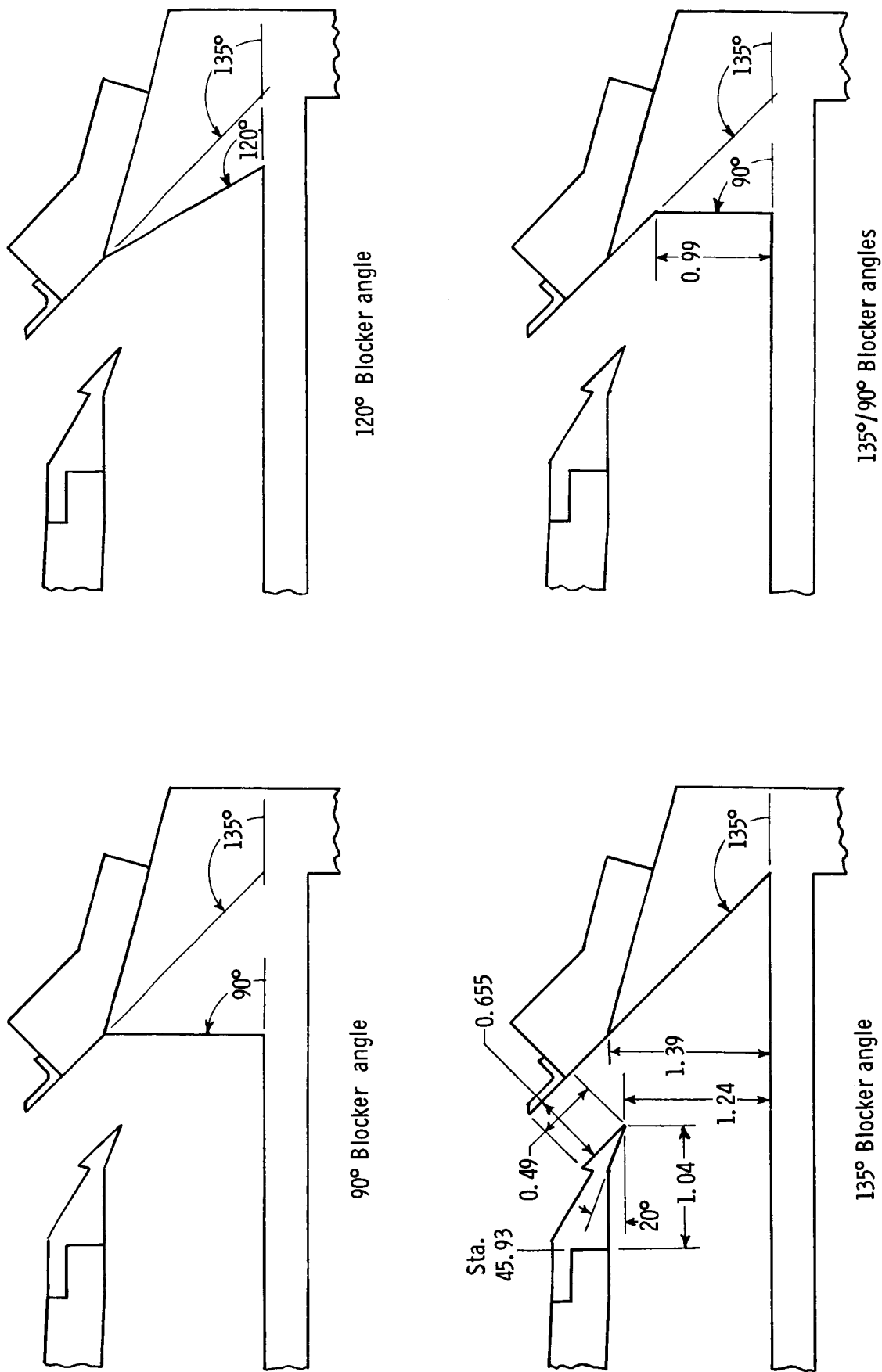
135° Blocker angle

Figure 12. Four blocker geometries for 135° thrust-reverser port with port corner radius of 0 in. in converging section. All dimensions are in inches unless otherwise indicated.
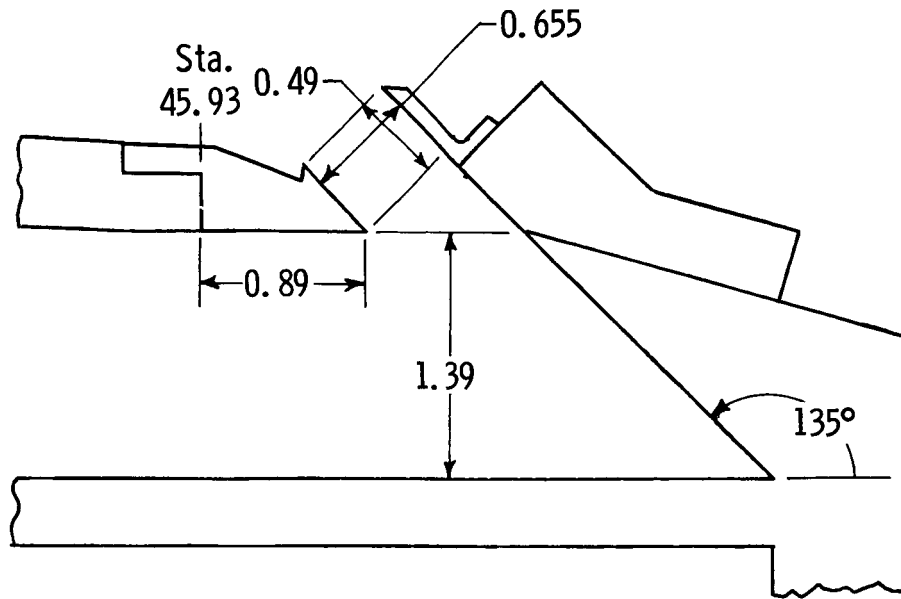
135° Blocker angle
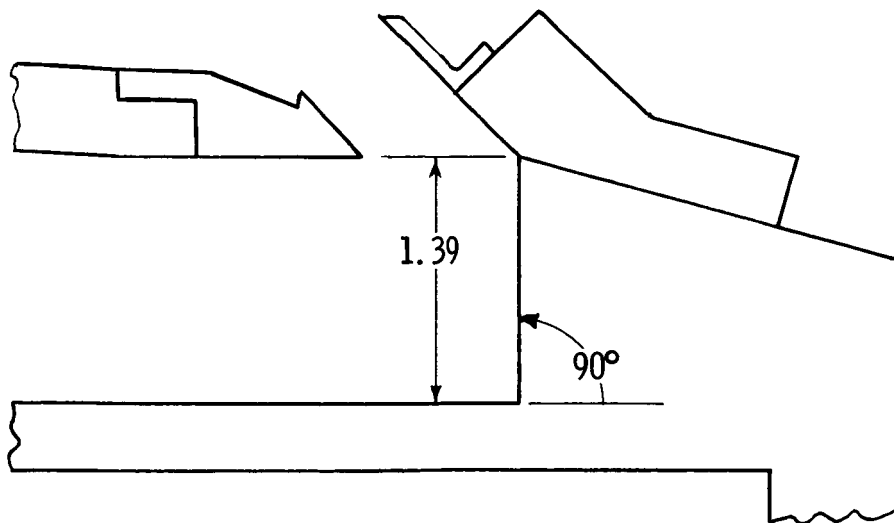
90° Blocker angle

Figure 13. Two blocker geometries for 135° thrust-reverser port with port corner radius of 0 in. in constant-area duct. All dimensions are in inches unless otherwise indicated.
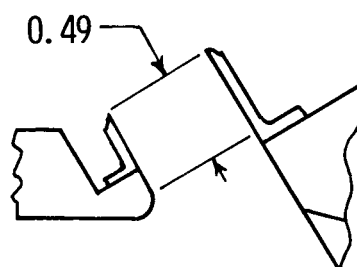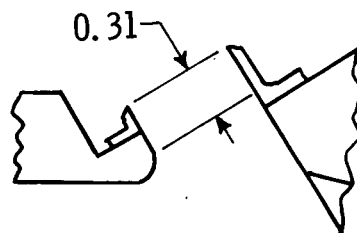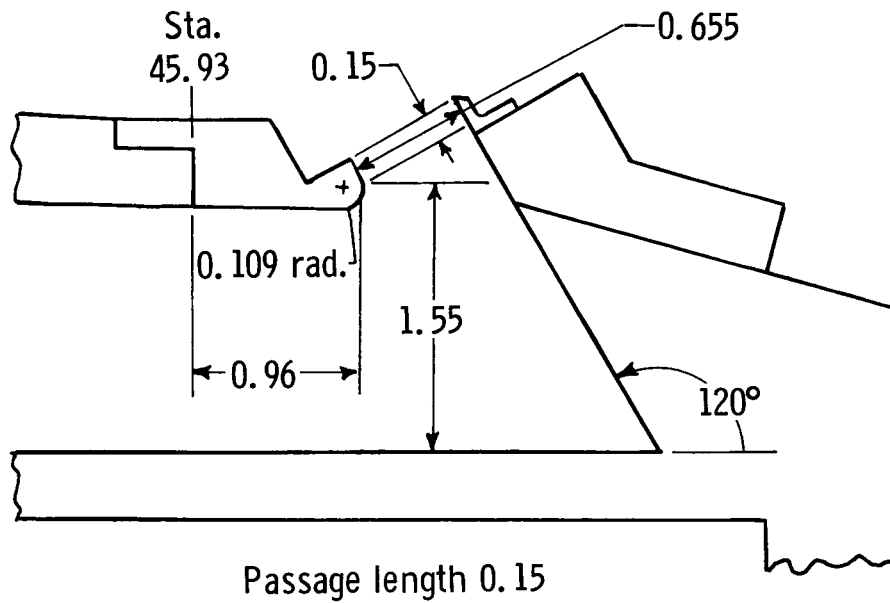
Figure 14. Three port-passage lengths for 120° thrust-reverser port with port corner radius of 0.109 in. in constant-area duct. All dimensions are in inches unless otherwise indicated.

Sta. 45.93

0.49

0.655

1.06

1.39

120°

0.49

0.33
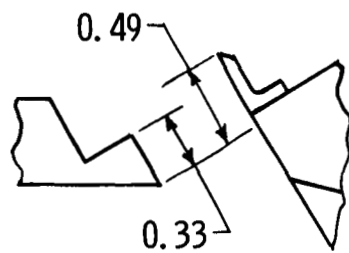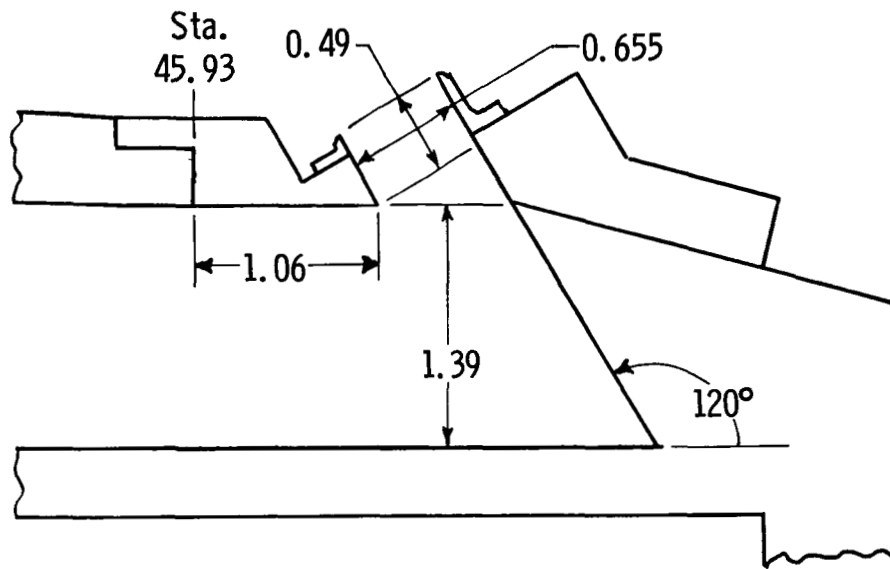
**Portion of forward passage
wall removed**

Figure 15. Passage geometry for 120° thrust-reverser port in constant-area duct having port corner radius of 0 in. with and without portion of forward passage wall. All dimensions are in inches unless otherwise indicated.
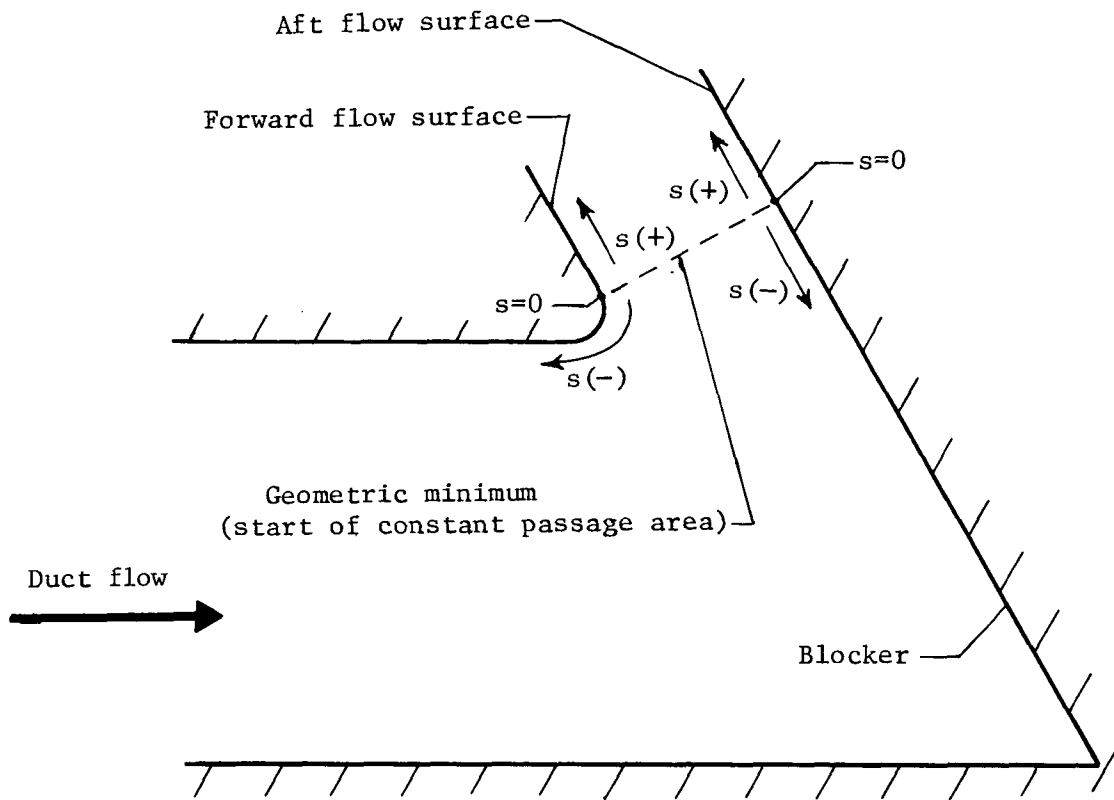
Figure 16. Coordinate system used to measure location of pressure orifices on forward and aft flow surfaces relative to port geometric minimum area.

Port corner radius, in.

○   0
□   .047
◇   .109
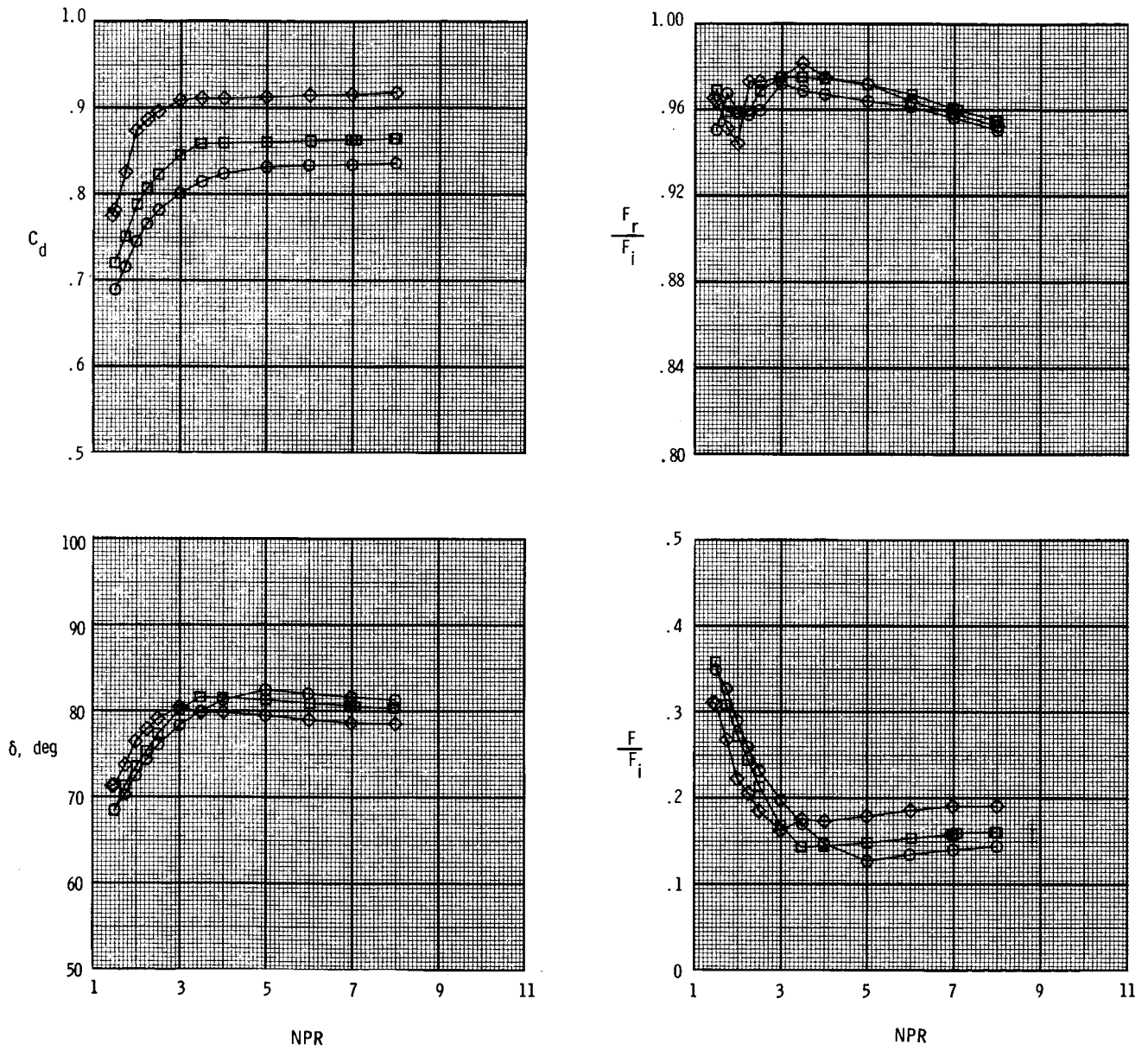
(a) Convergent-section ports.

Figure 17. Effect of port corner radius on resultant thrust-vector angle, discharge coefficient, internal thrust ratio, and resultant thrust ratio for ports with geometric reverser angle of 75° and blocker angle of 75°.

Port corner radius, in.

○   0
□   .109
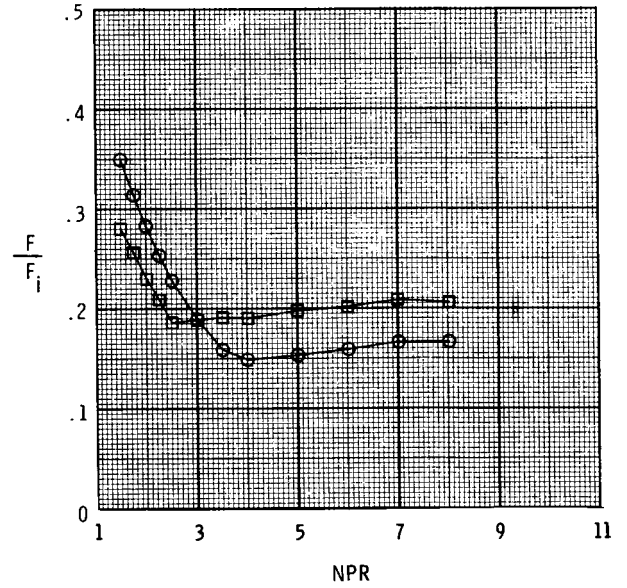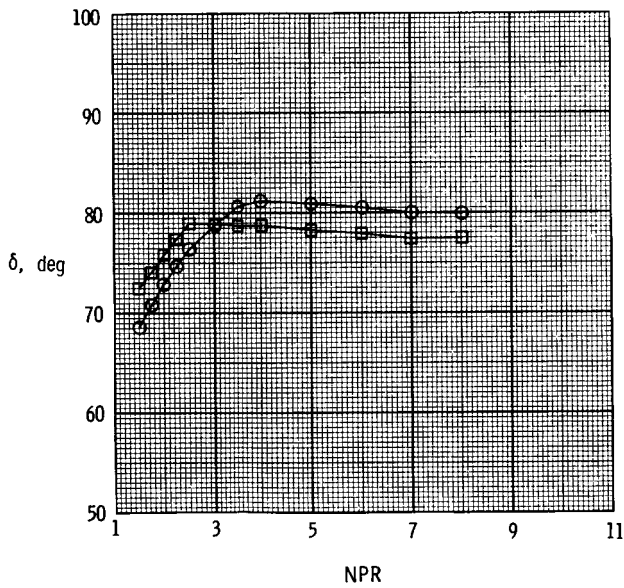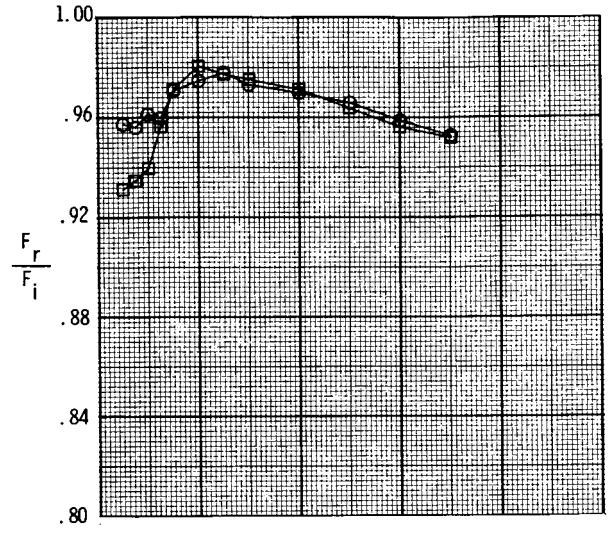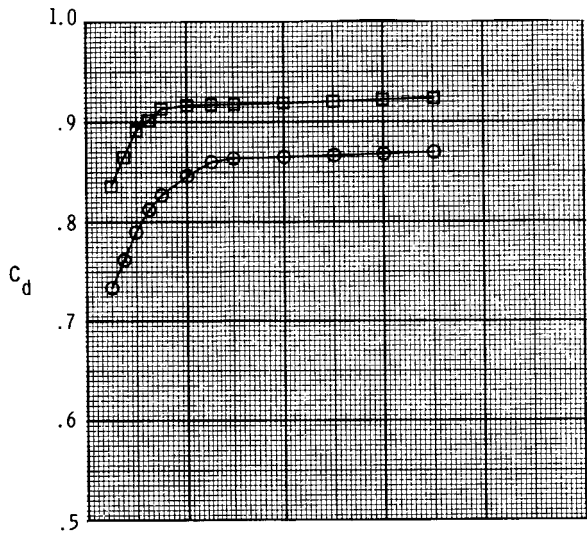
(b) Constant-area duct ports.

Figure 17. Concluded.

Port corner radius, in.

◯   0
▢   .047
◇   .109
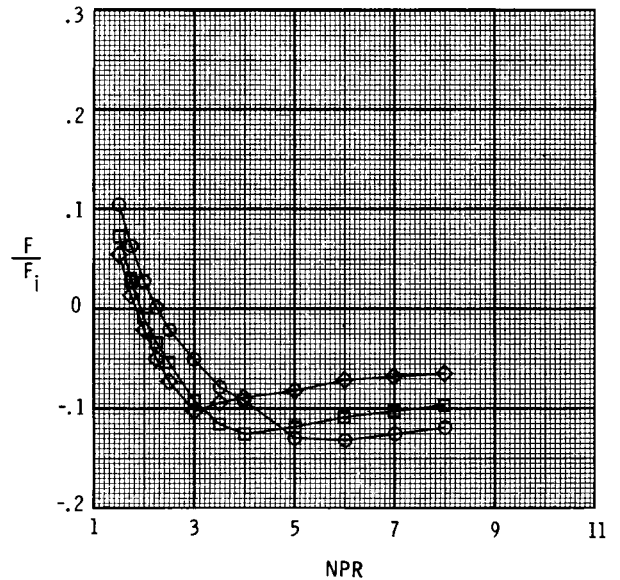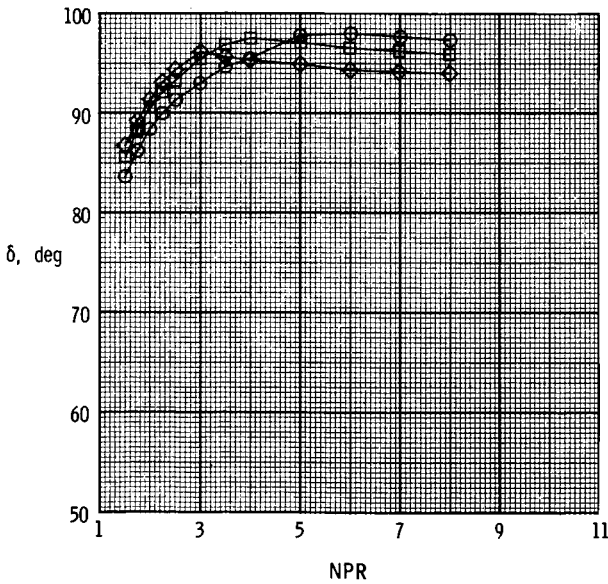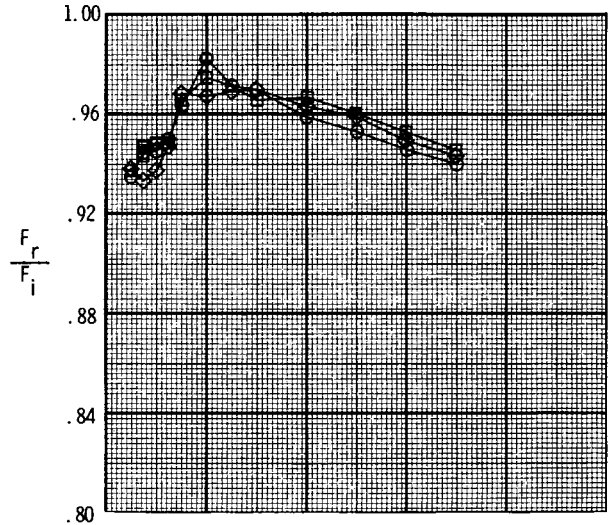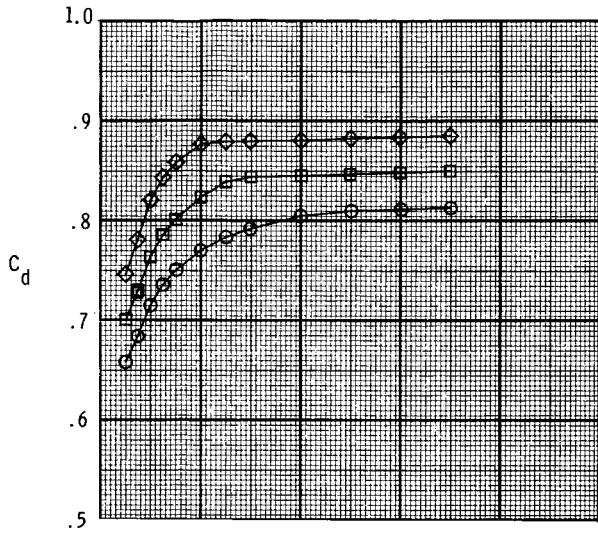
(a) Convergent-section ports.

Figure 18. Effect of port corner radius on resultant thrust-vector angle, discharge coefficient, internal thrust ratio, and resultant thrust ratio for ports with geometric reverser angle of 90° and blocker angle of 90°.
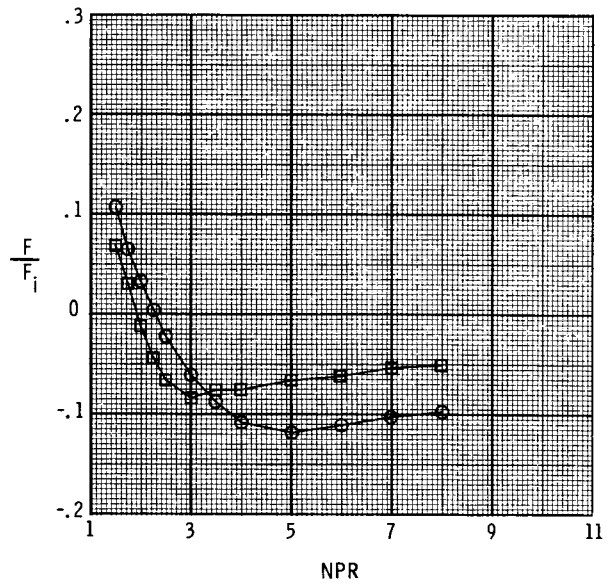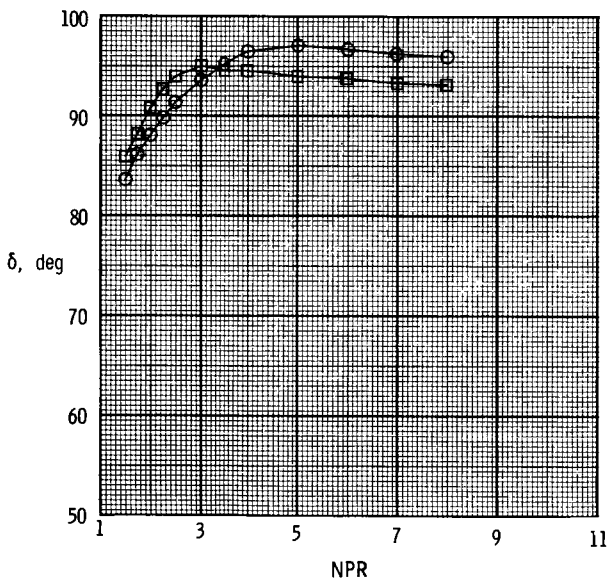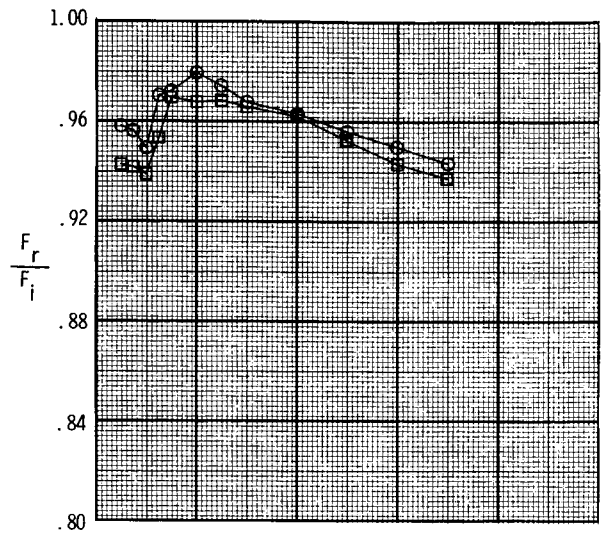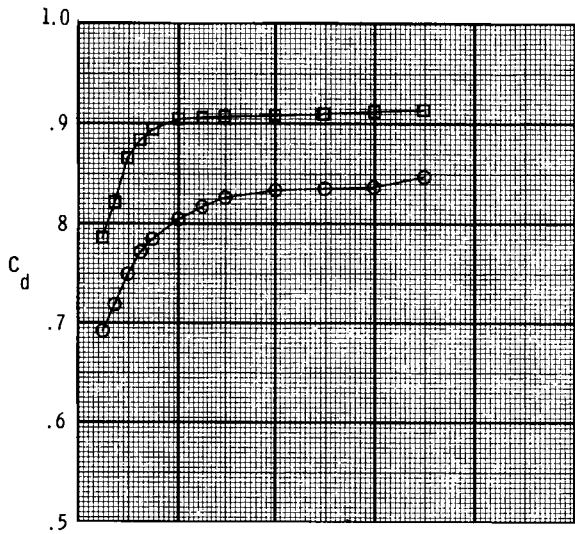
(b) Constant-area duct ports.

Figure 18. Concluded.
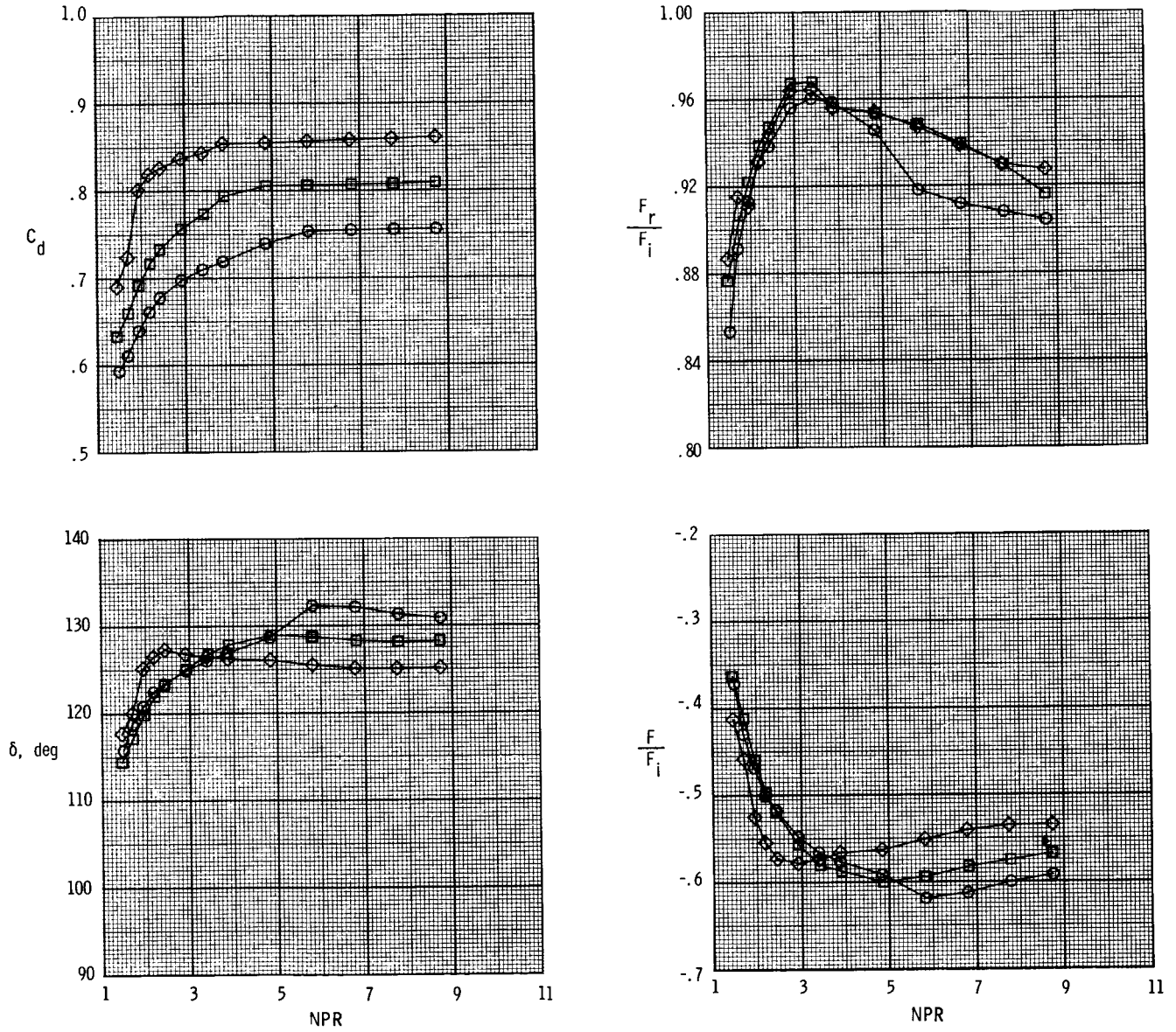
(a) Convergent-section ports.

Figure 19. Effect of port corner radius on resultant thrust-vector angle, discharge coefficient, internal thrust ratio, and resultant thrust ratio for ports with geometric reverser angle of 120° and blocker angle of 120°.
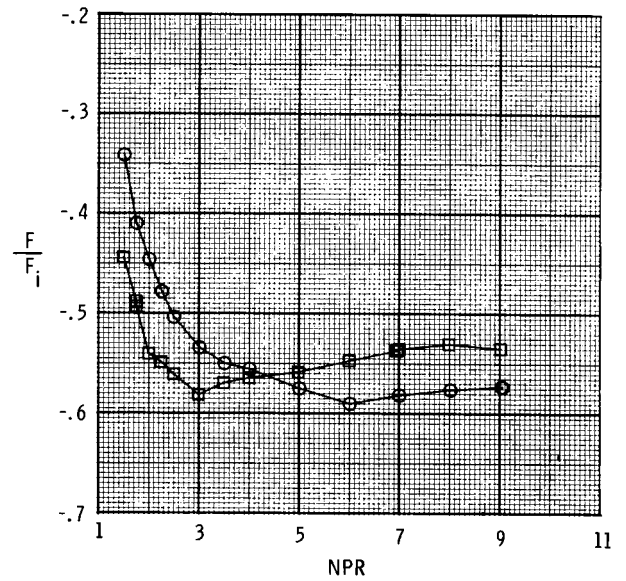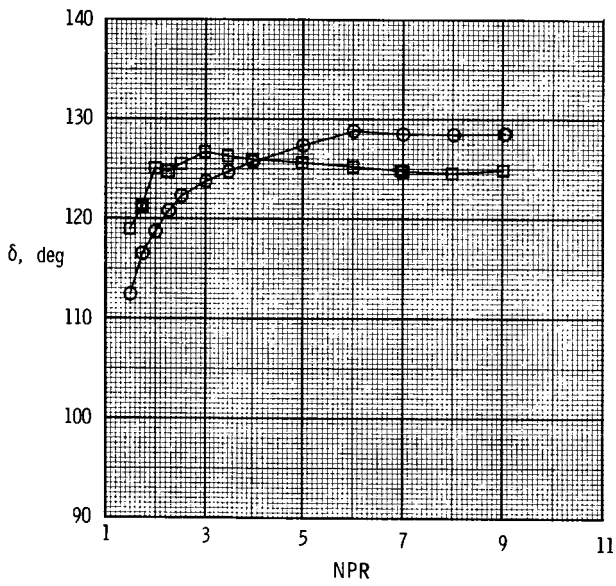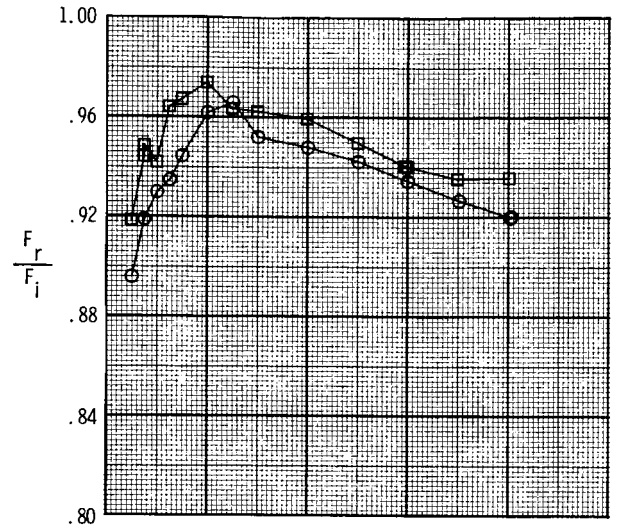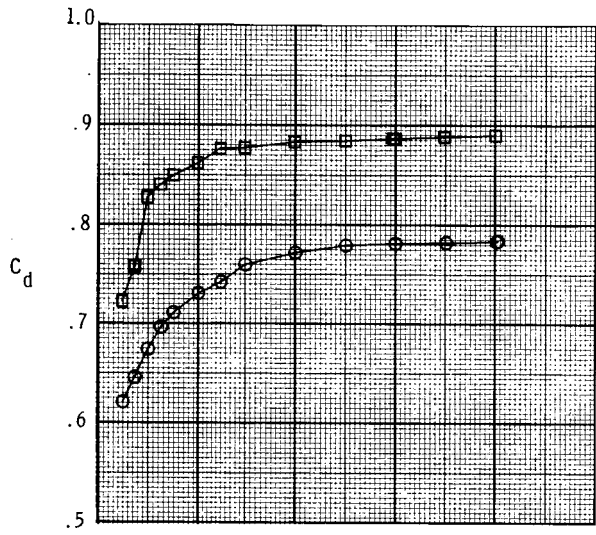
(b) Constant-area duct ports.

Figure 19. Concluded.
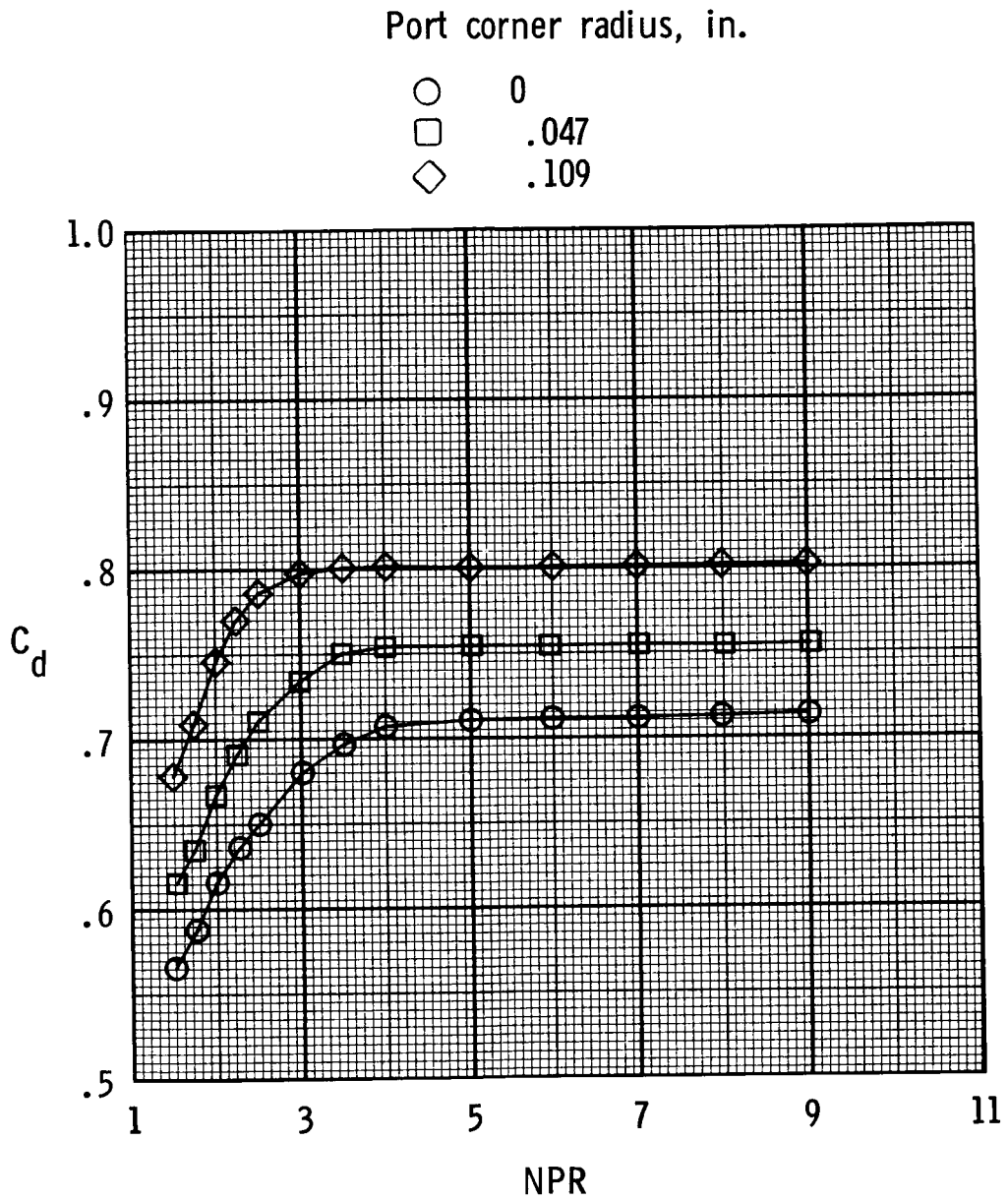
(a) Convergent-section ports.

Figure 20. Effect of port corner radius on discharge coefficient for ports with geometric reverser angle of 135° and blocker angle of 135°.

Port corner radius, in.

○　　0

□　　.109
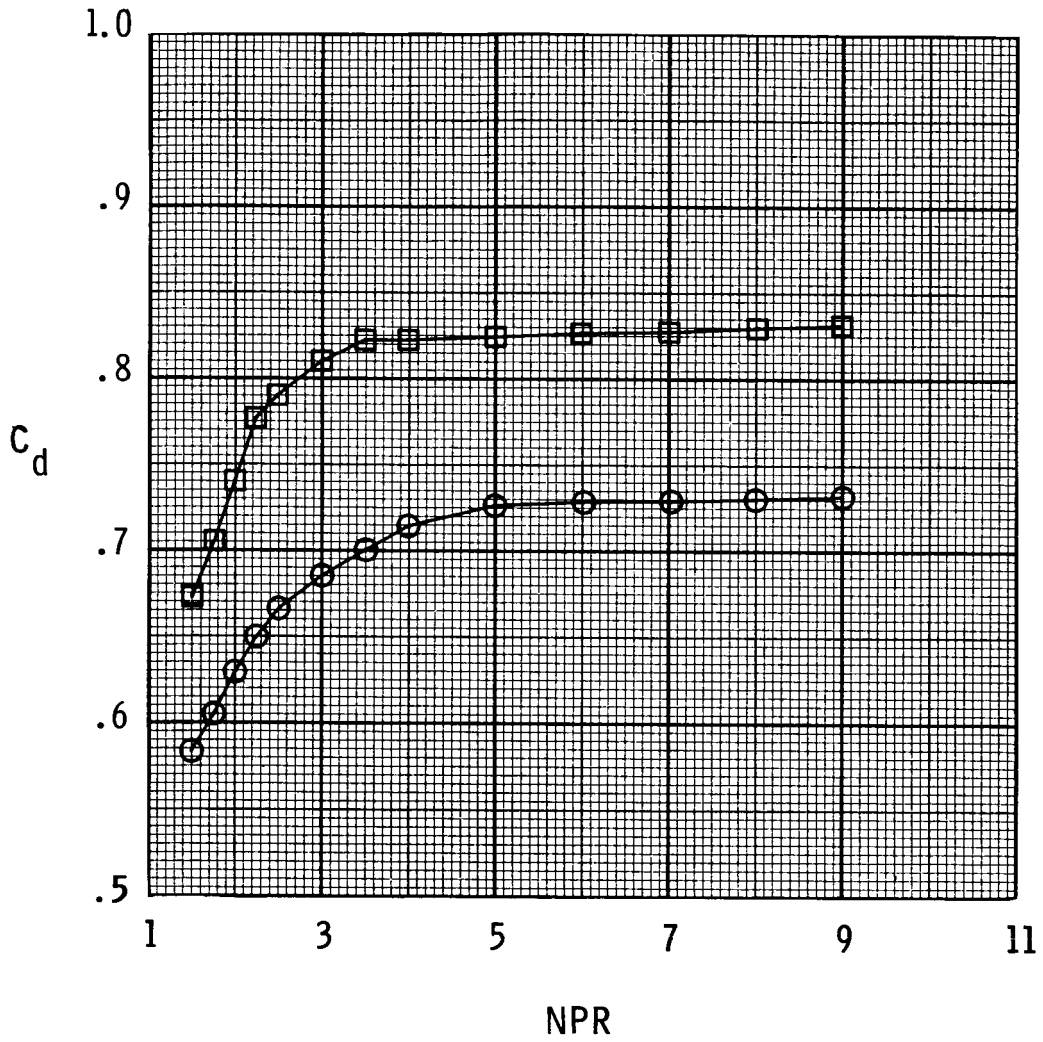
(b) Constant-area duct ports.

Figure 20. Concluded.
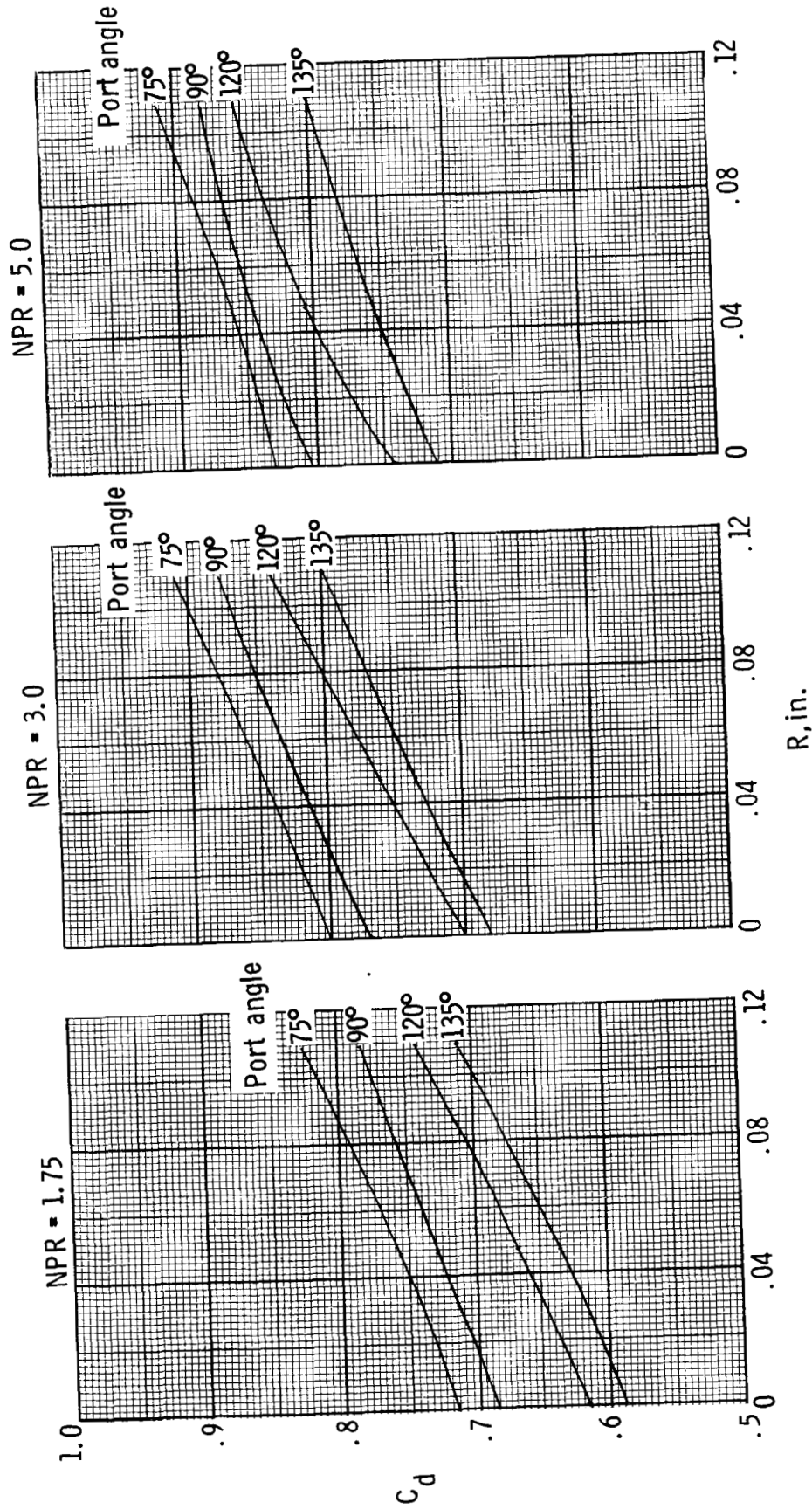
Figure 21. Variation of discharge coefficient with port corner radius at three nozzle pressure ratios for ports in convergent section of nozzle.

71
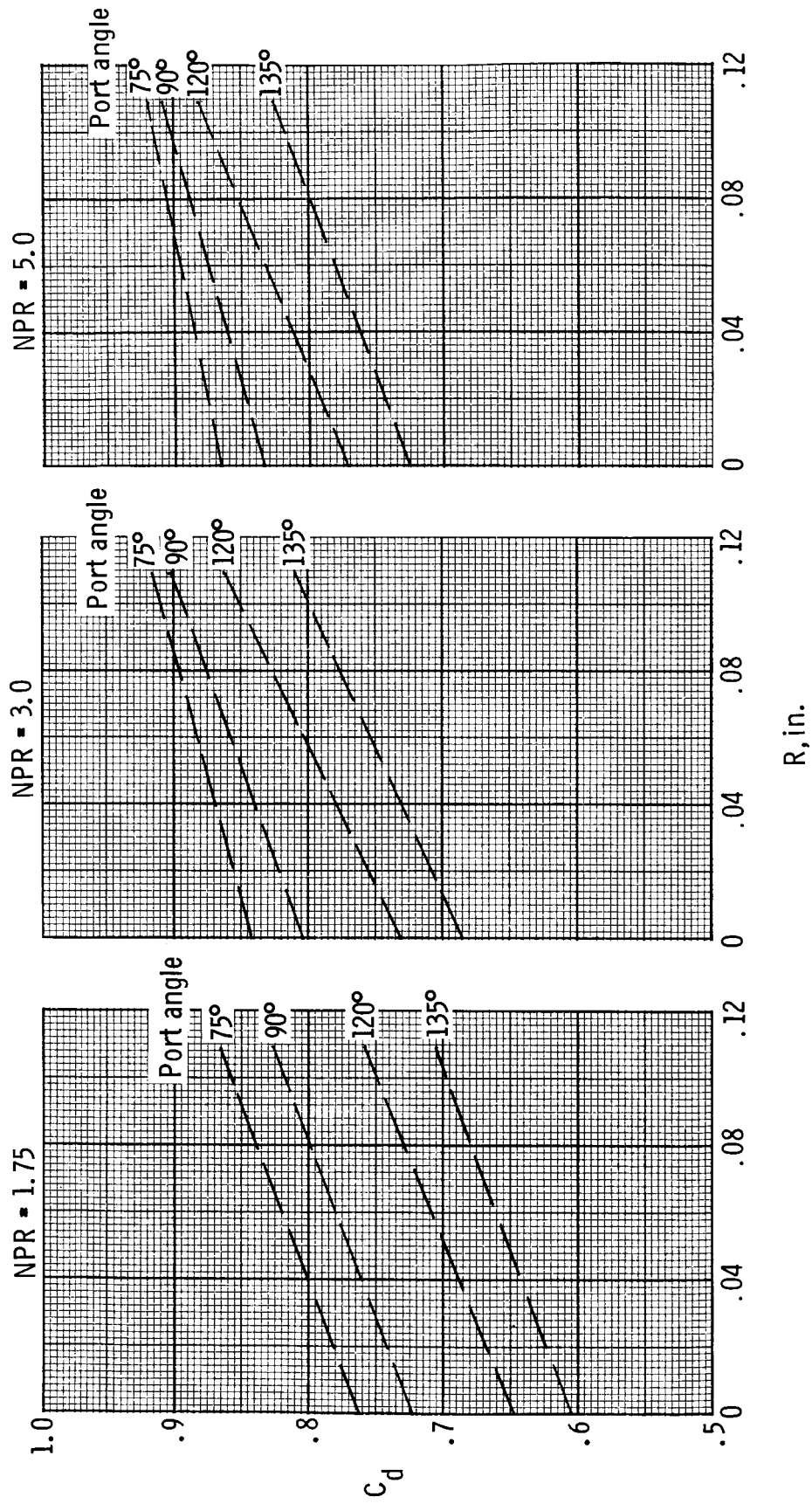
Figure 22. Variation of discharge coefficient with port corner radius at three nozzle pressure ratios for ports in constant-area duct.
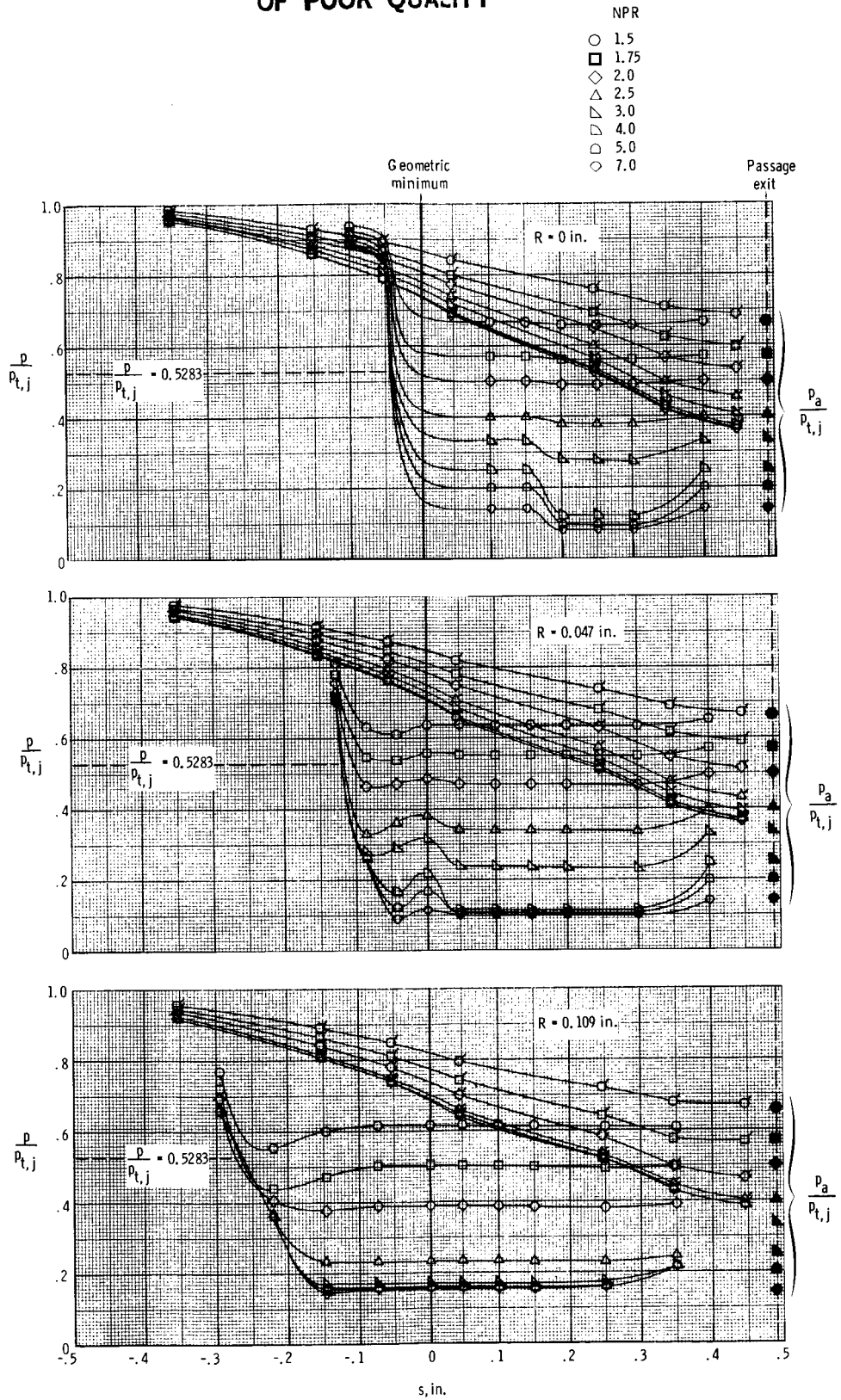
Figure 23. Pressure distributions on forward and aft flow surfaces for 135° ports with sharp and rounded port corners in convergent section of nozzle. Flagged symbols indicate aft surface pressures.
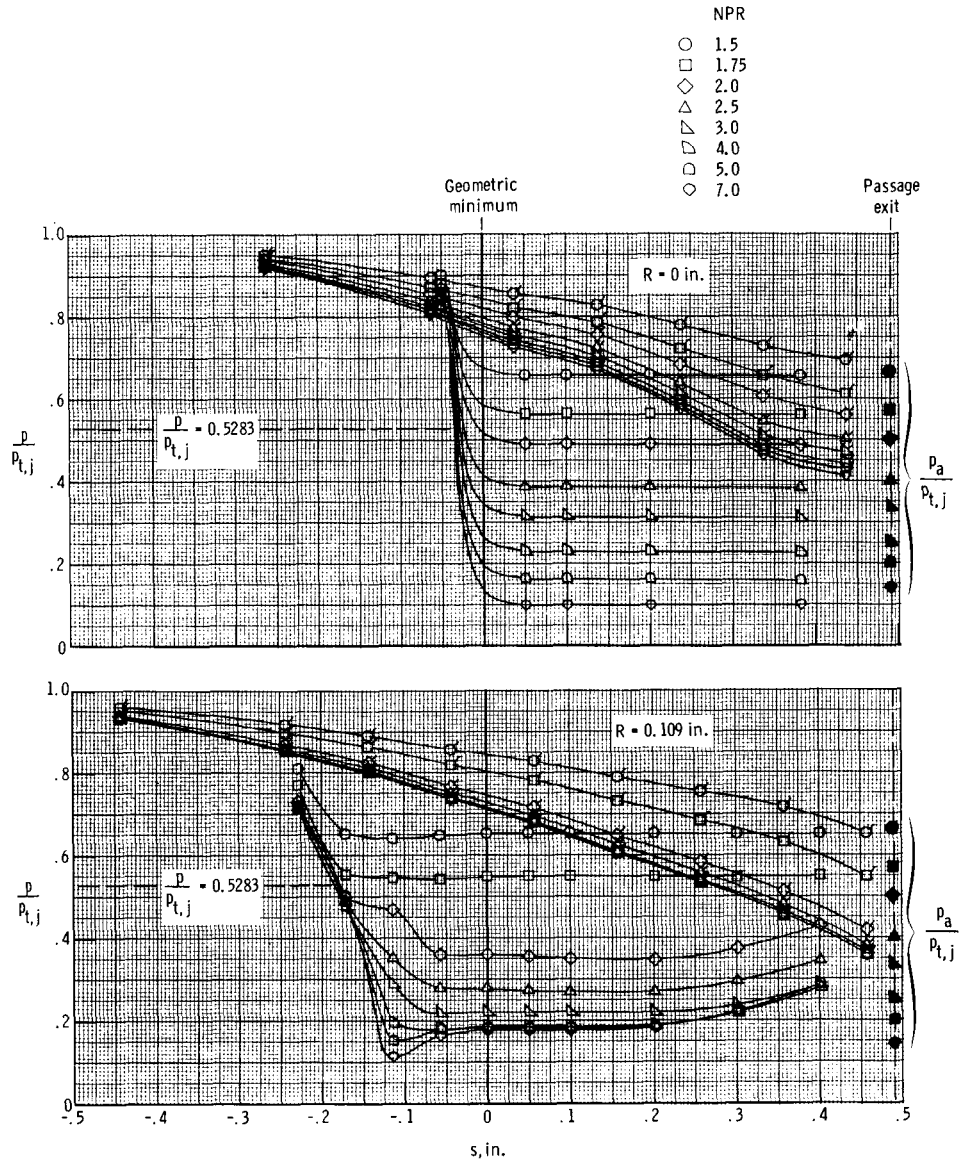
Figure 24. Pressure distributions on forward and aft flow surfaces for 120° ports with sharp and rounded port corners in constant-area duct. Flagged symbols indicate aft surface pressures.
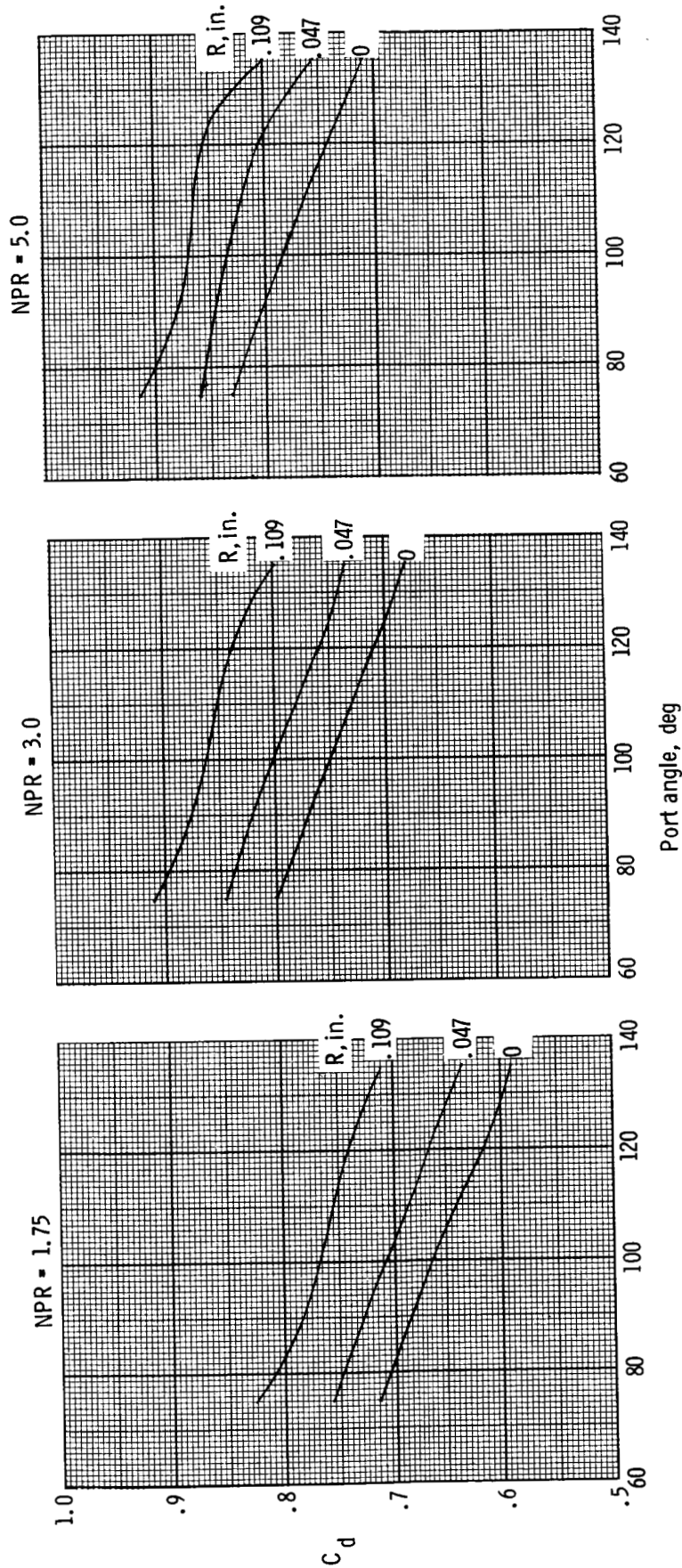
Figure 25. Variation of discharge coefficient with port angle at three nozzle pressure ratios for basic ports in convergent section of nozzle.
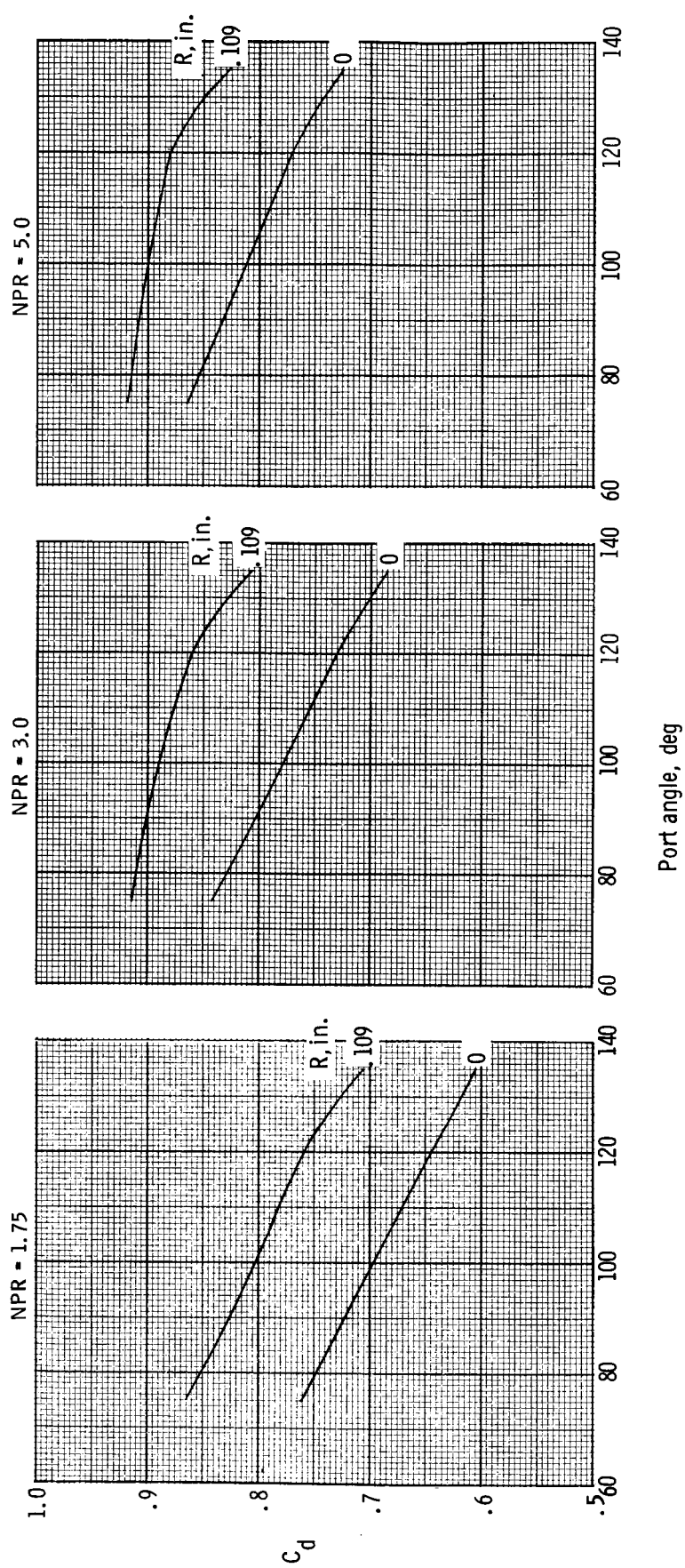
Figure 26. Variation of discharge coefficient with port angle at three nozzle pressure ratios for basic ports in constant-area duct.
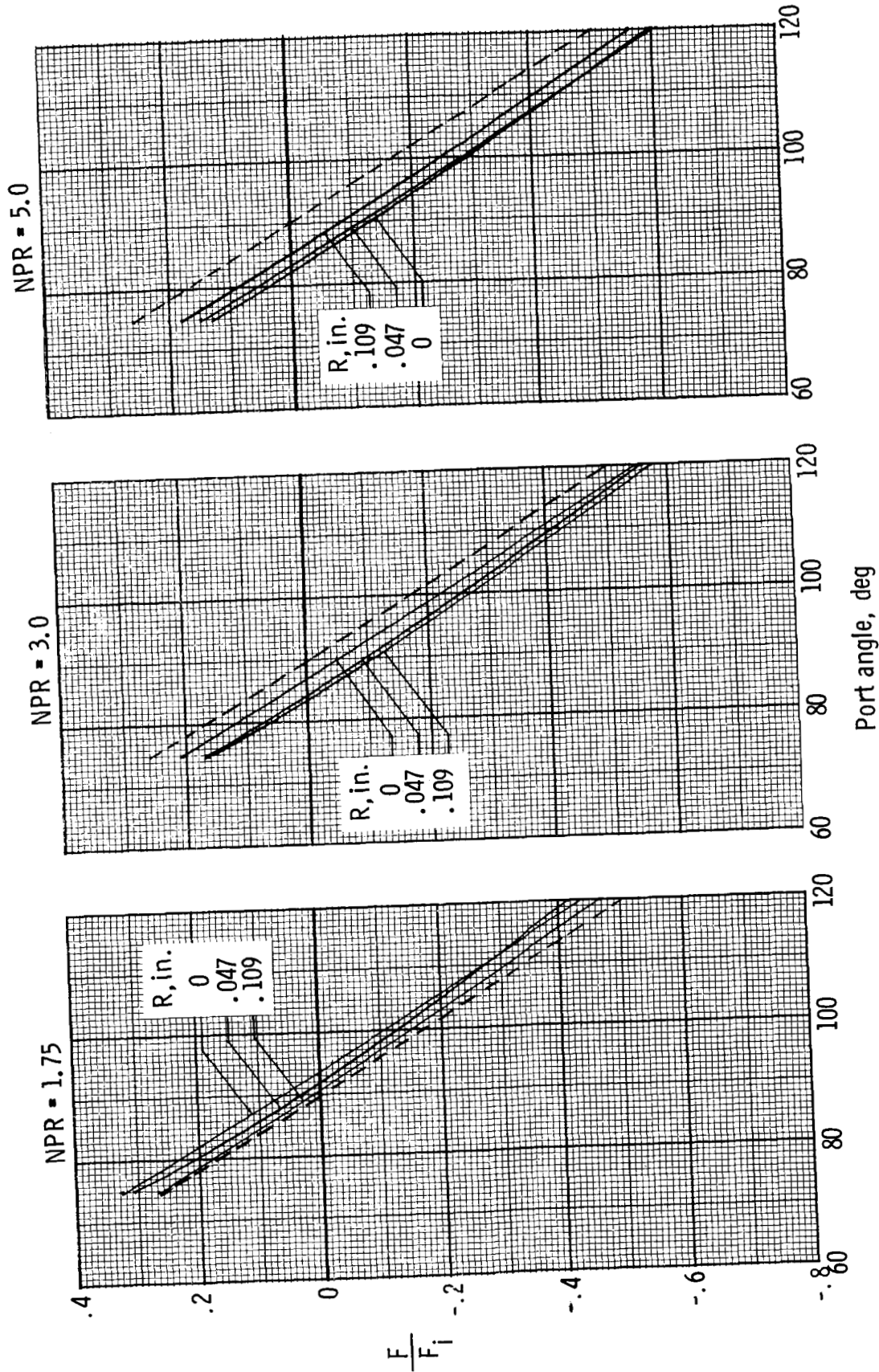
Figure 27. Variation of internal thrust ratio with port angle at three nozzle pressure ratios for basic ports in convergent section of nozzle. Dashed lines indicate cosine of port angle.

77
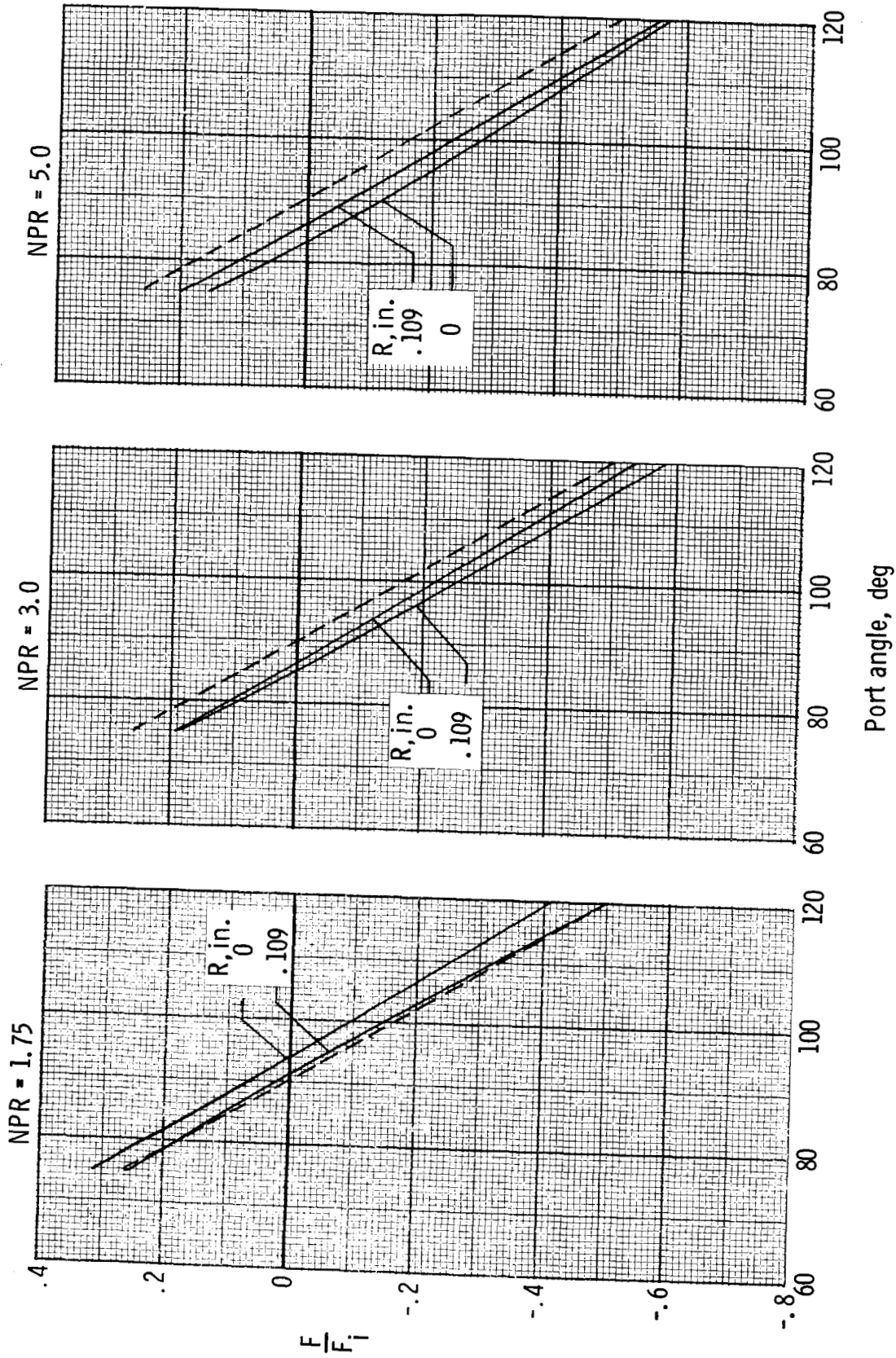
Figure 28. Variation of internal thrust ratio with port angle at three nozzle pressure ratios for basic ports in constant-area duct. Dashed lines indicate cosine of port angle.
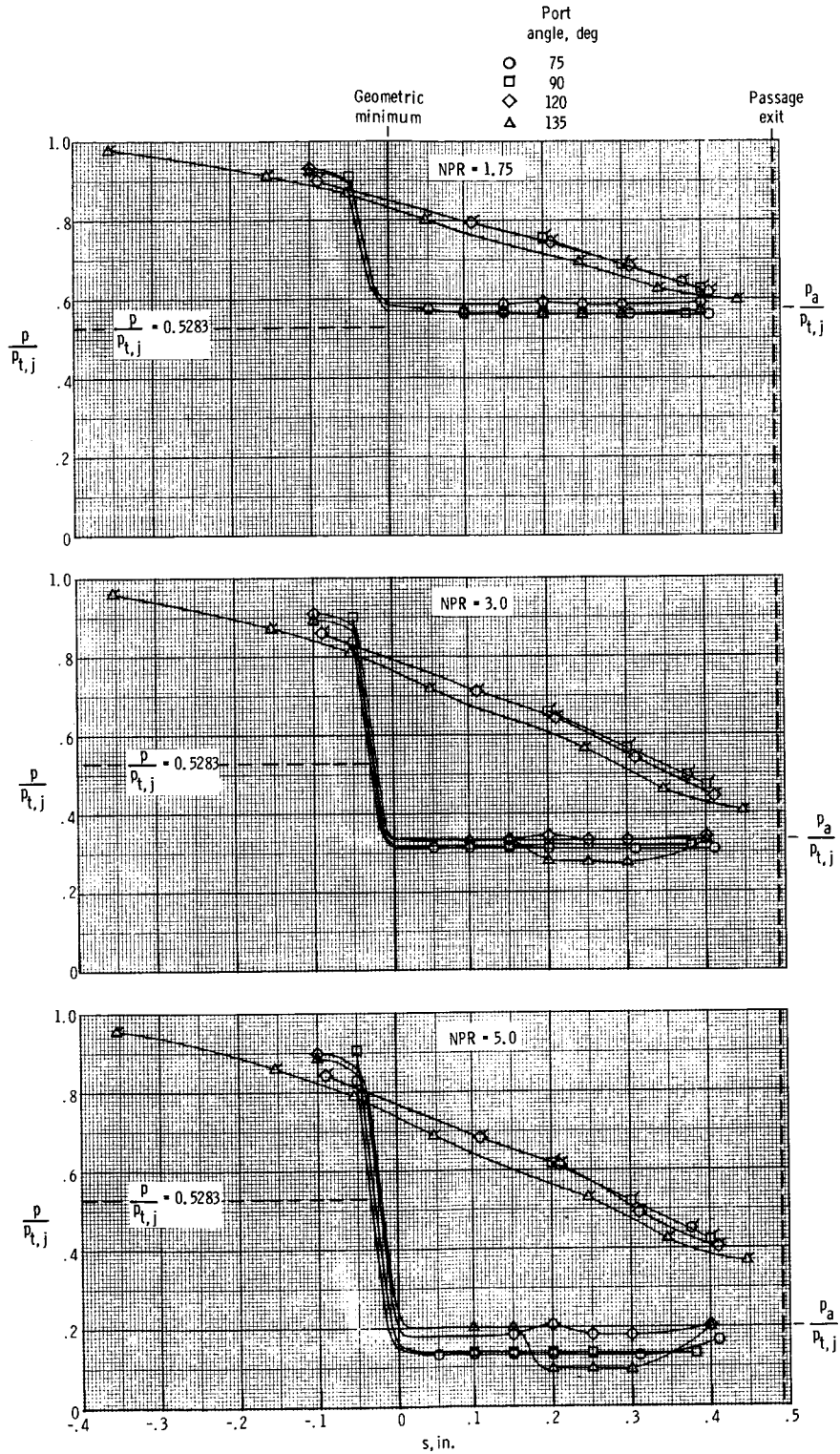
Figure 29. Pressure distributions (at three nozzle pressure ratios) on forward and aft flow surfaces for ports with corner radius of 0 in. in convergent section of nozzle. Flagged symbols indicate aft surface pressures.
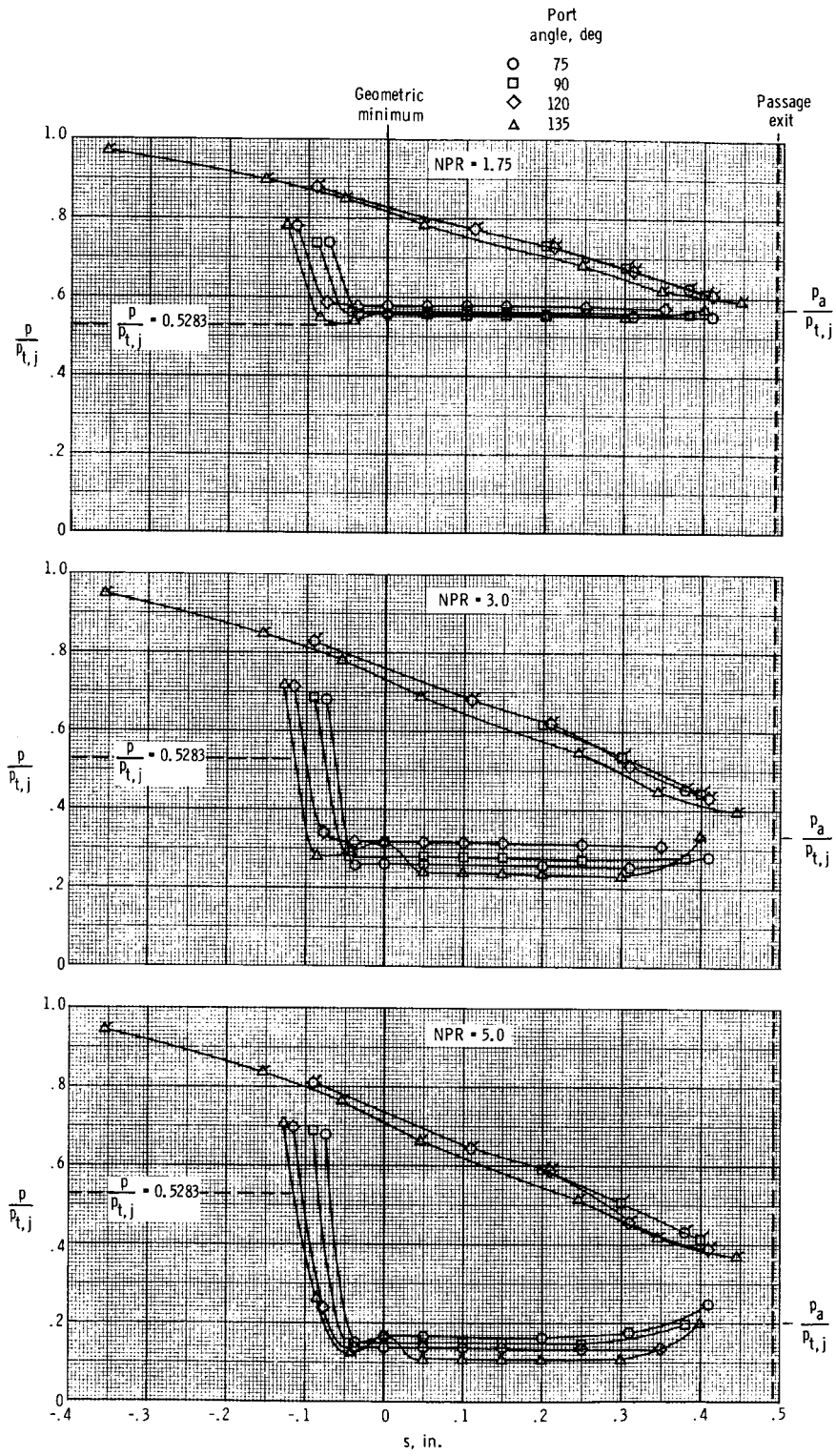
Figure 30. Pressure distributions (at three nozzle pressure ratios) on forward and aft flow surfaces for ports with corner radius of 0.047 in. in convergent section of nozzle. Flagged symbols indicate aft surface pressures.
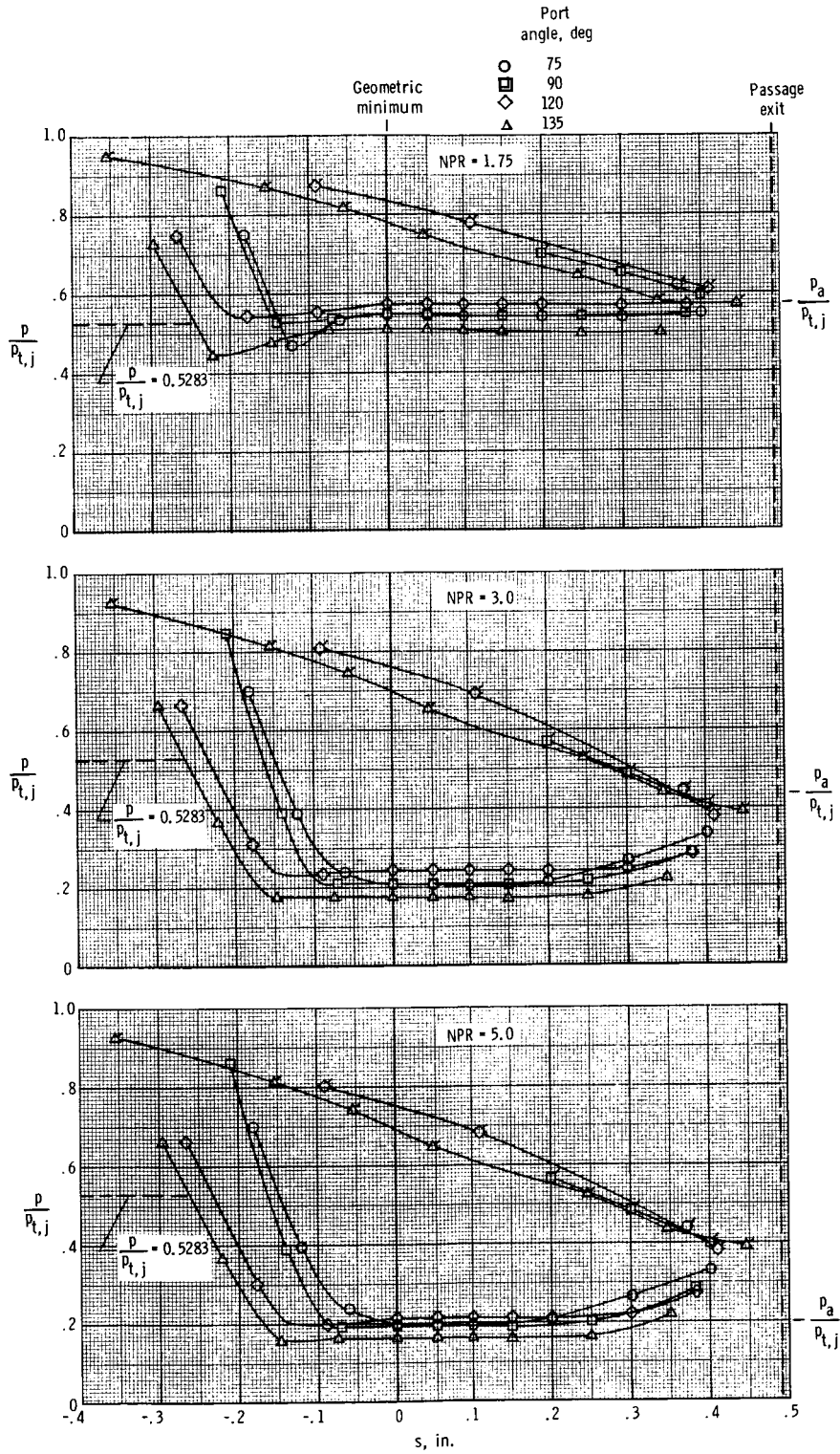
Figure 31. Pressure distributions (at three nozzle pressure ratios) on forward and aft flow surfaces for ports with corner radius of 0.109 in. in convergent section of nozzle. Flagged symbols indicate aft surface pressures.
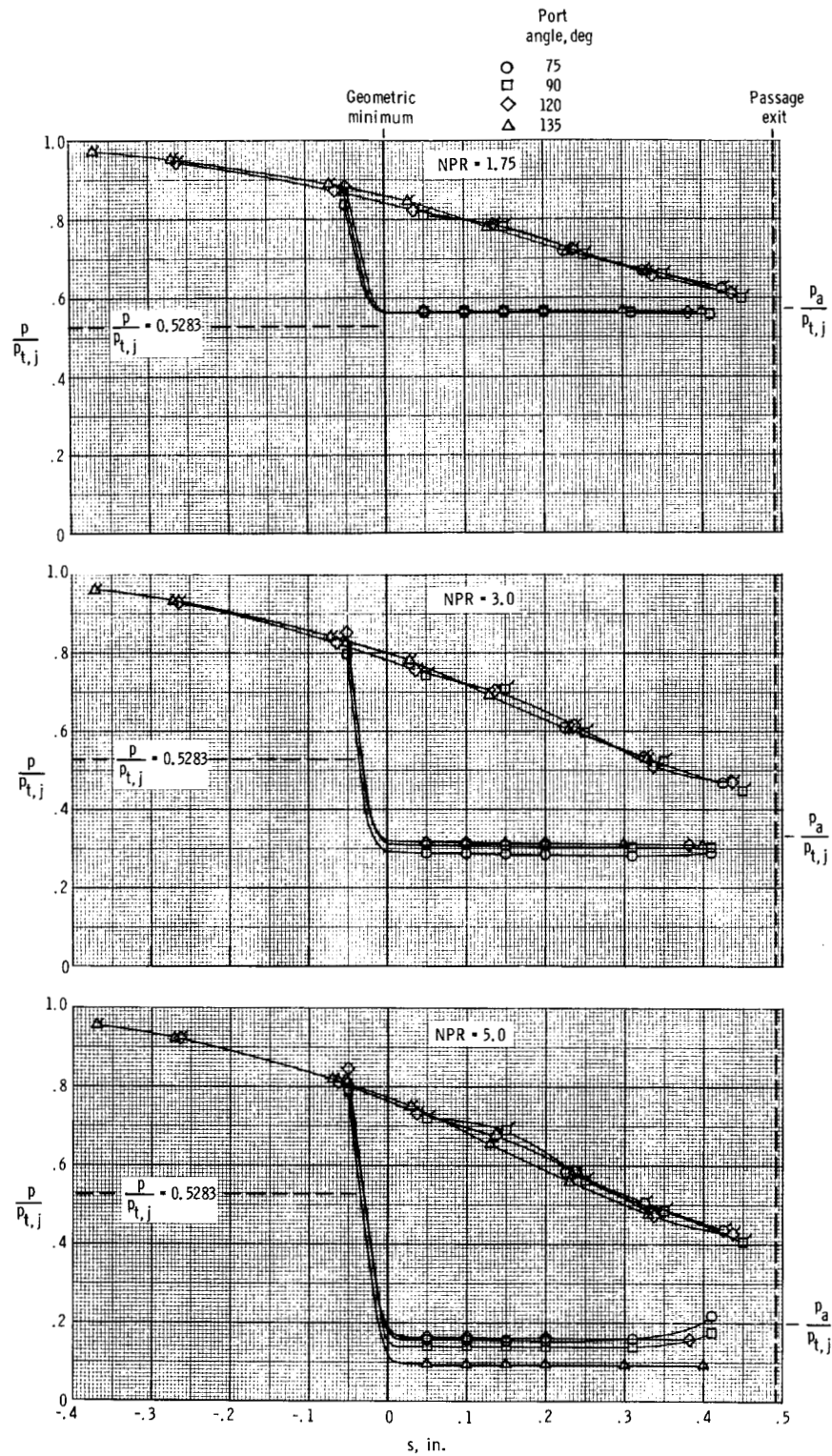
Figure 32. Pressure distributions (at three nozzle pressure ratios) on forward and aft flow surfaces for ports with corner radius of 0 in. in constant-area duct. Flagged symbols indicate aft surface pressures.
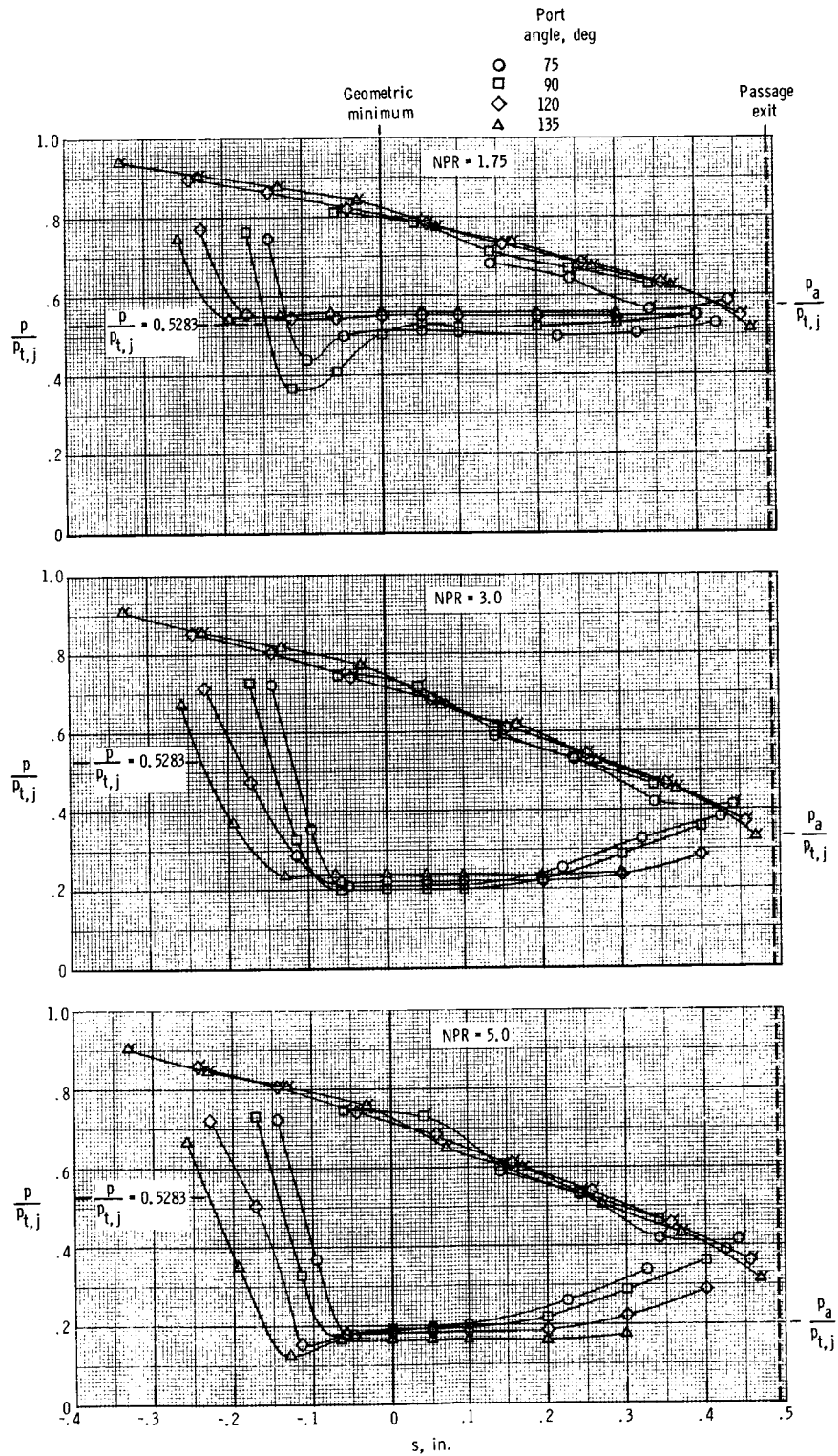
Figure 33. Pressure distributions (at three nozzle pressure ratios) on forward and aft flow surfaces for ports with corner radius of 0.109 in. in constant-area duct. Flagged symbols indicate aft surface pressures.

83
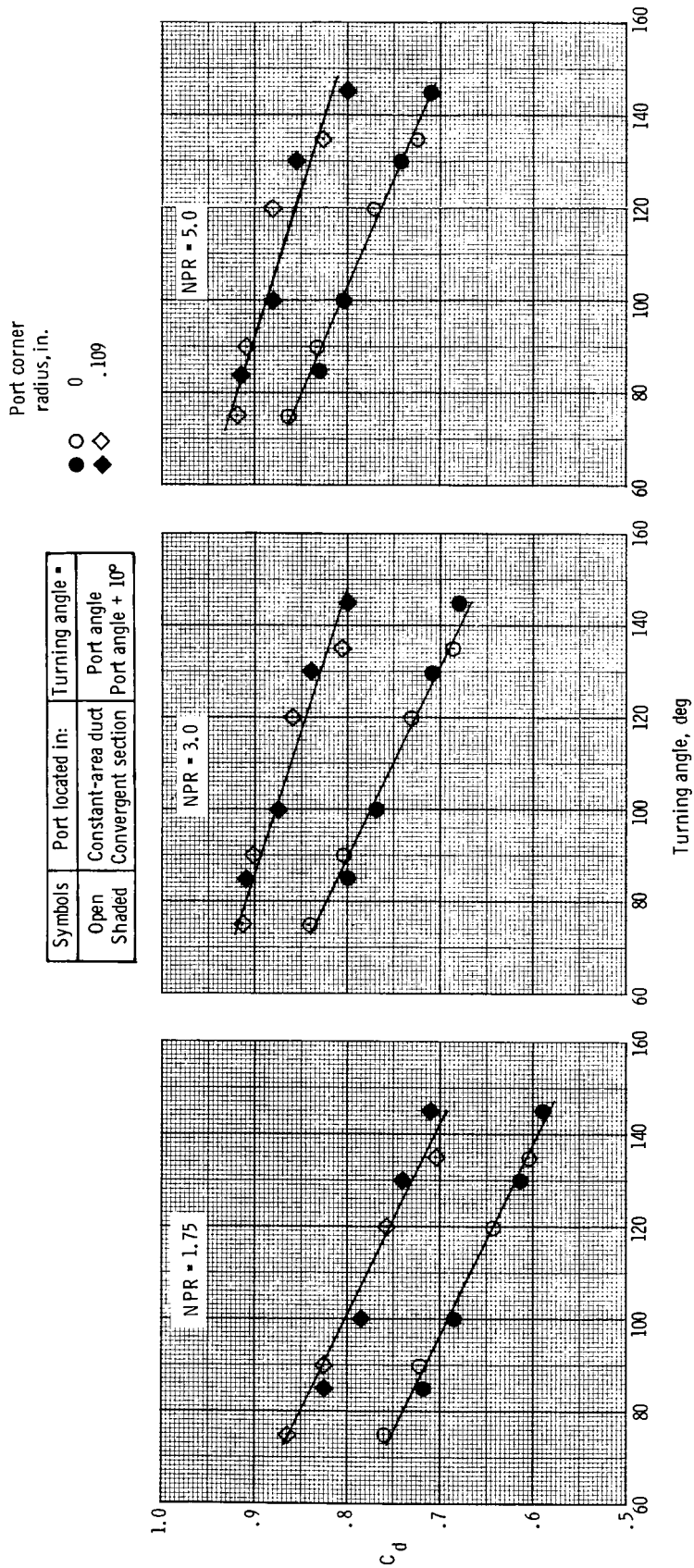
Figure 34. Correlation of discharge coefficient data with flow-turning angle for three nozzle pressure ratios.

Blocker angle, deg

○   90
□   120
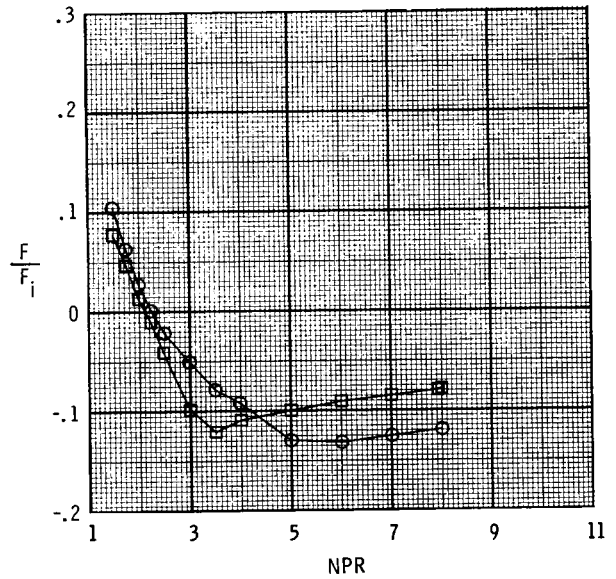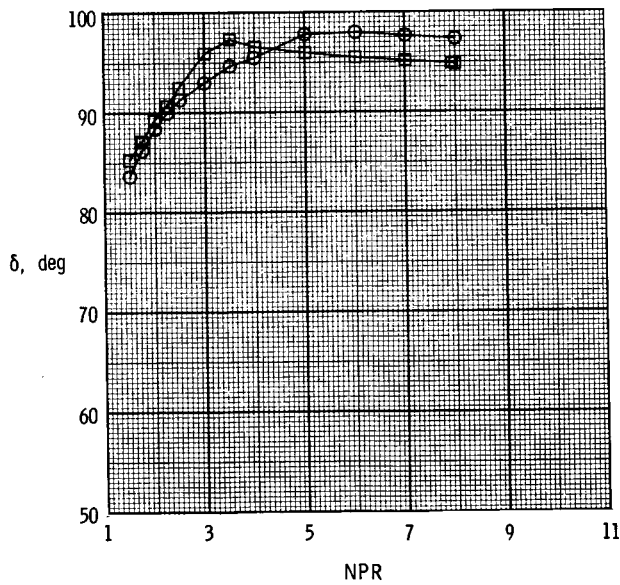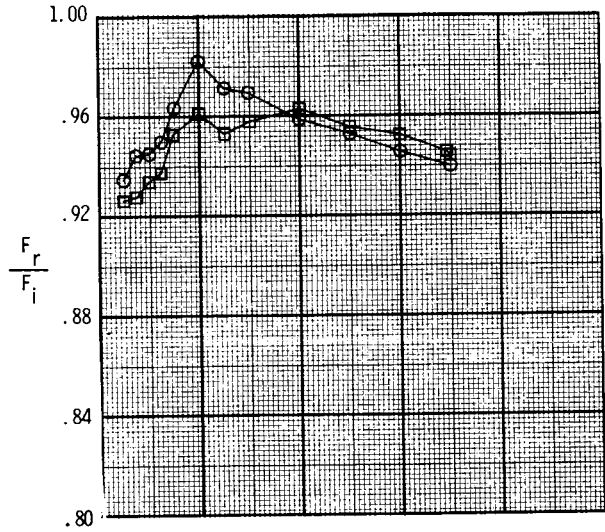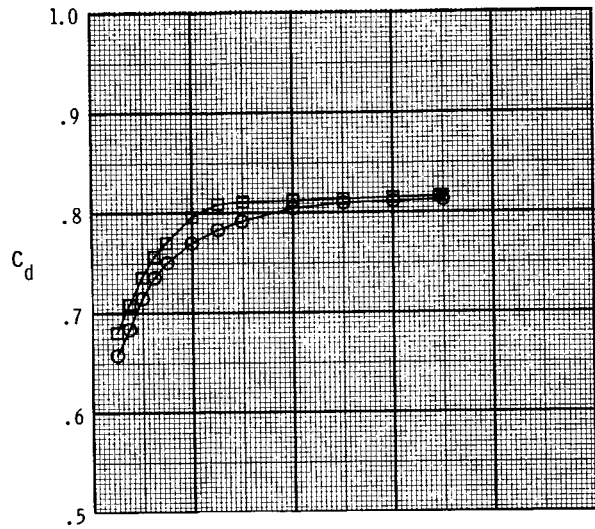
(a) Port corner radius of 0.

Figure 35. Effect of blocker angle on resultant thrust-vector angle, discharge coefficient, internal thrust ratio, and resultant thrust ratio for ports with geometric reverser angle of 90° with convergent-section geometry.

Blocker angle, deg

○   90
□   120
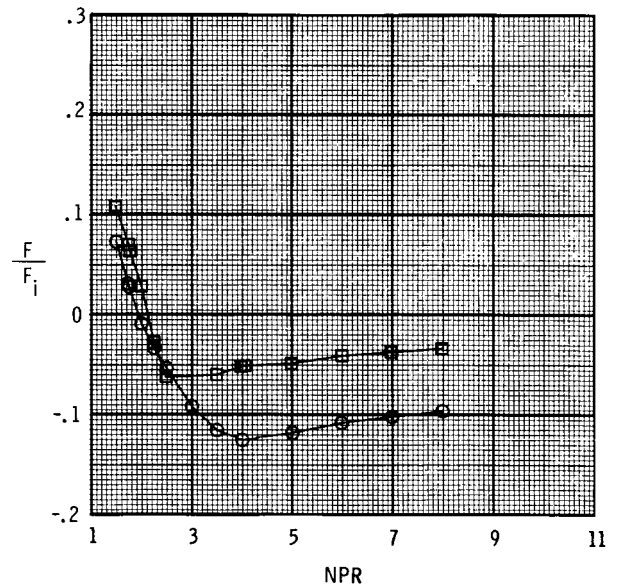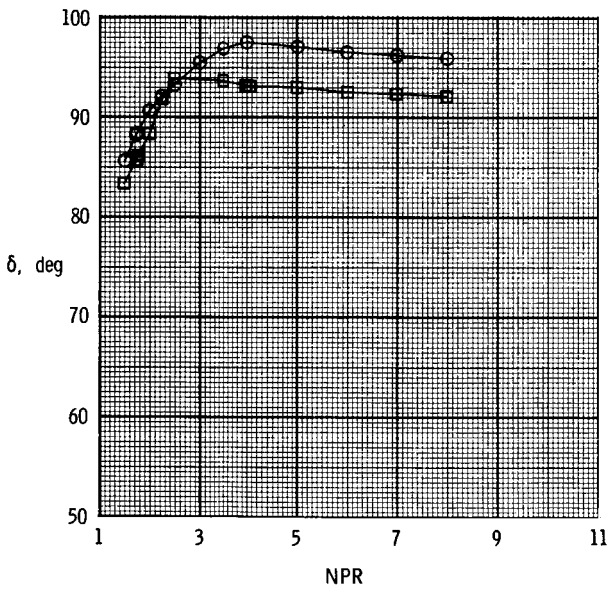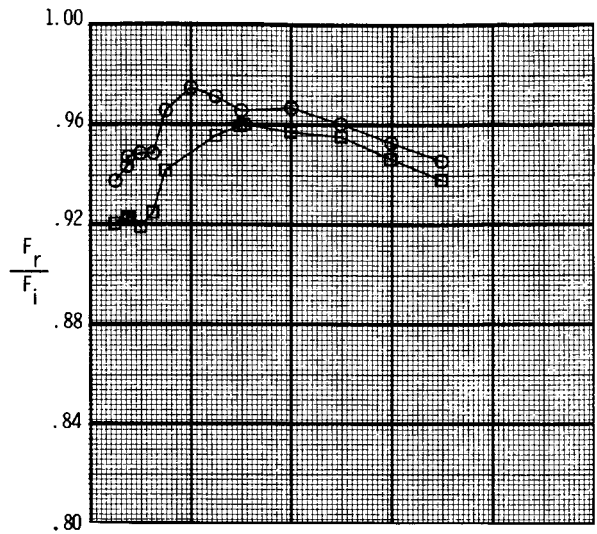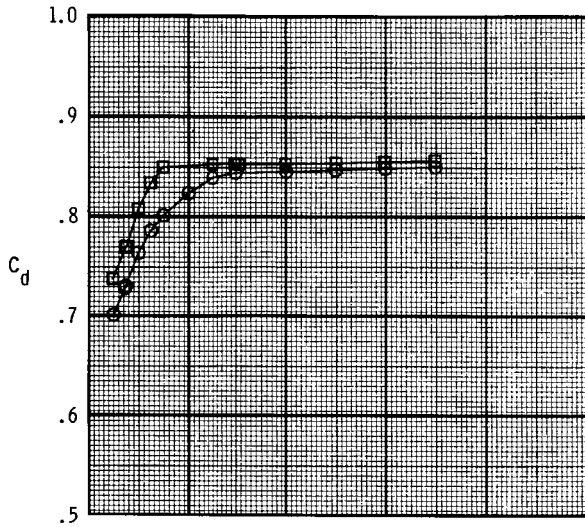
(b) Port corner radius of 0.047 in.

Figure 35. Concluded.

Blocker angle, deg

○ 75
□ 90
◇ 120
△ 135/90
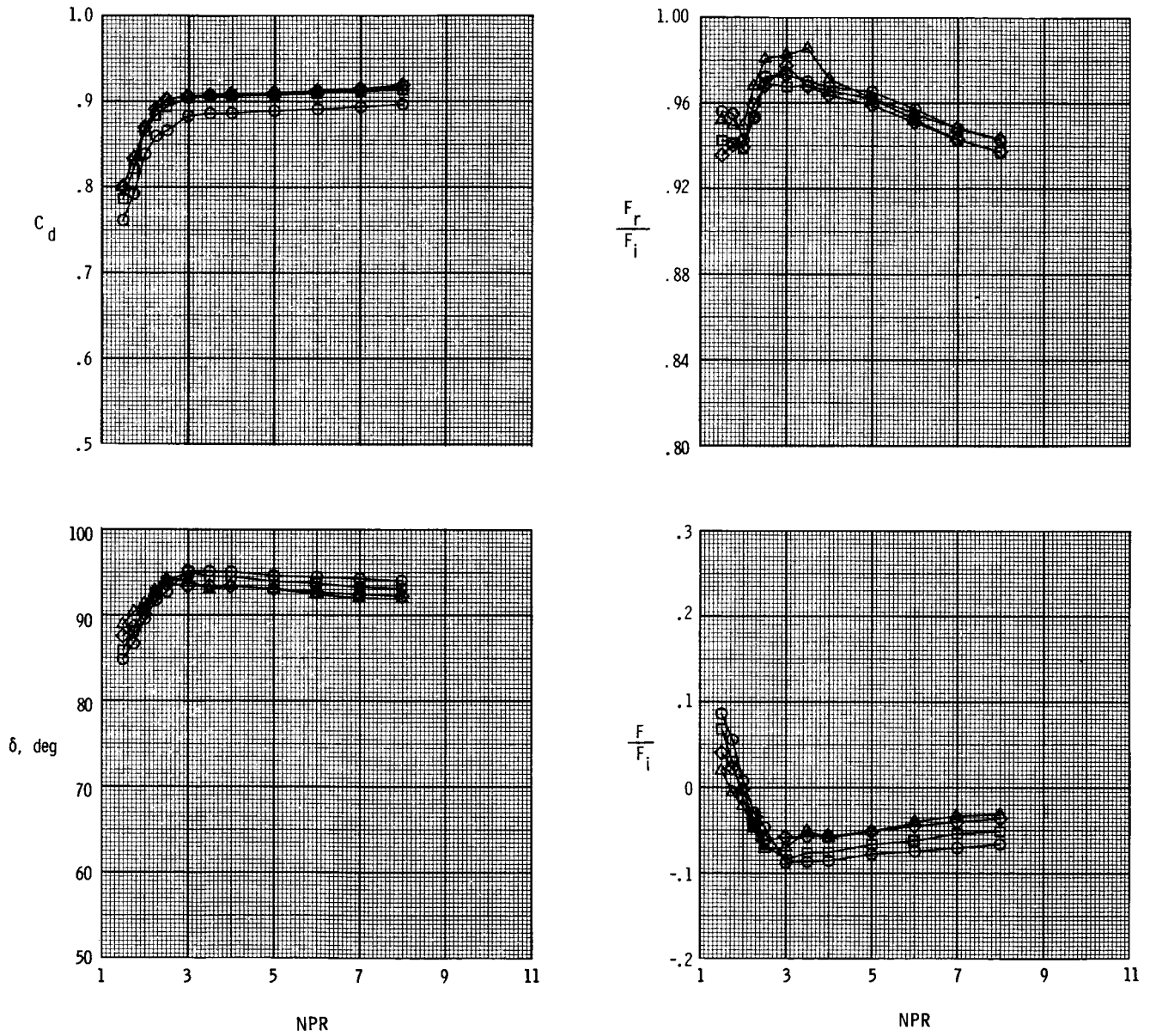
Figure 36. Effect of blocker angle on resultant thrust-vector angle, discharge coefficient, internal thrust ratio, and resultant thrust ratio for ports with geometric reverser angle of 90° with constant-area duct geometry and port corner radius of 0.109 in.
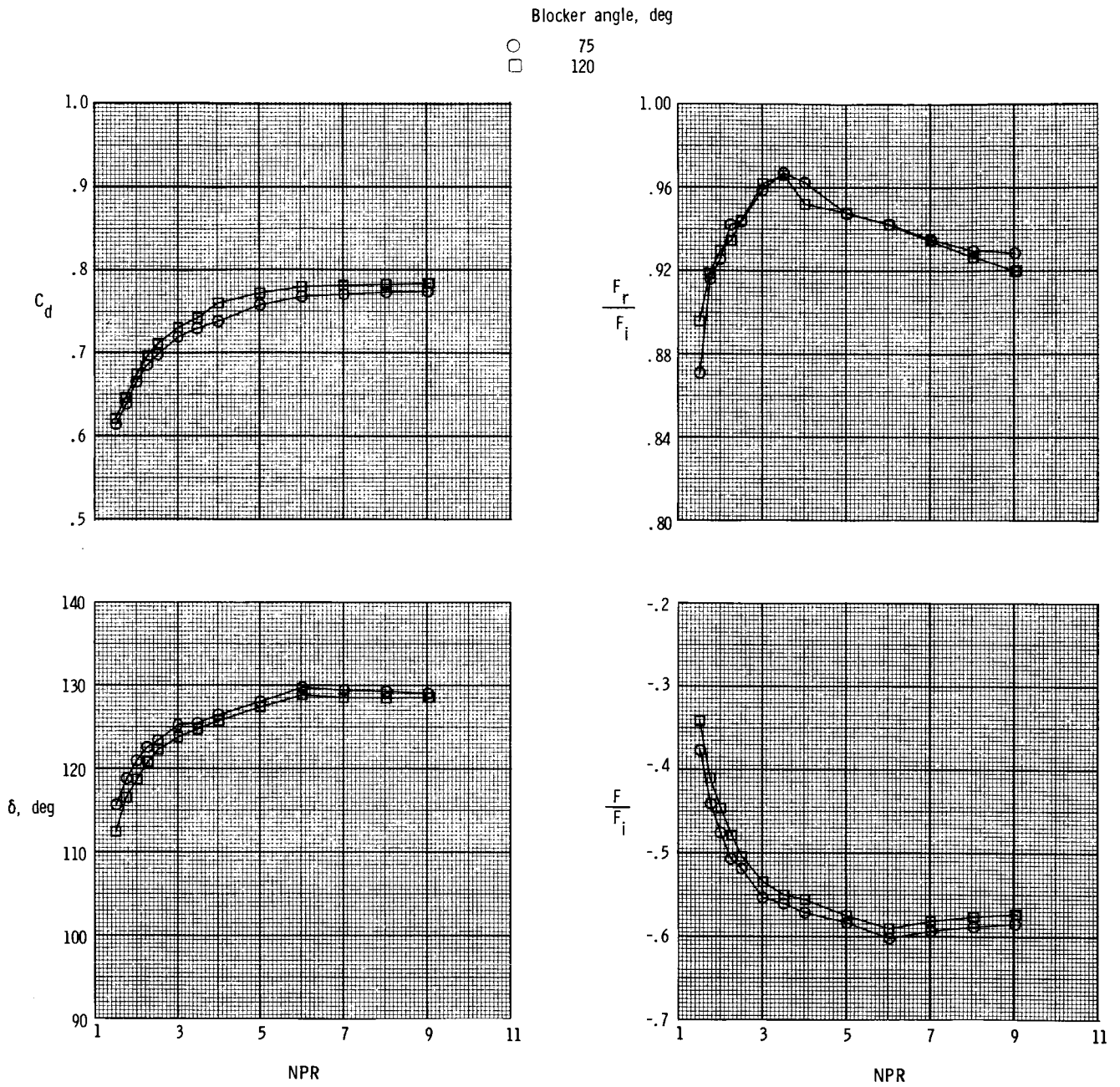
Figure 37. Effect of blocker angle on resultant thrust-vector angle, discharge coefficient, internal thrust ratio, and resultant thrust ratio for ports with geometric reverser angle of 120° with constant-area duct geometry and port corner radius of 0 in.

Blocker angle, deg

○	90
▢	120
◇	135
△	135/90
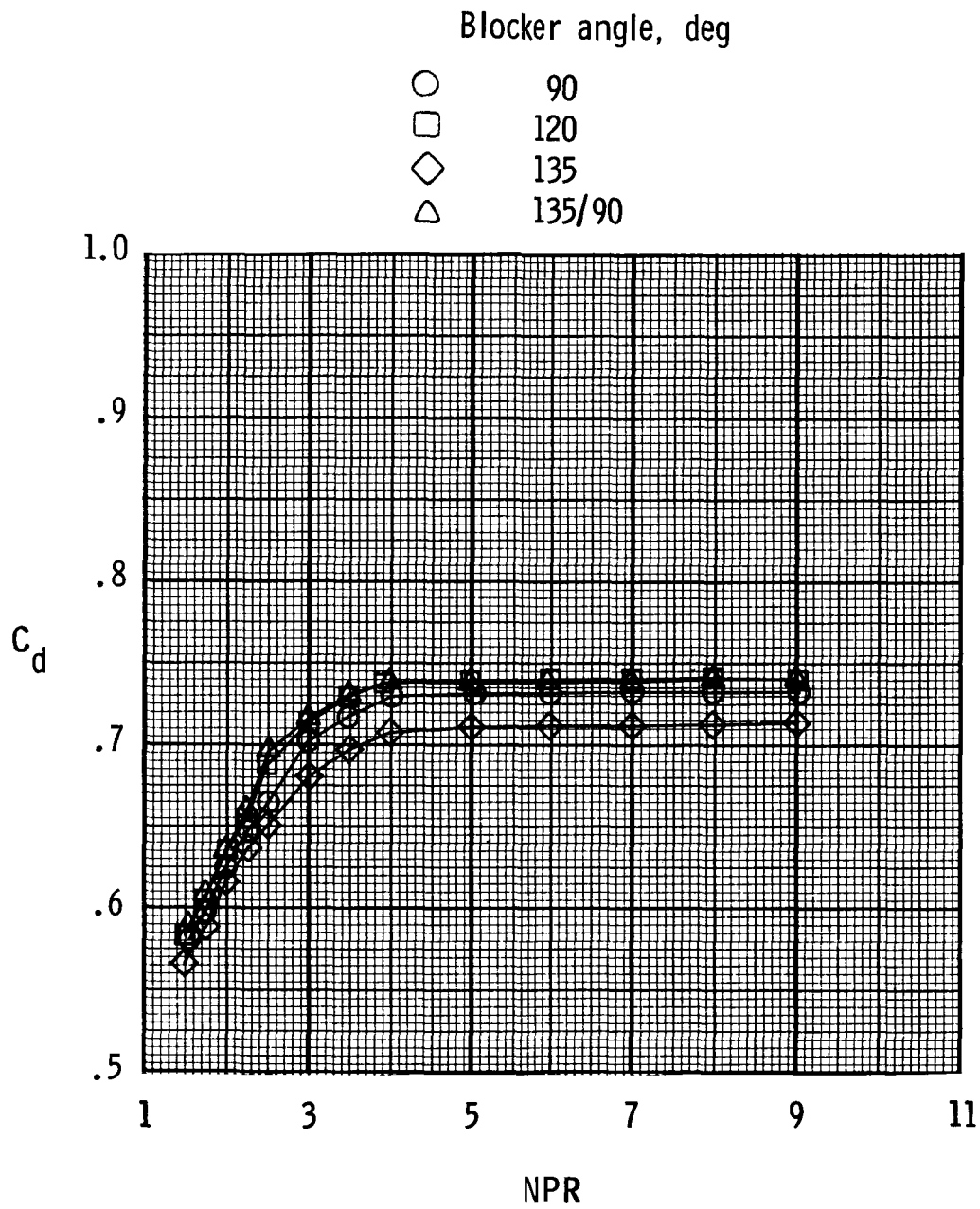
Figure 38. Effect of blocker angle on discharge coefficient for ports with geometric reverser angle of 135° with convergent-section geometry and port corner radius of 0 in.
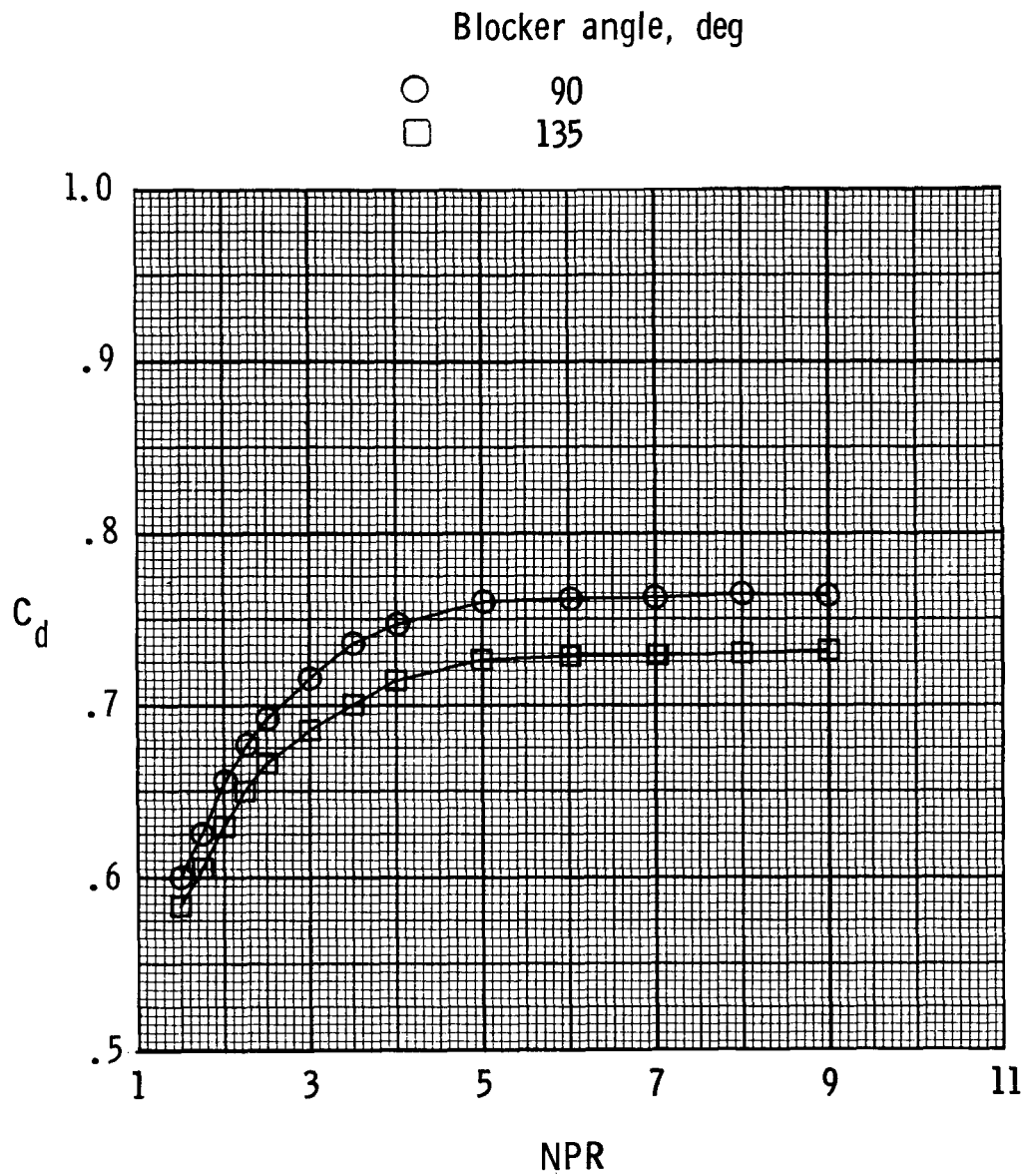
Figure 39. Effect of blocker angle on discharge coefficient for ports with geometric reverser angle of 135° with constant-area duct geometry and port corner radius of 0 in.
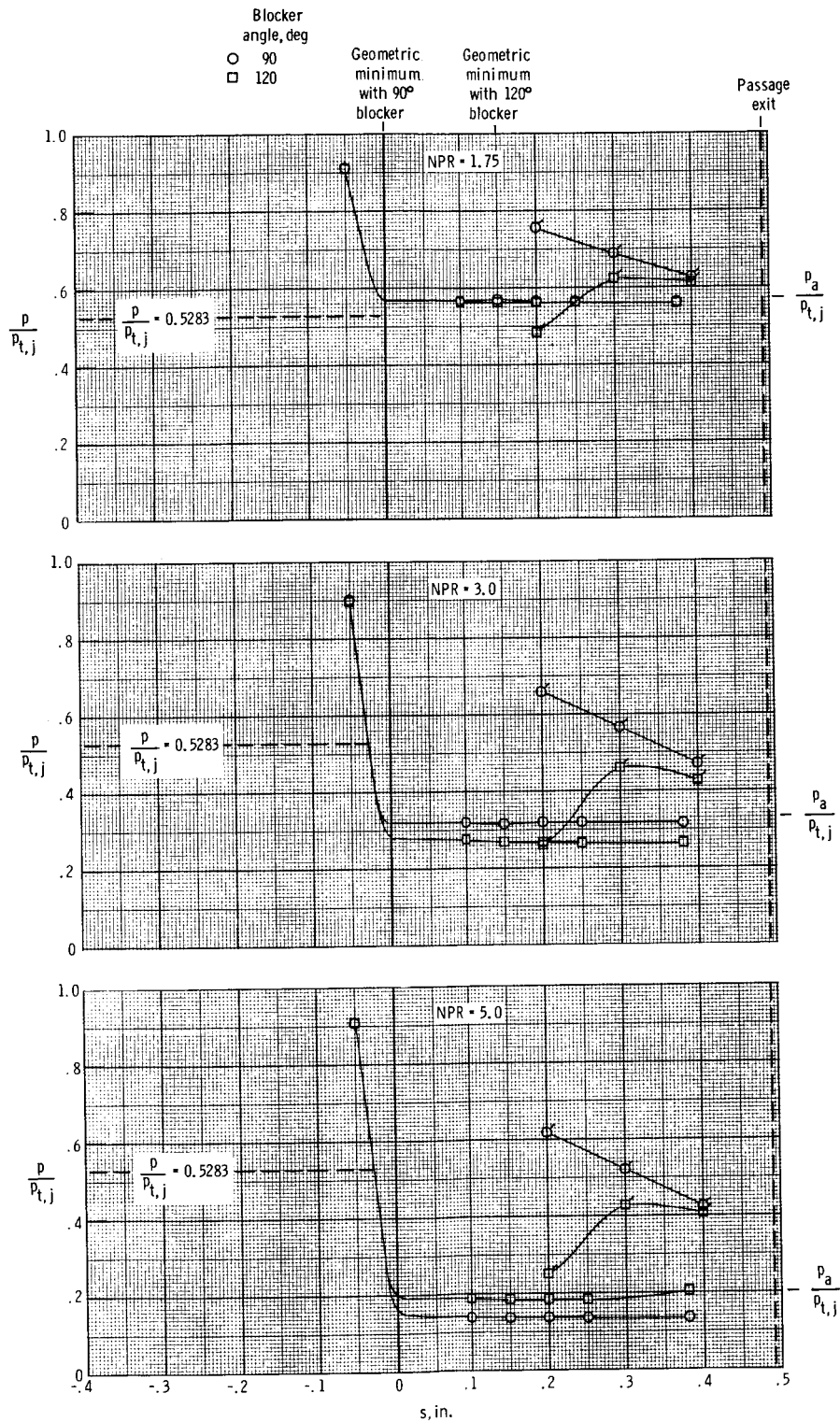
Figure 40. Pressure distributions (at three nozzle pressure ratios) on forward and aft flow surfaces for 90° port (corner radius of 0 in.) in convergent section of nozzle for two blocker angles. Flagged symbols indicate aft surface pressures.
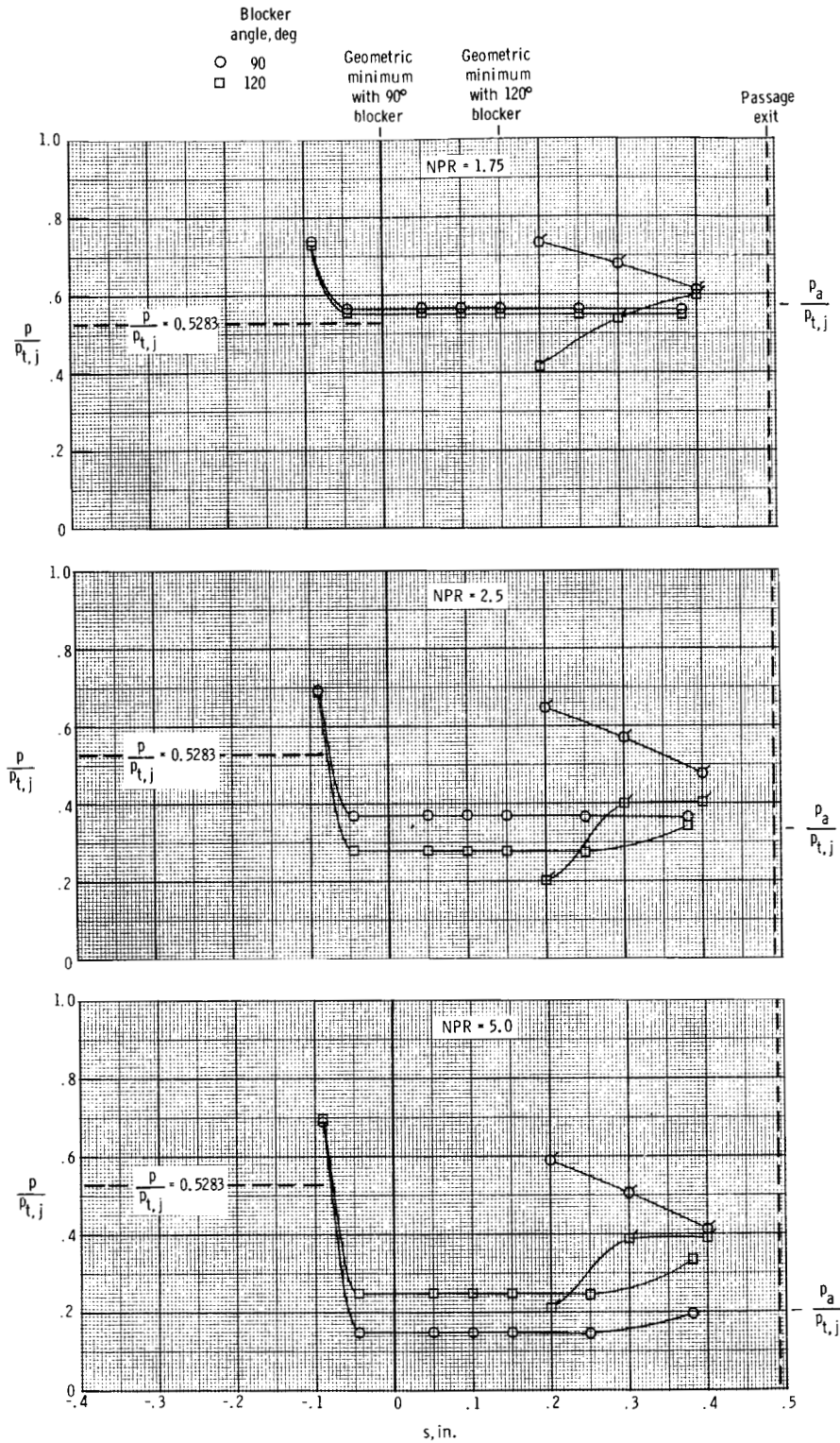
Figure 41. Pressure distributions (at three nozzle pressure ratios) on forward and aft flow surfaces for 90° port (corner radius of 0.047 in.) in convergent section of nozzle for two blocker angles. Flagged symbols indicate aft surface pressures.
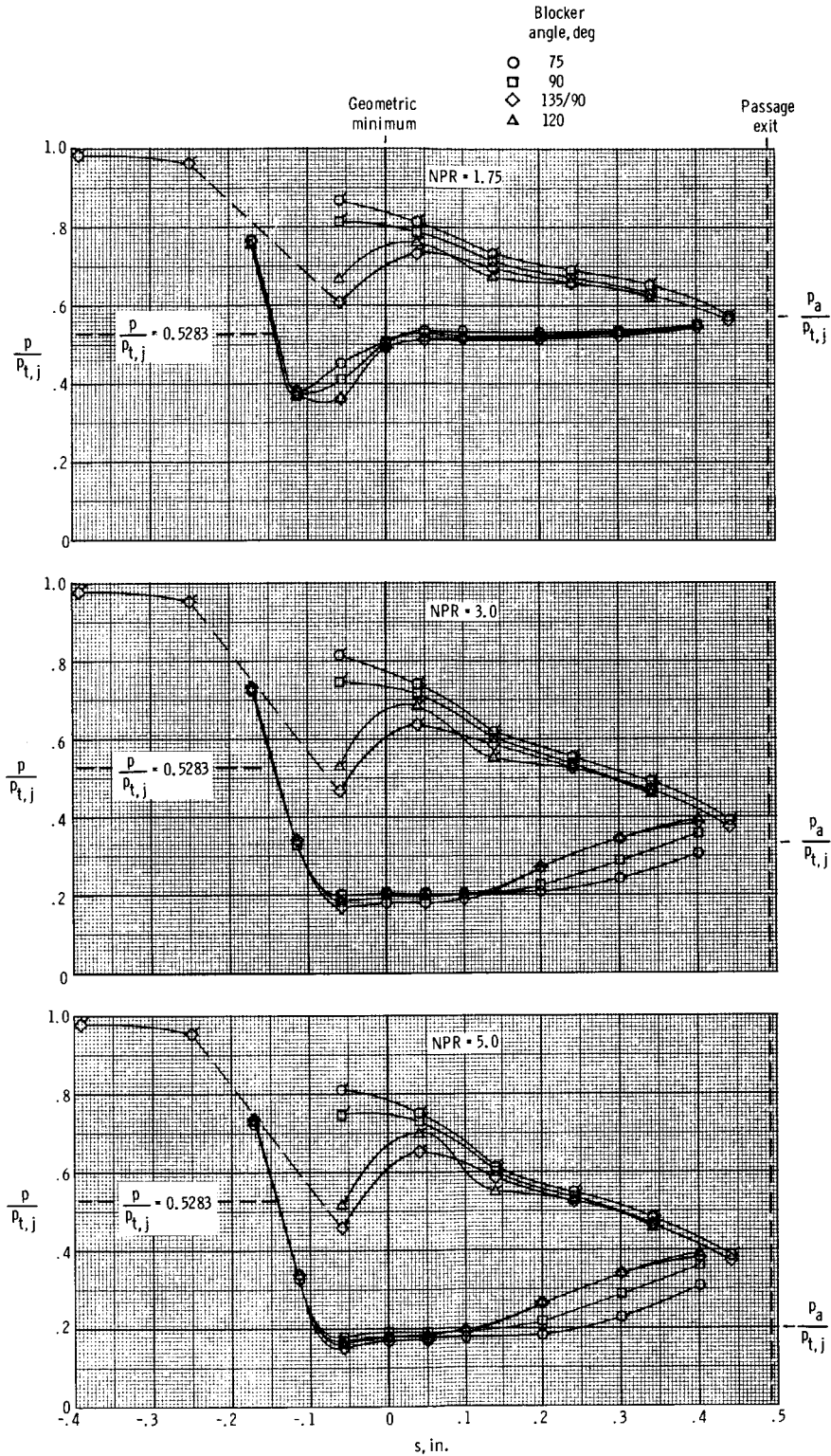
Figure 42. Pressure distributions (at three nozzle pressure ratios) on forward and aft flow surfaces for 90° port (corner radius of 0.109 in.) in constant-area duct for four blocker angles. Flagged symbols indicate aft surface pressures.

Figure 43. Pressure distributions (at three nozzle pressure ratios) on forward and aft flow surfaces for 120° port (corner radius of 0 in.) in constant-area duct for two blocker angles. Flagged symbols indicate aft surface pressures.
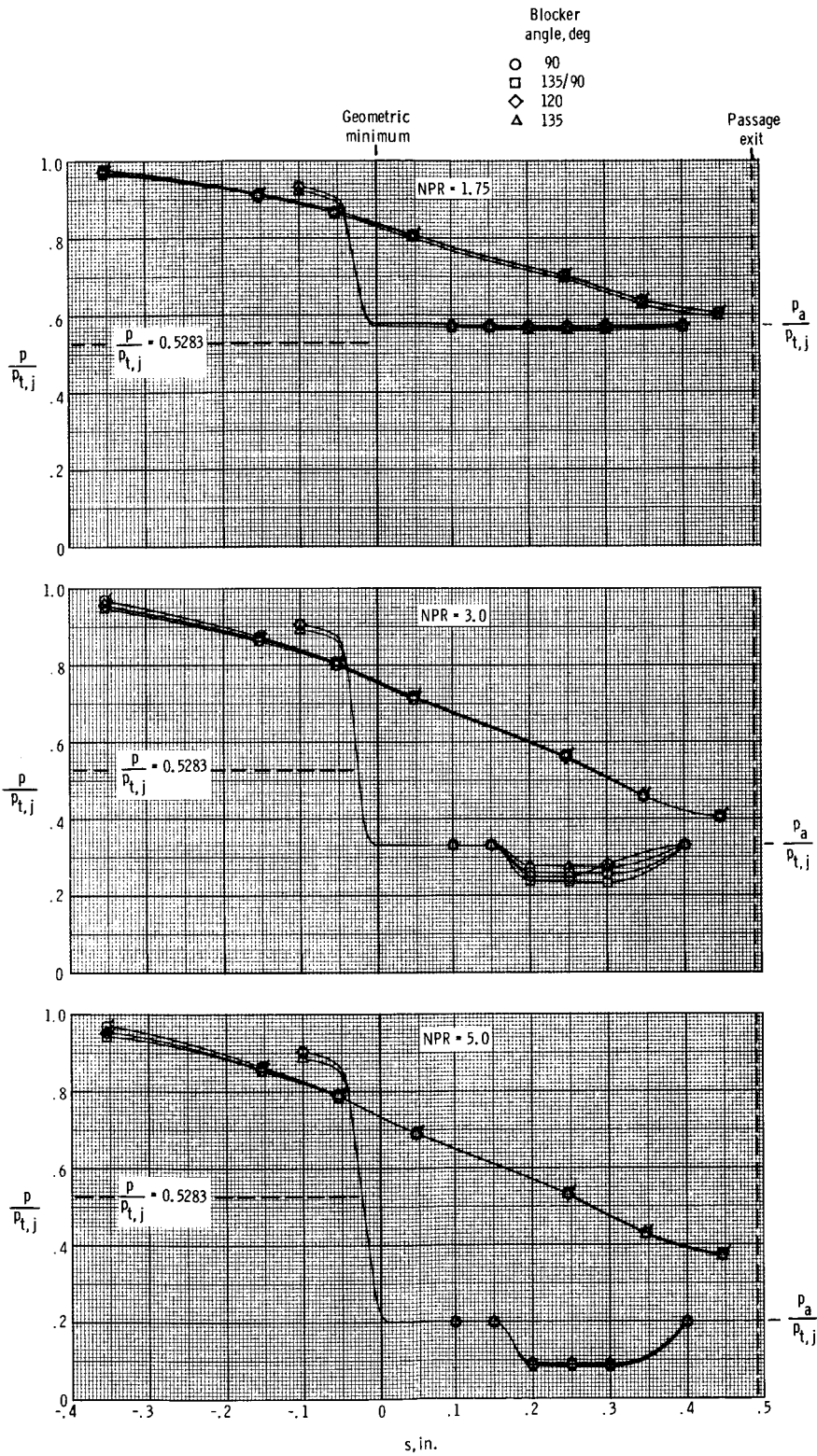
Figure 44. Pressure distributions (at three nozzle pressure ratios) on forward and aft flow surfaces for 135° port (corner radius of 0 in.) in convergent section of nozzle for four blocker angles. Flagged symbols indicate aft surface pressures.
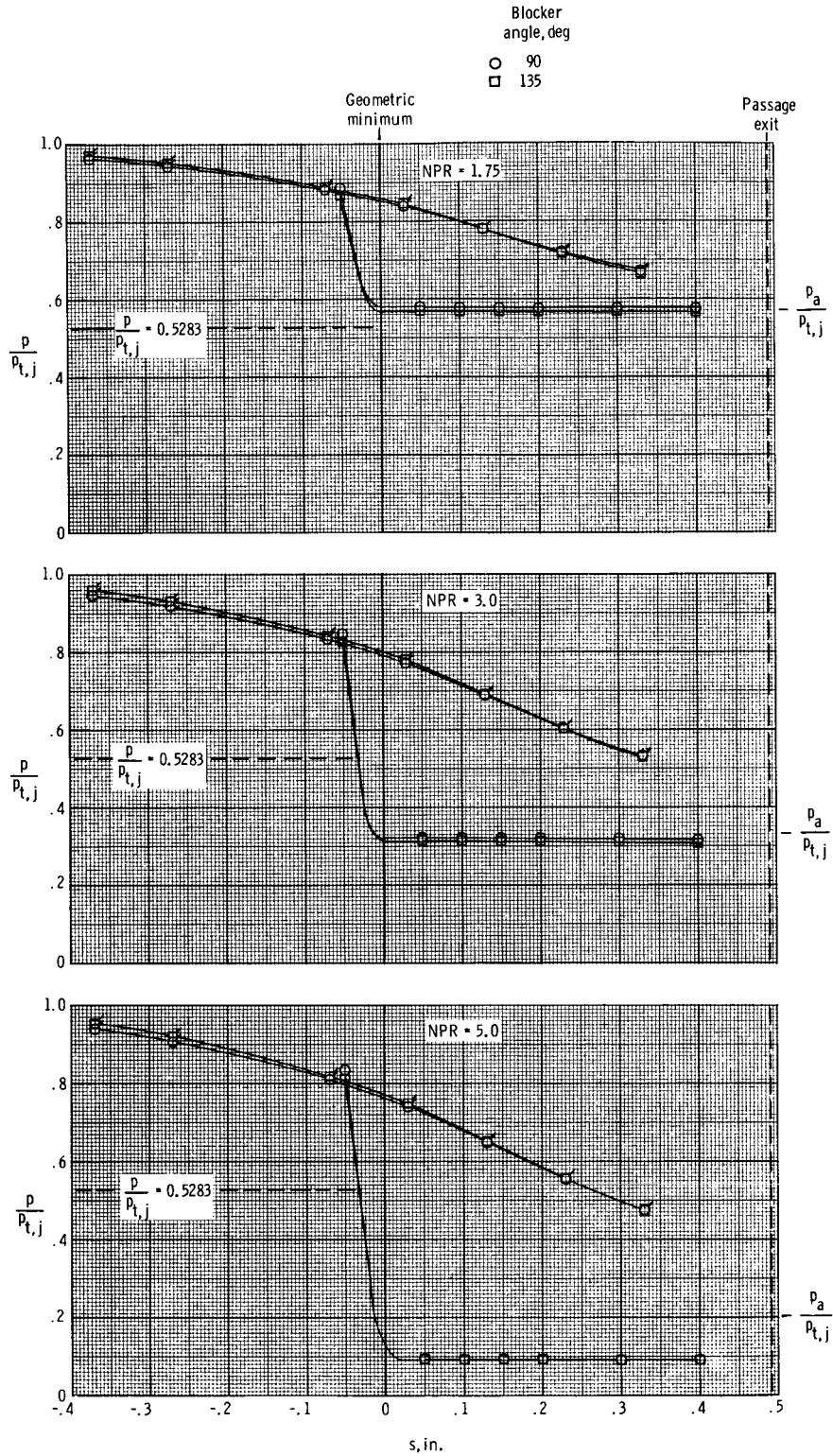
Figure 45. Pressure distributions (at three nozzle pressure ratios) on forward and aft flow surfaces for 135° port (corner radius of 0 in.) in constant-area duct for two blocker angles. Flagged symbols indicate aft surface pressures.

C-2
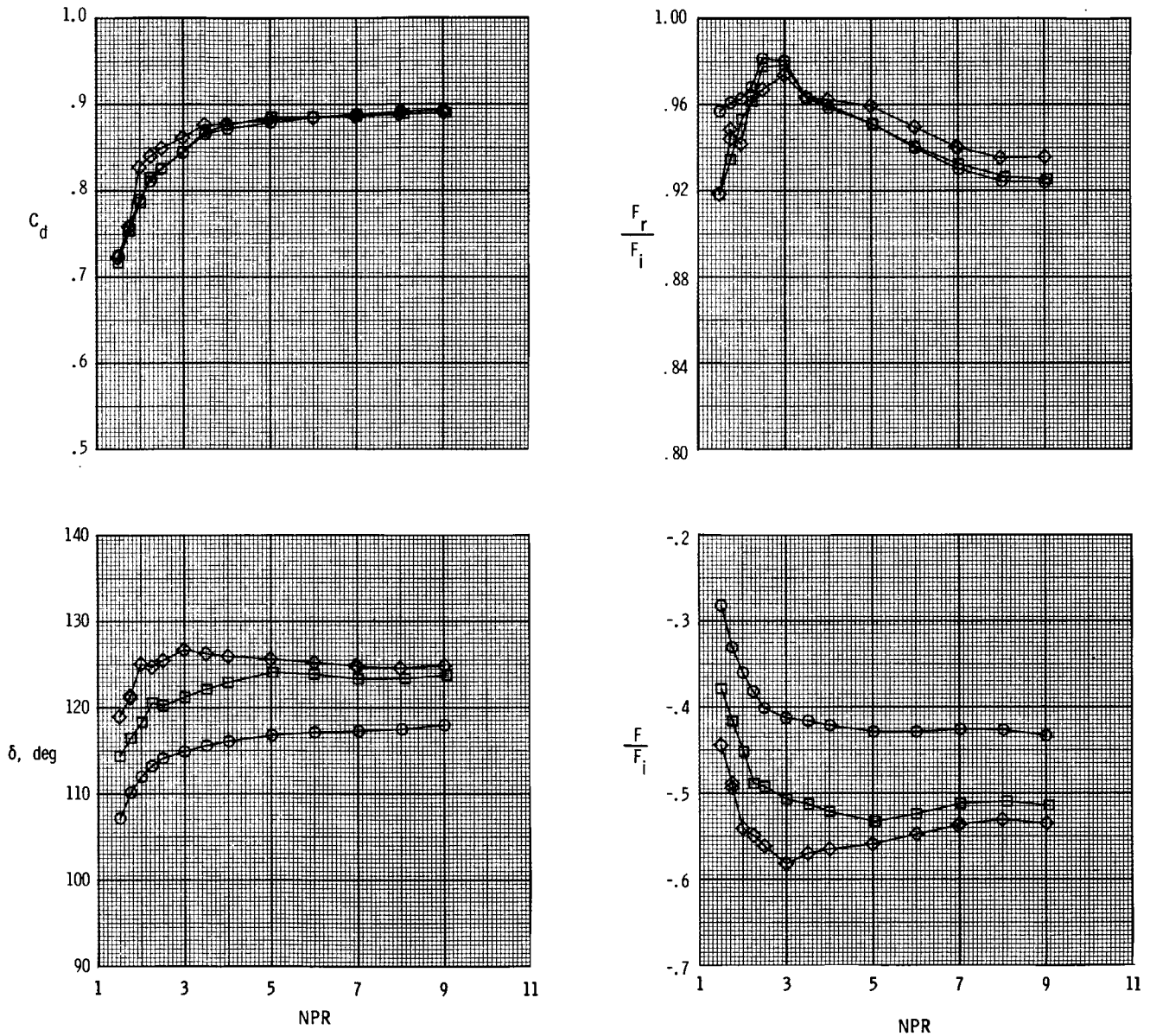
Figure 46. Effect of port-passage length on resultant thrust-vector angle, discharge coefficient, internal thrust ratio, and resultant thrust ratio for ports with geometric reverser angle of 120° with constant-area duct geometry and port corner radius of 0.109 in.
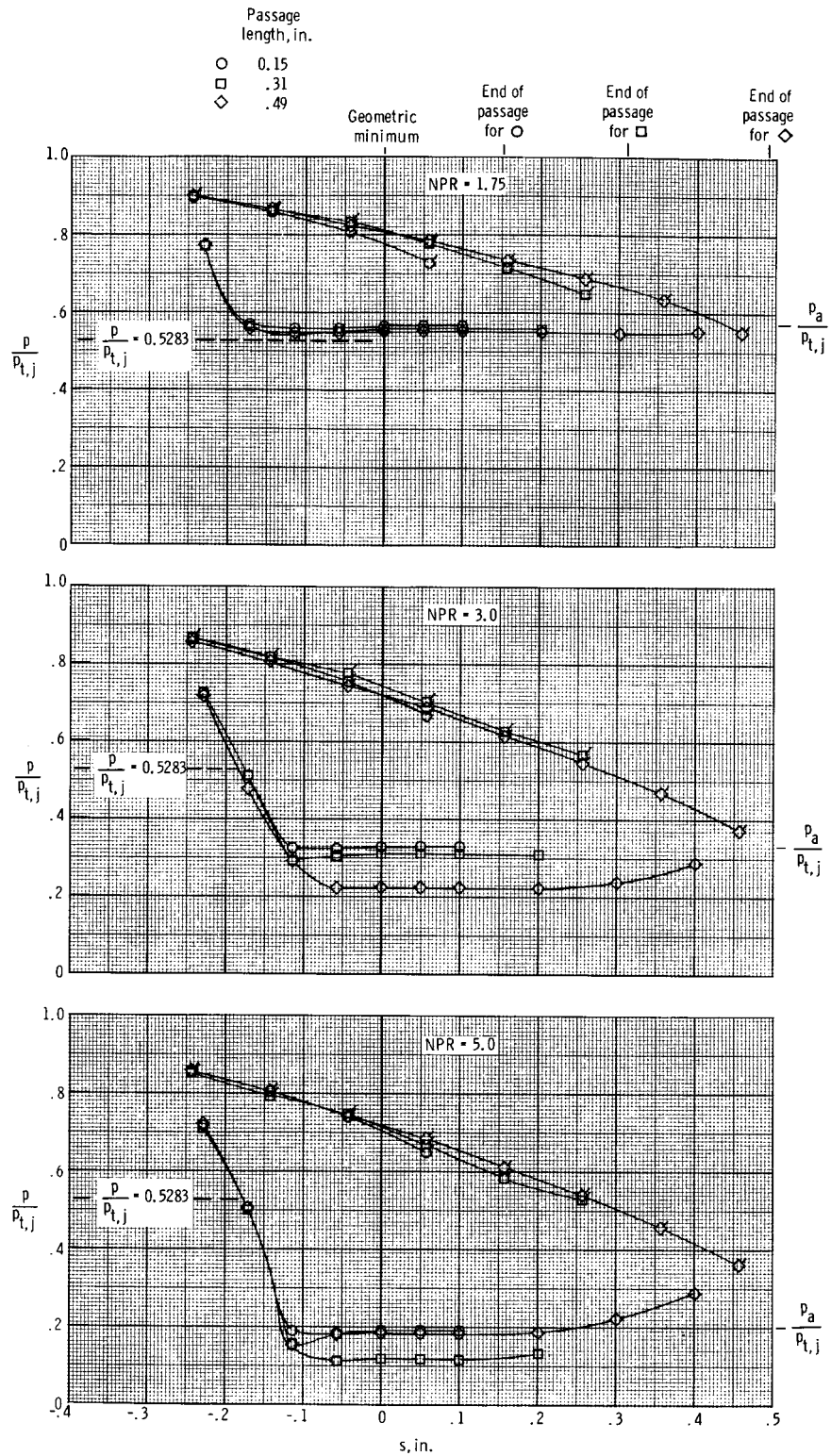
Figure 47. Pressure distributions (at three nozzle pressure ratios) on forward and aft flow surfaces for 120° port (corner radius of 0.109 in.) in constant-area duct for three port passage lengths. Flagged symbols indicate aft surface pressures.
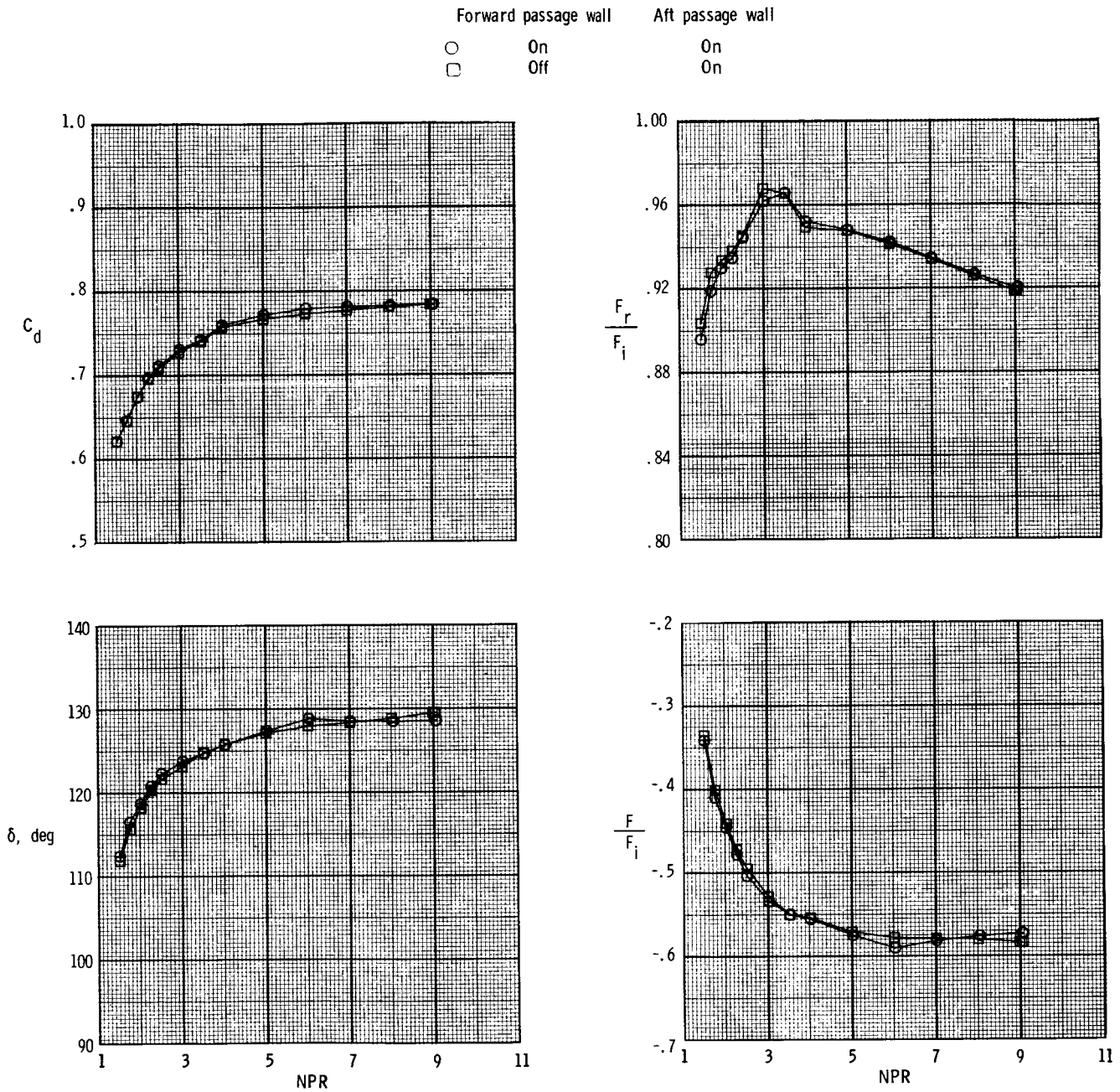
Figure 48. Effect of forward and aft passage walls on resultant thrust-vector angle, discharge coefficient, internal thrust ratio, and resultant thrust ratio for ports with geometric reverser angle of 120°, with constant-area duct geometry and port corner radius of 0 in.
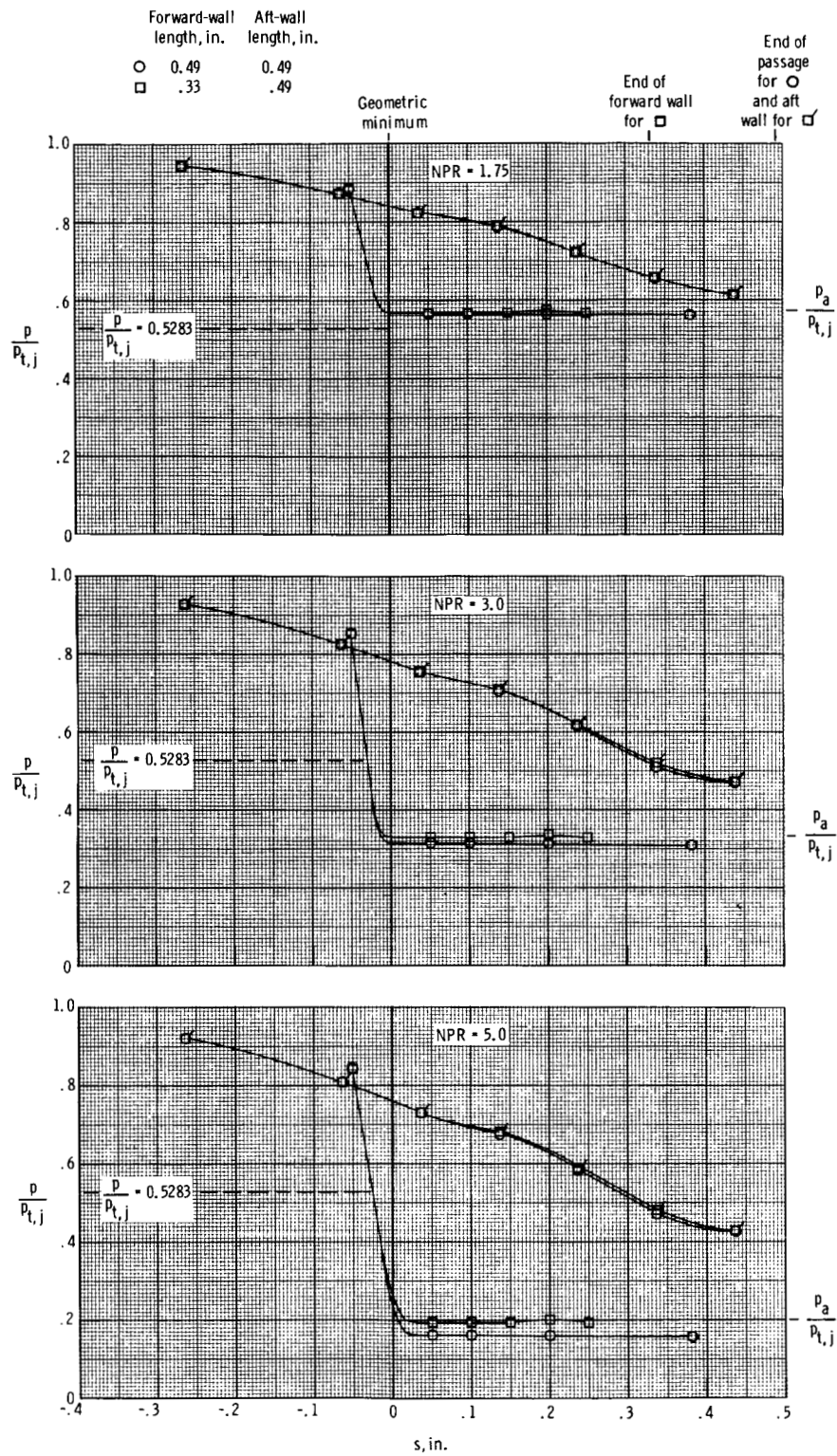
Figure 49. Pressure distributions (at three nozzle pressure ratios) on forward and aft flow surfaces for 120° port (corner radius of 0 in.) in constant-area duct for two forward passage wall lengths. Flagged symbols indicate aft surface pressures.

Report Documentation Page

1. Report No. NASA TM-89061	2. Government Accession No.	3. Recipient's Catalog No.
4. Title and Subtitle Effect of Varying Internal Geometry on the Static Performance of Rectangular Thrust-Reverser Ports		5. Report Date June 1987
		6. Performing Organization Code
7. Author(s) Richard J. Re and Mary L. Mason		8. Performing Organization Report No. L-16211
9. Performing Organization Name and Address NASA Langley Research Center Hampton, VA 23665-5225		10. Work Unit No. 505-62-91-01
		11. Contract or Grant No.
12. Sponsoring Agency Name and Address National Aeronautics and Space Administration Washington, DC 20546-0001		13. Type of Report and Period Covered Technical Memorandum
		14. Sponsoring Agency Code

15. Supplementary Notes

16. Abstract

An investigation has been conducted to evaluate the effects of several geometric parameters on the internal performance of rectangular thrust-reverser ports for nonaxisymmetric nozzles. Internal geometry was varied with a test apparatus which simulated a forward-flight nozzle with a single, fully deployed reverser port. The test apparatus was designed to simulate thrust reversal (conceptually) either in the convergent section of the nozzle or in the constant-area duct just upstream of the nozzle. The main geometric parameters investigated were port angle, port corner radius, port location, and internal-flow blocker angle. For all reverser-port geometries, the port opening had an aspect ratio (throat width to throat height) of 6.1 and had a constant passage area from the geometric port throat to the exit. Reverser-port internal performance and thrust-vector angles computed from force-balance measurements are presented.

17. Key Words (Suggested by Authors(s)) Thrust reversing Nonaxisymmetric nozzles Internal performance	18. Distribution Statement Unclassified—Unlimited Subject Category 02	
19. Security Classif.(of this report) Unclassified	20. Security Classif.(of this page) Unclassified	21. No. of Pages 101	22. Price A06